PhD Dissertation
Tesis Doctoral

Piezoelectric Energy Harvesting Devices (PEHDs) for the Development of Selfpowered Structural Health Monitoring Systems

Author / *Autor*:

María Infantes

Supervisor / *Director*:

Rafael Castro Triguero

Profesor Titular
Universidad de Córdoba

Tutor / *Tutor*:

Rafael Gallego Sevilla

Catedrático de Universidad
Universidad de Granada

Programa de doctorado en Ingeniería Civil
Escuela Internacional de Posgrado
Universidad de Granada

December, 2022

Editor: Universidad de Granada. Tesis Doctorales
Autor: María Macías Infantes
ISBN: 978-84-1117-689-7
URI: https://hdl.handle.net/10481/80007

A mi abuela Encarnación,
inspiración por su sabiduría.

Agradecimientos

Me gustaría aprovechar bien este espacio para agradecer sinceramente a todo aquel que me ha ayudado en el desarrollo de este trabajo de investigación. En primer lugar, a mi director de tesis, Rafael Castro, por todo su cariño, su enorme entusiasmo y su ayuda incondicional. Gracias por tus ideas y por ofrecerme todos los medios que han hecho posible la conclusión de este estudio. Gracias también a mi tutor Rafael Gallego por el apoyo y la guía durante toda esta etapa.

Mi más sincero agradecimiento al Prof. Michael Ian Friswell por su hospitalidad durante mi primera estancia de investigación en la *Swansea University* y por su inestimable ayuda durante el desarrollo de los trabajos de investigación y la elaboración de las publicaciones. Me siento muy afortunada por haber tenido la oportunidad de trabajar con un grupo tan reputado, también por haber encontrado allí la motivación en las primeras fases de mi doctorado. Me gustaría también agradecer a los miembros del *College of Engineering* por su acogida, especialmente a Rubén Sevilla por su guía inicial sobre la implementación de la metodología PGD. Muchas gracias a los estudiantes de doctorado, entre los que menciono con cariño a Germán Martínez, que sin duda hicieron que mi estancia fuera mucho más enriquecedora.

Un momento clave en mi formación fue la estancia de investigación en el *Laboratoire Energétique Mécanique Electromagnétisme (LEME)-Université Paris Nanterre*. Agradezco enormemente a Philippe Vidal, Olivier Polit y Laurent Gallimard todo el tiempo que me han dedicado. Su apoyo y predisposición para la colaboración fueron absolutos desde el principio, a pesar de que no existía ningún vínculo previo entre los grupos de investigación. Sin duda es gracias a las numerosas charlas, correcciones y herramientas que me han facilitado que esta tesis hoy ve la luz. No quiero olvidarme de mencionar aquí a Michele D'Ottavio, siempre dispuesto a ayudarme y hacerme sentir parte del grupo. *Merci à tous du fond du cœur*.

Quiero trasladar mi gratitud a todas las personas con las que he tenido el placer de colaborar en estos años. A los miembros del departamento de Mecánica de Estructuras e Ingeniería Hidráulica de la Universidad de Granada, en especial a Alejandro E. Martínez, Enrique García y Esther Puertas por toda la ayuda que me han brindado. Al personal de la Universidad de Córdoba, especialmente al PAS y al PDI del departamento de Mecánica y con cariño a María del Carmen Jurado, con los que he compartido tres años de trabajo. A

Francisco Javier Jiménez, del departamento de Ingeniería Eléctrica, por tantos buenos días de ensayos en el laboratorio. A Eduardo Hidalgo y Fernando Muñoz, de la Universidad de Sevilla, en particular por hacerme sentir parte responsable del proyecto *AIC3* para el que trabajamos juntos. Gracias a Pablo Pachón por su predisposición y buena actitud para la colaboración. A Javier F. Jiménez y Javier Naranjo, por tantas conversaciones inspiradoras y por estar conmigo desde el principio. A Iván Muñoz, Christian Gallegos, Carlos Martín de la Concha y todos los doctorandos del departamento de de la Universidad Politécnica de Madrid, por abrirme las puertas de su laboratorio y estar siempre dispuestos para la colaboración en nuevas líneas de trabajo que espero puedan seguir desarrollándose en el futuro. Gracias de corazón a Benedetta Orfeo y a Maleja Sánchez por la complicidad y por ampliar mis horizontes, los geográficos y los de mi interés investigador.
Estoy muy agradecida a las fuentes de financiación que han hecho posible esta tesis doctoral. Durante tres años he podido desarrollar mi investigación en la Universidad de Córdoba gracias al proyecto *AIC3* liderado por el Grupo Azvi y en colaboración con la Universidad de Sevilla, cofinanciado por el CDTI con una ayuda del programa I+D+i por y para el beneficio de las Empresas-Fondo Tecnológico (FEDER). Gracias también a la Universidad de Granada y al programa Erasmus+ por financiar mi estancia de investigación a través de la convocatoria de movilidad internacional 2020 para estudiantes de programas de doctorado. Muchas gracias a Ineco por acompañarme en esta última etapa de mi doctorado, especialmente a Alejandro Rodríguez y a Pablo Sánchez por su apoyo. Me llena de ilusión poder continuar este camino juntos con el desarrollo del proyecto *SMART BRIDGES*, seleccionado en la convocatoria de 2020 en líneas estratégicas de la Agencia Estatal de Investigación, en colaboración público-privada con las universidades de Córdoba y Granada.
Por último, agradecer a aquellas personas que no han colaborado directamente en la elaboración de esta tesis, pero que con su ilusión y sus ánimos han hecho de estos años una etapa mucho más agradable. A mi familia, también a la elegida, gracias.

María Macías Infantes
Madrid, 2022

Resumen

La idea fundamental que guía el trabajo presentado en esta tesis es la recolección de energía de las vibraciones estructurales para el desarrollo de sensores autónomos aplicados a la monitorización continua de estructuras civiles. La demanda energética de los sistema de monitorización se ha resuelto típicamente mediante la instalación de sensores conectados a la red eléctrica, lo cual supone un coste medioambiental y económico adicional difícil de mantener a largo plazo. Además, la ubicación remota de muchas estructuras hace inviable la conexión al suministro eléctrico. La novedad de esta propuesta es el autoabastecimiento de los sensores empleando un sistema de captación de energía totalmente limpio que utiliza las vibraciones de las estructuras para generarla. Esta generación de energía se lleva a cabo mediante el mecanimo de conversión de energía piezoeléctrica. A lo largo de los últimos años, se han presentado en la literatura diversos diseños para los dispositivos de recolección, siendo la viga *cantilever* con una/dos capas de material piezoeléctrico (configuraciones unimorfa/bimorfa) la más analizada. Opcionalmente, se coloca una masa en el extremo libre para modificar la frecuencia de resonancia hasta un valor deseado (habitualmente la propia frecuencia natural de la estructura huésped) y/o amplificar el efecto piezoeléctrico.

Esta tesis aborda el estudio de dispositivos piezoeléctricos de captación de energía con un doble enfoque. Por un lado, se plantea la modelización numérica de vigas compuestas como las que constituyen estos dispositivos. Para ello, se ha desarrollado y validado una nueva formulación basada en el método *Proper Generalized Decomposition* para resolver el problema de vibración forzada en vigas laminadas bidimensionales con capas piezoeléctricas. Se considera una descripción espacio-frecuencia del problema dinámico y la separación de variables del dominio espacial. El resultado es una solución 2D en el dominio de la frecuencia con una complejidad computacional 1D. Por otro lado, más orientado a la práctica, se analiza la viabilidad de un sistema piezoeléctrico de captación de energía basado en vibraciones aplicado en un puente de una autovía sito en Palma del Río, Córdoba (Spain). Para evaluar la potencia disponible a partir de vibraciones reales se plantea una nueva formulación semi-analítica basada en las vibraciones inducidas por el tráfico. Se han considerado dos situaciones diferentes de las que se extraen conclusiones sobre la evaluación de la potencia generada: i) registros de vibraciones con el puente abierto al tráfico regular, ii) vibraciones ambientales con el puente cerrado al tráfico.

Abstract

The underlying idea that guides the work presented in this dissertation is the vibration-based energy harvesting as an enabler for the successful development of self-powered sensors applied to long-term monitoring of civil structures. The energy requirement of the monitoring system has typically been solved by the installation of grid-connected sensors, which is a solution with a fixed additional economic and environmental cost difficult to maintain in the long term. In addition, the remote location of many structures makes mains power supply unfeasible. The novelty of this proposal is the self-supply of the sensors applying a totally clean energy collection system that uses the vibrations of the structures to generate energy. This vibration-based energy harvesting system makes use of devices in which the piezoelectric energy conversion mechanism takes place. The performance of piezoelectric energy harvesters is strongly dependent on the excitation source, represented by the vibration of the host structure. Numerous variants of these devices have been proposed in the literature but the most widely tested consists of a small cantilever beam with one/two layers of piezoelectric material (unimorph/bimorph configurations) and optionally a mass attached to the free end to move the resonance frequency towards some desired point (tuning) and/or amplify the conversion effect.

The study of piezoelectric energy harvesting devices has been approached in this thesis with a twofold focus. On the one hand, the numerical modelling of composite beams such as those that constitute piezoelectric energy harvesting devices is addressed. A new formulation based on the Proper Generalized Decomposition method to solve the forced vibration problem in bi-dimensional laminated beams with piezoelectric layers is developed and validated. A harmonic space-frequency description of the dynamic problem is considered and a variable separation in the spatial domain is introduced. The result is a 2D solution in frequency domain with 1D computational complexity. On the other hand, more geared to practice, the feasibility of a piezoelectric vibration-based energy harvesting system for a real highway bridge is studied. A new semi-analytic formulation based on the measured traffic-induced vibration has been used to evaluate the available power from real vibrations of a bowstring highway bridge located in Palma del Río, Córdoba (Spain). Two different situations have been considered from which conclusions on the assessment of harvested power are drawn: i) operational vibration records with the bridge open to regular traffic, ii) ambient vibrations with the bridge closed to traffic.

Contents

List of Figures

List of Tables

Notation

L	Length of the beam
h	Total hickness of the beam
h_f	Thickness of the face
h_c	Thickness of the core
S	Length to thickness ratio
NC	Number of layers
Ω_x	Problem domain in beam axis direction
Ω_z	Problem domain in thickness direction
ω	Load frequency
$\overline{\omega}$	Dimensionless load frequency
$C_{ij}^{(k)}$	Stiffness coefficients of layer k
$e_{ij}^{(k)}$	Piezoelectric constants of layer k
$\varepsilon_{ij}^{(k)}$	Permittivity coefficients of layer k
$u(x,z,\omega)$	Displacement field
$u_1(x,z,\omega)$	Displacement in beam axis direction
$u_3(x,z,\omega)$	Displacement in thickness direction
$v_1^i(x)$	Function of x at enrichment step i, for the approx. of u_1
$v_3^i(x)$	Function of x at enrichment step i, for the approx. of u_3
$f_1^i(z)$	Function of z at enrichment step i, for the approx. of u_1

$f_3^i(z)$	Function of z at enrichment step i, for the approx. of u_3
$g^i(\omega)$	Function of ω at enrichment step i, for the approx. of u_1,u_3
$\phi(x,z,\omega)$	Electric potential field
$v_\phi^i(x)$	Function of x at enrichment step i, for the approx. of ϕ
$f_\phi^i(z)$	Function of z at enrichment step i, for the approx. of ϕ
$g_\phi^i(\omega)$	Function of ω at enrichment step i, for the approx. of ϕ
$[q^v]$,$[q^{v_\phi}]$	Vector of DOFs associated with the mesh on Ω_x
$[q^f]$,$[q^{f_\phi}]$	Vector of DOFs associated with the mesh on Ω_z
$[q^g]$,$[q^{g_\phi}]$	Vector of DOFs associated with the mesh on ω
n_x	Number of elements in the mesh on Ω_x
n_z	Number of elements in the mesh on Ω_z
n_ω	Number of elements in the mesh on ω
$Ndof_x$	DOFs associated with the mesh on Ω_x
$Ndof_z$	DOFs associated with the mesh on Ω_z
N	Number of total enrichment steps

Glossary of Acronyms

ASD Acceleration Power Spectral Density. 73, 76

CLT Classical Laminate Theory. 13, 42
CRLT Coupled Refined Layerwise Theory. 56, 57
CUF Carrera's Unified Formulation. 16, 42

DOF Degree Of Freedom. 14, 15, 21, 24, 38, 42, 43, 51–53, 63

ESL Equivalent Single Layer. 13, 14, 36, 42

FE Finite Element. 3, 10, 11, 14, 15, 21, 24, 25, 33, 36–38, 43, 51–53, 56, 63, 82
FEA Finite Element Analysis. 15, 24, 28, 43, 53, 54, 60
FEM Finite Element Method. 14
FRF Frequency Response Function. 10, 11, 15, 24, 30–32, 34, 43, 53, 62
FSDT First-order Shear Deformation Theory. 13, 42

GAN Generative Adversarial Network. 3, 4

IoT Internet of Things. 2–4

LW Layerwise. 14, 15, 33, 36, 38, 42, 43, 63

MEMS Microelectromechanical Systems. 5

OMA Operational Modal Analysis. 3

PEHD Piezoelectric Energy Harvesting Device. 5, 7, 8, 11, 63, 67, 68, 81, 82, 84, 85

PGD Proper Generalized Decomposition. 3, 7, 8, 10, 11, 14, 15, 17, 23–26, 28, 29, 32–34, 36–38, 43, 52–54, 56, 58–60, 62, 63, 82–84

PSD Power Spectral Density. 76

PVD Principle of Virtual Displacements. 42

PZT lead zirconate titanate (Pb[Zr(x)Ti(1-x)]O3). 54, 56, 59, 76

RMS Root Mean Square. 73

RMVT Reissner Mixed Variational Theorem. 42

RUL Remaining Useful Life. 2

SDOF Single Degree Of Freedom. 67, 68, 75

SHM Structural Health Monitoring. 1–5, 7, 11, 41, 65, 66, 80, 81, 83, 85

WSN Wireless Sensor Network. 4, 5, 65, 80

1 Introduction

Para los proyectos a largo plazo, eso es lo más importante. Una vez que ajustas tu ritmo, lo demás viene por sí solo. Lo que sucede es que, hasta que el volante de inercia empieza a girar a una velocidad constante, todo el interés que se ponga en continuar nunca es suficiente.

HARUKI MURAKAMI, 2007

1.1 Scope of the thesis

The central idea around which the research plan of the present thesis focuses is the development of self-powered sensors for long-term Structural Health Monitoring (SHM). The energy requirement of the network has typically been solved by installing grid-connected systems, which are very expensive and difficult to maintain in the long term. The novelty of this approach is the self-supply of the sensors through a totally clean energy harvesting system based on the operational and ambient structural vibrations.

SHM is a reliable and effective maintenance technique. It can be applied to a wide variety of structural types, from bridges, footbridges, buildings, to dams, wind turbines or high voltage towers. Nowadays, this type of long-term monitoring is becoming increasingly necessary because structures such as ageing bridges, high-rise buildings or historic structures compromise the safety of many people. Thus, it is important to monitor their structural behaviour in order to be able to evaluate in-service performance, design control systems, detect possible failures early, detect damage caused by environmental agents, etc.

SHM technique involves the extensive use of devices and sensors deployed in the host structure. These sensors provide information on critical structural properties without damaging the structure or interrupting its normal use (non-destructive evaluation). This information is processed with different techniques (statistics, artificial intelligence) to determine the current state of the monitored structure and thus enabling data-driven maintenance decision-making. Advances in SHM can arise mainly in three interrelated

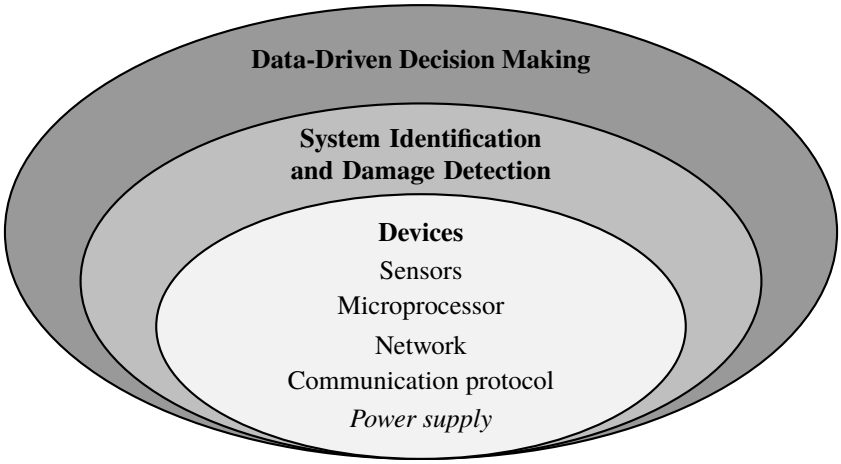

Figure 1.1 Circular stack diagram of a SHM system.

areas of research: data collection device technology, system identification and damage detection strategies and data-driven decision making techniques to support maintenance system (see Figure 1.1). In each of these areas, there are certain approaches that have been attracting much scientific interest in the last decade. The most relevant research topics are listed below.

1. *On the data-driven decision making techniques to support maintenance systems*

Data-driven techniques for infrastructure asset management have matured over the last decade aiming at optimising maintenance costs so that maintenance can be applied as needed as opposed to schedule or periodical strategies. Enabled by recent developments in the Internet of Things (IoT) and Industry 4.0, some researchers have proposed these models as digital twins of the entire infrastructure network, so that can be treated as expert-systems with learning capabilities.

a) **Digital twins**. Since its conceptual definition first published by Michael Grieves [1], digital twins have evolved in complexity. When applied to structural health management, digital twins need to incorporate anticipated predictability of damage and risk evaluation, self-adaptively to new environmental and operational conditions, and decision-making capabilities. By predictability, the digital twin of the infrastructure will be able to foresee the Remaining Useful Life (RUL) of its component structures.

b) **Expert systems for decision making**. Expert systems have the ability to emulate the human capacity to make decisions within a specific application domain based on execution rules and knowledge, which does not necessarily include self-adaptation. As for self-adaptively, the expert system will have the capacity to modify its behaviour in response to changing conditions with little or no human input, hence increasing efficiency, safety, and availability while minimizing the possibility of human errors [2].

2. *On the development of advanced SHM methodologies*

SHM is defined as the process of implementing a structural assessment strategy to perform a diagnosis of the integrity of structures. The field of SHM encompasses the use of a wide variety of monitoring technologies, although ambient/operational vibration-based SHM has received most attention owing to its minimal intrusiveness. These techniques exploit ambient/operational acceleration records to extract the modal features of a system through output-only Operational Modal Analysis (OMA) [3]. Several areas of research are trending these days:

a) **Environmental effects and damage detection.** The implementation of long-term automated SHM enables the early detection of damage by tracking anomalies in time series of identified modal features. Nonetheless, numerous papers have reported about the striking dependence of modal features on environmental (e.g. temperature, humidity, wind) and operational conditions (e.g. traffic level). It follows that environmental effects must be filtered out through statistical pattern recognition and machine learning techniques [4].

b) **Data-driven and reduced order modelling**. The increasing reduction in the costs related to monitoring equipment has promoted the development of SHM systems acquiring large amounts of monitoring data. This information can be used to feed a digital twin of the structure, and so relate the appearance of anomalies in the experimental data to damage in the structure. Nevertheless, such a process usually requires an elevated number of model evaluations, which results in a huge computational burden when the numerical model is computationally intensive. In this regard, the use of inexpensive reduced-order models bypassing the original offers an efficient solution. Manifold reduced-order models can be found in the literature such as Deep Neural Networks, Kriging metamodelling [5] or Proper Generalized Decomposition (PGD) [6].

c) **Automated unsupervised classification based on deep learning**. Damage identification is a key factor in the SHM process. The information is contained in temporal series, for which specific techniques are required to extract damage information according to pre-defined features. In the last years, there is a great effort in the scientific community in the development of unsupervised classifiers based on Deep Learning for continuous SHM [7, 8]. The main drawback of these classifiers is the dependence on large datasets associated with real damaged structures; typically, it is required 10 data sets (time-series) per trainable parameter. The amount of data for real damaged structures with different scenarios is limited. To circumvent this issue, it is required the generation of artificial data, compatible with the real structure. In this sense, the use of Generative Adversarial Networks (GANs) and the OMA-updated optimal Finite Element (FE) models provides optimal frameworks for Data Augmentation [9, 10]. GAN models are a type of deep neural networks focused on the generation of realistic data coming from specific featured class. The application of Transfer Learning techniques, common in Deep Learning models, to transfer the knowledge of classifiers from one domain to another domain (from one bridge to other similar bridge) could also be relevant.

3. *On the evolution of monitoring technologies to Smart Sensing based on IoT*

The traditional SHM sensing system is wire-based. The deployment of cables in the structure is very time-consuming and expensive, either for installation and maintenance. Continuous advances in the communication and sensing device technologies have made the use of Wireless Sensor Networks (WSNs) increasingly important. Additionally, the irruption of the IoT paradigm has burst the capabilities of this approach in SHM. However, several challenges must be faced to make these systems work highly capable and properly. These are the most relevant challenges:

a) **Node lifetime**. Wireless SHM nodes are designed to be powered by batteries whose lifetime depends largely on many factors. One of them is the battery capacity: the larger the battery, the longer the lifetime, which is in contrast to the current trend of reducing the size of the nodes. The sensors used to collect data consume the battery power load. Thus, a proper use of the sampling is required to optimize the use of the current. Another element which causes a fall in the battery capacity is the computing time taken by processing elements. This is a complex issue as many facts get involved in the amount of consumed current. A strategy which includes both two factors is to include a low-power sensor which triggers the execution of highly efficient mesh of sensing when a certain event is detected [11]. However, the most significant power consuming element is the communication component. Fog computing techniques and the communication protocols used play a crucial role.

b) **Edge & Fog computing**. The proliferation of IoT devices has led to the deployment of large networks of sensors. However, in order to maximize efficiency, these devices should be designed with minimum power, processing and memory resources. In order to achieve this goal, IoT sensors usually communicate with low-power protocols to a gateway (a device with greater resources, usually without energy restrictions), which then send data to cloud servers. Thus, a multi-layered architecture emerges in which information processing is not centralized in the cloud but undertaken, as far as possible, close to the information generators. This modern paradigm of distributed computing is called fog computing (edge computing when the end nodes themselves also participate in the processing). In data collection applications, giving the infrastructure an active role in information processing opens the door to adaptive models that significantly improve system efficiency. For example, adapting the intensity and frequency of the sampling process according to the relevance of the information itself [12]. The local Edge-Computing approach is particularly suitable for the SHM automated unsupervised classifiers based on GANs. Only valuable data, required for SHM diagnosis, is transferred to the cloud, which activates other prognosis health management stages.

c) **Power supply**. As mentioned above, for a WSN to be autonomous it needs a battery to provide power to record, process and transmit the data. Long-term SHM systems require considerable power for their operation, so this leads to continuous maintenance, consisting of replacing or recharging the batteries. To overcome this limitation and reduce maintenance costs, a significant research effort has being carried out to develop a variety of energy harvesting techniques [13, 14].

The energy harvesting technique and its application to powering WSNs of SHM systems represents the research topic of this thesis. It involves collecting and storing energy from non-exploited sources such as solar, wind and kinetic energy. In civil engineering applications, the latter is one of the most relevant sources, since structures are exposed to continuous vibrations due to operational (vehicle traffic, pedestrian streams, etc.) and ambient (mainly wind) conditions. The structural vibration can be used directly to generate energy by means of three physical conversion mechanisms: piezoelectric, electromagnetic and electrostatic [15, 16]. Other less used mechanisms are magnetostriction and flexoelectricity [17]. Piezoelectric is generally considered the most suitable of the conversion mechanisms, since it is compatible with Microelectromechanical Systems (MEMS), which represent the current trend for SHM sensor networks.

The piezoelectric effect is a reversible process by which some materials are able to generate electric charge when subjected to strain and vice versa (direct and inverse piezoelectric effect). This electromechanical behaviour can be expressed by the following two coupled constitutive equations:

$$T_{ij} = c^{E}_{ijkl} S_{kl} - e_{kij} E_k \tag{1.1a}$$

$$D_i = e_{ikl} S_{kl} + \varepsilon^{S}_{ik} E_k \tag{1.1b}$$

where T_{ij} is the stress tensor, S_{kl} is the strain tensor, E_k is the electric field tensor and D_i is the electric displacement tensor. The matrices c_{ijkl}, e_{kij} and ε_{ik} contain the elastic, piezoelectric, and permittivity constants, respectively, while the superscripts E and S denote that the constants are evaluated at constant electric field and constant strain, respectively. Alternative forms of piezoelectric constitutive equations can be also derived [18].

The performance of Piezoelectric Energy Harvesting Devices (PEHDs) is highly dependent on the excitation source represented by the vibration of the host structure. Different designs of these devices have been proposed and studied in the literature with the aim of taking advantage of this input signal and converting it into exploitable energy. Among all of them, the most widely analysed and tested PEHD consists of small cantilever beams, since, compared to other designs, they have lower resonance frequencies and a relatively larger strain for a given input excitation [19]. They typically comprise one or two layers of piezoelectric material (unimorph and bimorph configurations) and may optionally have a mass attached to the free end to move the resonant frequency towards a desired point (tuning) and/or amplify the conversion effect [20, 21]. These devices would be embedded in the host structure which, when vibrating, would induce a dynamic voltage in the layers of piezoelectric material, resulting in an alternating voltage output through electrodes placed on these layers. To use this energy to charge a battery, it would be necessary to have an electronic circuit to do the rectification and conversion to direct current. In the analysis of such devices, it is a common practice to consider a resistance or impedance to represent the electrical load.

A state-of-the-art review of the EH technique during the first stage of the research work led to the elaboration of the mind map shown in Figure 1.2. The diagram shows the main topics of current development, including: sources and conversion mechanisms, device architectures and their optimization to maximize the harvested power, equivalent circuit modelling, advanced electromechanical models and input/output analysis. The last two topics are the main focus of the three original research papers that make up this thesis.

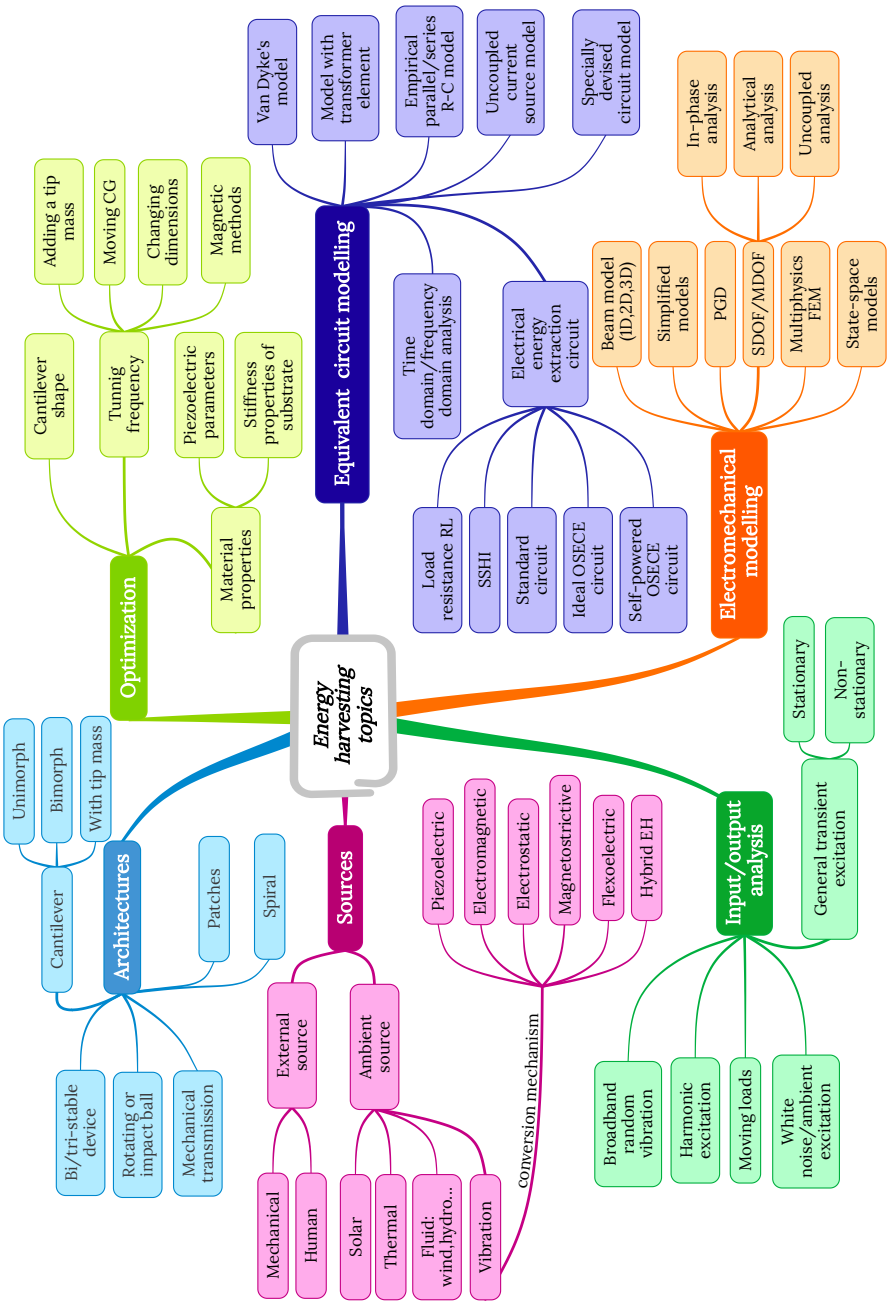

Figure 1.2 Mind map on the energy harvesting technique.

Regarding the numerical modelling, the main contribution of this research work is the application of PGD scheme to PEHDs modelling. PGD represents a new generation of numerical simulation strategies that has proven to be highly suitable in addressing problems that cannot be solved using direct and traditional numerical techniques. The PGD can be viewed as an *a priori* approach to reduced-order modelling. From its early development as a new family of solvers for some classes of multidimensional partial differential equations encountered in kinetic theory modelling of complex fluids [22], its applications have been very varied. It has been successfully applied to multidimensional models, separating physical space, parametric models defining virtual charts, real simulation, Dynamic Data Driven Applications Systems, etc [23]. In this case it is used as a strategy to separate the spatial domain of the problem.

1.2 Motivation

Energy harvesting from ambient vibration sources for use in powering low energy electronic devices has become the focus of numerous scientific studies over recent decades. The energy harvesting technique basically consists of capturing and storing energy from non-exploited external sources. These include environmental sources such as solar, wind and kinetic energy. This last source is very appealing in civil engineering as structures are subject to continuous ambient and operational vibration due to the action of traffic, wind, etc. This vibration can then be used directly to harvest energy to power electronic devices in the structure's support systems.

The use of energy harvesting devices is increasingly required, especially in targets where the use of batteries is either indispensable or desirable. The limited lifetime, high maintenance costs and the environmentally harmful recycling process of batteries justify this new paradigm. WSNs used in SHM systems represent one of the promising applications for many reasons:

- System efficiency: energy that would otherwise be lost is harvested.
- Maintenance cost savings: there is no need to replace or recharge the batteries of the system nodes.
- Environmental friendliness and safety improvement: the reduction in the manufacturing of new batteries containing chemicals and metals that are harmful to the environment and human health is encouraged.
- Accessibility to remote locations: possibility to monitor underwater, high altitude or remote structures by enabling real autonomy of the monitoring nodes.

In this field, energy harvesting from a vibrating piezoelectric device was established as a leading methodology. The piezoelectric energy conversion mechanism is selected because it offers several advantages, such as:

- High power density for a given input (power output/device volume).
- Output voltage high enough to charge a storage component without the need for multi-stage post-processing.

- No external load or input voltage is required, as the generation is produced by the material constitutive behaviour.
- Piezoelectric devices can be manufactured at the micro-scale.

Since vibration-based energy harvesting represents a clean power technology that can be of interest for application in civil engineering structures, the motivation of the present research work is thus justified.

1.3 Objectives

The scope of the present thesis is the vibration-based energy harvesting as an enabler for the successful development of self-powered sensors applied to long-term monitoring of civil structures. Since this is a very ambitious concern, the main objective of this research is to progress on the numerical modelling of PEHDs, as well as in the actual assessment of the the available power from operational structural vibration. Particularly, the study will seek to advance the following specific objectives:

- Application of the model reduction technique called PGD to the numerical analysis of composite beams with piezoelectric layers such as those that constitute the a PEHD. Indeed, applying the spatial decomposition of the problem allows obtaining a 2D solution in frequency domain with 1D computational complexity.
- In-depth analysis of the input and output signals of the PEHD. The input signal is represented by the host structure vibration from which the PEHD generates an output voltage. The input excitation can be different in nature: a harmonic excitation due to the action of a repetitive force over time, a transient dynamic load due to a vehicle passage, a broadband stochastic signal due to an environmental excitation (wind, etc.). The input/output signal analysis requires the detailed study of two fundamental aspects: the frequency width of the input signal (broadband) and the natural vibration frequencies of the host structure. These two aspects limit the amount of harvested energy since ideally the frequency width of the input signal and the natural frequencies of the host structure should match those of the harvesting mechanism, thus providing the highest possible output voltage. The aim would be to adopt a novel holistic approach to the problem through the statistics of the voltage of piezoelectric energy harvesters under real measured bridge vibration base excitation.

1.4 Original contributions

This section lists the papers that constitute the core of this thesis as well as those articles that are partially related to it.

1.4.1 Refereed journal papers

(A) **Title:** Forced vibration analysis of composite beams based on the variable separation method

Authors: **M Infantes**, P Vidal, R Castro-Triguero, L Gallimard, E García-Macías, O Polit

Reference: *Mechanics of Advanced Materials and Structures*, 28(6):618-634, 2020

Date: First published on-line March 23, 2019

DOI: 10.1080/15376494.2019.1578015

(B) **Title:** Evaluation of optimal sensor placement algorithms for the Structural Health Monitoring of architectural heritage. Application to the Monastery of San Jerónimo de Buenavista (Seville, Spain)

Authors: P Pachón, **M Infantes**, M Cámara, V Compán, E García-Macías, M I Friswell, R Castro-Triguero

Reference: *Engineering Structures*, 202:109843, 2020

Date: First published on-line November 9, 2019

DOI: j.engstruct.2019.109843

(C) **Title:** A collaborative machine learning-optimization algorithm to improve the finite element model updating of civil engineering structures

Authors: J Naranjo-Pérez, **M Infantes**, J F Jiménez-Alonso, A Sáez

Reference: *Engineering Structures*, 225:111327, 2020

Date: First published on-line September 25, 2020

DOI: j.engstruct.2020.111327

(D) **Title:** Forced vibration analysis of composite beams with piezoelectric layers based on the variable separation method

Authors: **M Infantes**, P Vidal, R Castro-Triguero, L Gallimard, O Polit

Reference: *Composite Structures*, 273:114248, 2021

Date: First published on-line June 11, 2021

DOI: j.compstruct.2021.114248

(E) **Title:** A feasibility study on piezoelectric energy harvesting from the operational vibration of a highway bridge

Authors: **M Infantes**, R Castro-Triguero, R R Sola-Guirado, D Bullejos, M I Friswell

Reference: *Advances in Structural Engineering*, Article in Press

Date: First published on-line September 1, 2022

DOI: 10.1080/15376494.2019.1578015

1.4.2 International conference papers

(A) **Title:** Determining the best pareto-solution in a multi-objective approach for model updating

Authors: **M Infantes**, J Naranjo-Pérez, A Sáez, J F Jiménez-Alonso

Published in: *Towards a Resilient Built Environment Risk and Asset Management*, pp. 523-530

Conference IABSE Symposium: Towards a Resilient Built Environment Risk and Asset Management, Guimarães (Portugal) 27-29 March 2019

(B) **Title:** Modeling of smart vibration-based energy harvesters based on the PGD method

Authors: **M Infantes**, R Castro-Triguero, P Vidal

Published in: Proceedings of ECCOMAS SMART 2019, pp. 1468-1479

Conference 9th ECCOMAS Thematic Conference on Smart Structures and Materials, Paris (France) 8-11 July 2019

1.5 Methodology and document outline

This doctoral dissertation has been written as a collection of articles. Following this methodology, the results of this thesis are presented as a series of research papers that have been published in different scientific media after a peer-review process. The three articles that constitute the core of this thesis, previously named as (A), (D) and (E), have been reprinted in a unified format and represent chapters 2, 3 and 4. Each chapter is briefly summarised as follows.

Chapter 2 proposes a new strategy based on the PGD method to solve the forced vibration problem in bi-dimensional layered beams. The approach redefines the problem by approximating the displacement field as a sum of separated functions of x (beam axis coordinate), z (thickness coordinate), and ω (load frequency) and proposes an iterative algorithm that solves three 1D problems at each iteration. Several numerical tests with different slenderness ratios and boundary conditions are considered to validate the method. The results in terms of modal parameters and Frequency Response Functions (FRFs) are analysed and compared with exact elasticity solution and FE simulations with very good agreements.

Chapter 3 extends the previous formulation to bi-dimensional composite beams with piezoelectric layers. The approach considers a classical harmonic space-frequency description of the dynamic problem and redefines it by approximating the displacement and electric potential fields as a sum of separated functions of the spatial domain. The result is a 2D solution in frequency domain with 1D computational complexity. Several numerical tests with wide range of slenderness ratios are considered in order to assess the validity of the method. Moreover, a study of different combinations of boundary conditions is carried out. The results in terms of modal parameters and FRFs are analysed and compared with

exact elasticity solution and FE simulations. Successful results opens up the possibility of confidently introducing electrical loads into the formulation, to the extension of the PGD approach to the parametric modelling of bimorph PEHDs.

Chapter 4 moves from the numerical analysis used in the previous two chapters towards a more applied approach. The study focuses on energy harvesting using cantilever piezoelectric devices excited by operational and ambient bridge vibration. The optimal design and analysis of energy harvesters is usually performed using the mean and standard deviation of a response quantity of interest (i.e. voltage) under broadband Gaussian white noise excitation. In this chapter, a novel holistic approach to the problem is proposed through the statistics of the voltage of piezoelectric energy harvesters under real measured bridge vibration base excitation. A new semi-analytic expression of the expected power is developed. The solution is based on the closed-form of the FRF between the harvester output voltage and the base excitation, and the experimentally measured spectral density of the latter. A study on the influence of the electromechanical coupling of the problem governing equations is first conducted. Then, a sensitivity analysis of the piezoelectric energy harvester parameters is performed. The critical analysis is developed through a case study of the measured long-term vibrations of a bowstring-arch highway bridge. Both operational and ambient vibration records are considered in the feasibility study. The results show the potential of the semi-analytic expression to evaluate the harvested power of piezoelectric harvesters under operational structural vibrations. This is a promising approach to confidently develop future analyses on the power requirements of WSNs for SHM.

Finally, **Chapter 5** summarizes the main contributions and conclusions of this thesis, as well as ongoing research works and possible future developments.

2 Forced vibration analysis of composite beams based on the variable separation method

Title:	Forced vibration analysis of composite beams based on the variable separation method
Authors:	M Infantes, P Vidal, R Castro-Triguero, L Gallimard, E García-Macías, O Polit
Journal:	Mechanics of Advanced Materials and Structures
ISSN:	1537-6494
JCR:	Impact Factor = 3.517, Q1 (Mechanics 22 / 136)
Details:	Volume: 28 (6), pages 618-634. Published online Mach 23, 2019
DOI:	10.1080/15376494.2019.1578015

2.1 Introduction

Considering the increasing applications of composite and sandwich structures in the industrial field due to their high specific strength and stiffness, it is important to develop advanced models to design with a good compromise between accuracy and computational costs. In this regard, accurate knowledge of deflection and stresses is required to take into account effects of the transverse shear deformation due to the low ratio of transverse shear modulus to axial modulus. Moreover, the transverse normal effect has to be included into the formulation for thick structures. In fact, all these aspects can play an important role on the behaviour of structures in service, in particular on natural frequencies or on the harmonic behaviour.

According to published research, various theories in mechanics for composite or sandwich structures have been developed. They can be classified as: (i) the Equivalent Single Layer (ESL) approach where the number of unknowns is independent of the number of layers, but the transverse shear and normal stresses continuity at the interfaces between layers are often violated. The Classical Laminate Theory (CLT) [24], the First-order

Shear Deformation Theory (FSDT) [25–30], and higher order theories [31–34] can be distinguished. Some of these theories also include the transverse normal effect with non-constant polynomial expressions of the out-of-plane displacement [35]. While most of these approaches are based on a displacement formulation, mixed formulations are also carried out in [36, 37] with the Finite Element Method (FEM); (ii) the Layerwise (LW) approach where the number of Degrees Of Freedom (DOFs) depends on the number of layers. This theory aims at overcoming the restriction of the ESL concerning the discontinuity of out-of-plane stresses at the interface layers. In recent contributions, various orders of expansion for the in-plane displacement are chosen: trigonometric [38], linear [39], and so forth; (iii) Alternative zig-zag approach developed in order to improve the accuracy of ESL models avoiding the additional computational cost of LW approach. Based on physical considerations and after some algebraic transformations, the number of unknowns becomes independent of the number of layers. Global higher-order theories and the zig-zag theories are asses in [40] to predict the global response of soft-core sandwich beams. A family of models was employed in [41] and more recently improved in [42, 43] with different orders of kinematic assumptions, taking into account the transverse normal strain. Note also the refined approach based on the Sinus model [44–46]. An extended review work on these models can be found in reference [47].

It should be noted the systematic approach based on the Carrrera's Unified Formulation to provide a large amount of 2D models for composite structures based on ESL and/or LW descriptions of the unknowns [48–50]. The aforementioned works deal with only some aspects of the broad research activity about models for layered structures and corresponding FE formulations. An extensive assessment of different approaches has been made in [47, 51–55]. A survey of developments in the vibration analysis of laminated composite beams is compiled in [56].

Over the past years, the PGD has shown interesting features in the reduction model framework [22]. This type of method was introduced by Ladevèze [57] and called *radial approximation* in the framework of the LArge Time INcrement (LATIN) method. In this latter, space coordinates and time variables are separated. It allows to decrease drastically computational time such as in [58, 59]. It has been also used in the context of separation of coordinate variables in multi-dimensional partial differential equations [22]. In particular, it has been applied for composite beams and plates in [60–63] with an in-plane / out-of-plane coordinate separation. Separated representation can be also applied to deduce parametric solutions where parameters are considered as problem extra-coordinates, see e.g. [64]. For a review about the PGD and its fields of application, readers can refer to [65, 66].

In this work, a model based on the PGD method is built for the forced vibration problem of laminated and sandwich beams under harmonic excitation. For this purpose, the displacements are written under the form of separated variable representation, i.e. a sum of products of unidimensional functions of x and z coordinates, and also the pulsation of the harmonic load ω. Note that the space and load frequency variable separation has been already addressed in [67]. Nevertheless, herein also the in-plane / out-of-plane coordinate separation is included in the formulation as it is well-suited to perform efficient computations for composite structures in terms of model complexity and computational cost. Moreover, the deduced explicit solution with respect to the pulsation allows us to

avoid numerous classical computations for each considered value of the load frequency within the domain of interest. To achieve that, the approximation of the 2D beam is based on a quadratic FE approximation for the variation with respect to x and a quadratic LW description for the variation with respect to z. Using the PGD, each unknown function of x is classically approximated using one DOF at each node of the mesh while the LW unknown functions of z are global for the whole beam. Finally, the deduced non-linear problem implies the resolution of three linear problems alternatively. This process yields to few unknowns involved in each of these linear problems.

In this paper, the reference problem is firstly recalled in section 2.2. The application of the PGD is given in the framework of the forced vibration problems with a specific parametrization in section 3.3. This particular assumption on the displacements yields a non-linear problem, solved through a classical iterative process. In section 2.4, the FE discretization is also described. Finally, the algorithm derived in the paper is verified numerically in section 2.5. For this purpose, a preliminary convergence study is first carried out. Then, the method is illustrated by numerical tests which have been performed upon various laminated and sandwich beams. The influence of slenderness ratios and boundary conditions are addressed. The accuracy of computations is evaluated by comparisons with an exact 2D elasticity solution, two-dimensional computations using commercial Finite Element Analysis (FEA) software and also results available in the literature. It is shown that the method allows us to obtain both the FRF and the shape modes with the associated eigenfrequencies with very good agreement respect to the reference solutions by using a a dimensionally reduced model which supposes less computational cost.

2.2 Reference problem description

In the present study, a straight beam of length L with a rectangular uniform cross section of thickness h and depth b is considered. The beam consists of NC layers assumed to be orthotropic in the beam axes. The x axis is taken along the longitudinal beam axis whereas y and z are the two axes of symmetry of the rectangular cross section (see Figure 2.1). The principal notation used in the formulation of the problem is summarized in the chapter on Notation in the preamble of this book.

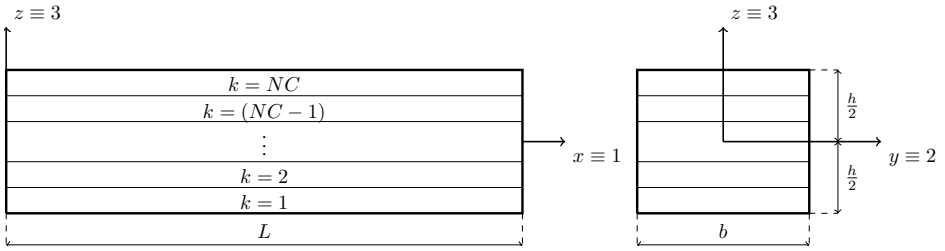

Figure 2.1 The laminated beam and coordinate system.

Hereafter, the y coordinate is neglected and the beam is considered in the (x,z) plane, i.e., in the domain $\Omega = \Omega_x \times \Omega_z = [0 \leq x \leq L] \times [-h/2 \leq z \leq h/2]$. In classical beam

theory, the displacement field is assumed to be expressed as

$$[u] = \begin{bmatrix} u_1(x,z) \\ u_3(x,z) \end{bmatrix} = \begin{bmatrix} \sum_{i=0}^{N_1} z^i v_1^i(x) \\ \sum_{i=0}^{N_3} z^i v_3^i(x) \end{bmatrix} \tag{2.1}$$

where $(v_1^i(x), v_3^i(x))$ are functions to be sought and N_1, N_3 are integers. For instance, by using this expression, models found in the literature can be described as follows

- The classical Timoshenko models with $N_1 = 1$ and $N_3 = 0$,
- ED2 model in Carrera's Unified Formulation (CUF) [53] with $N_1 = 2$ and $N_3 = 2$.

The problem of a composite beam subjected to an arbitrary dynamic excitation $[F_d(t)]$ is considered. Stresses can be conveniently written under the following form:

$$[\sigma]^\top = [\sigma_{11} \quad \sigma_{33} \quad \sigma_{13}] \qquad \text{or} \qquad [\tau] = \begin{bmatrix} \sigma_{11} & \sigma_{13} \\ \sigma_{13} & \sigma_{33} \end{bmatrix} \tag{2.2}$$

The boundary value problem to be solved consists of finding the displacement $[u(M,t)]$ and stress $[\sigma(M,t)], M \in \Omega$ such that

$$[\nabla_S]^\top [\sigma] + [b] = \rho \frac{\partial^2 [u]}{\partial t^2}, \quad \text{on } \Omega \tag{2.3}$$

$$[\tau(M,t)][n] = [F_d(t)], \quad \forall M \in \partial_F \Omega \tag{2.4}$$

$$[u(M,t)] = [u_d(t)], \quad \forall M \in \partial_u \Omega \tag{2.5}$$

where $[u_d]$ represents the displacement boundary condition, $[n]$ is the normal vector at the load application point, $[F_d(t)]$ is the prescribed surface load applied on $\partial_F \Omega = \partial_F \Omega_x \times \partial_F \Omega_z$, $[b]$ is the prescribed body load, ρ is the density of the material and $[\nabla_S]$ is the operator

$$[\nabla_S]^\top = \begin{bmatrix} \frac{\partial}{\partial x} & 0 & \frac{\partial}{\partial z} \\ 0 & \frac{\partial}{\partial z} & \frac{\partial}{\partial x} \end{bmatrix} \tag{2.6}$$

The problem can be expressed only in terms of the displacements using the constitutive relation $[\sigma] = [C][\varepsilon]$ and the kinematics equations $[\varepsilon] = [\nabla_S][u]$.

2.2.1 Constitutive relation

The stress-strain law of the k-th layer assumed to be orthotropic is

$$\begin{bmatrix} \sigma_{11}^{(k)} \\ \sigma_{33}^{(k)} \\ \sigma_{13}^{(k)} \end{bmatrix} = \begin{bmatrix} \bar{C}_{11}^{(k)} & \bar{C}_{13}^{(k)} & 0 \\ \bar{C}_{13}^{(k)} & \bar{C}_{33}^{(k)} & 0 \\ 0 & 0 & \bar{C}_{55}^{(k)} \end{bmatrix} \begin{bmatrix} \varepsilon_{11}^{(k)} \\ \varepsilon_{33}^{(k)} \\ \gamma_{13}^{(k)} \end{bmatrix} \tag{2.7}$$

where $\bar{C}_{ij}^{(k)}$ are the elastic moduli of the material taking into account the zero transverse normal stress hypothesis ($\sigma_{22} = 0$) expressed by

$$\bar{C}_{ij}^{(k)} = C_{ij}^{(k)} - C_{i2}^{(k)} C_{j2}^{(k)} / C_{22}^{(k)}, \qquad i,j = 1,3 \tag{2.8}$$

$$\bar{C}_{55}^{(k)} = C_{55}^{(k)} \tag{2.9}$$

where $C_{ij}^{(k)}$ are the 3D stiffness coefficients.

2.2.2 Variational formulation of the boundary value problem

Regarding the time dependent excitation, it can be expressed as $[F_d(t)] = [f_d] \cdot g(t)$, with $||f_d|| = 1$. The function $g(t)$ can be formulated as a superposition of weighted harmonic functions $e^{i\omega t}$, being i the imaginary unit and ω the load angular frequency

$$g(t) = \int_{-\infty}^{\infty} G(\omega)\, e^{i\omega t} \mathrm{d}\omega \tag{2.10}$$

where $G(\omega)$ is the Fourier transform of $g(t)$ and it represents the content of each harmonic in the excitation. In the following, a single harmonic excitation, $[F_d(t)] = [f_d]\, e^{i\omega t}$, is assumed as a basic problem. The response of a linear solid in absence of body loads and subjected to a harmonic excitation is presumed to have the same frequency as the applied load, $[u(M,t)] = [u(M)]e^{i\omega t}$, with $[u(M)]$ containing the displacements amplitude. Under these assumptions, the classical variational principle of a beam subjected to a harmonic load can be expressed as find $[u(M)] \in U$ (space of admissible displacement) such that

$$\int_\Omega [\varepsilon(\delta u)]^\top [\sigma(u)]\, \mathrm{d}V - \int_{\partial_F \Omega} [\delta u]^\top [f_d]\, \mathrm{d}S = \omega^2 \int_\Omega \rho [\delta u]^\top [u]\, \mathrm{d}V, \qquad \forall [\delta u] \in \delta U \tag{2.11}$$

where $[f_d]$ is the amplitude of the harmonic load. Note that in Eq. 2.11, damping is not considered.

2.3 Application of the PGD method to forced vibration beam

The PGD was introduced in [22]. This method is based on an *a priori* construction of the solution in separate variables. In the literature, the PGD has been used in order to separate spatial variables and also to consider problem parameters as extra-coordinates. In this approach, the PGD is first used to considering both the spatial variable separation and the introduction of the load frequency as an extra-coordinate in the solution. The following sections are dedicated to the application of PGD to the previous described problem.

2.3.1 Displacement field hypothesis

The displacement solution is built as

$$\begin{bmatrix} u_1(x,z,\omega) \\ u_3(x,z,\omega) \end{bmatrix} = \sum_{i=1}^{N} \left[u^i\right] = \sum_{i=1}^{N} g^i(\omega) \begin{bmatrix} f_1^i(z)\, v_1^i(x) \\ f_3^i(z)\, v_3^i(x) \end{bmatrix} \tag{2.12}$$

where $g^i(\omega), f_1^i(z), f_3^i(z), v_1^i(x), v_3^i(x)$ are functions which must be computed during the resolution process for each enrichment step $i = 1,2,...,n,...,N$. Considering this new

expression of the displacement (Eq. 2.12), Eq. 2.11 can be solved for a given value of the load frequency ω. Hence, the consideration of the load frequency within an interval $[\omega_{min},\omega_{max}]$ involves the resolution of multiple problems for many values of ω. To avoid these numerous resolutions, a new formulation is proposed as find $[u(M,\omega)] \in U$ such that $\forall\,[\delta u] \in \delta U$

$$\int_\omega \int_\Omega [\varepsilon(\delta u)]^\top [\sigma(u)]\,\mathrm{d}V\,\mathrm{d}\omega - \int_\omega \int_{\partial_F\Omega} [\delta u]^\top [f_d]\,\mathrm{d}S\,\mathrm{d}\omega \;=\; \int_\omega \int_\Omega \omega^2 \rho\,[\delta u]^\top [u]\,\mathrm{d}V\,\mathrm{d}\omega \quad (2.13)$$

2.3.2 The problem to be solved

The relation 2.12 can be written in a more compact form as

$$[u] = \sum_{i=1}^{N} g^i [F^i][v^i] = \sum_{i=1}^{N} g^i [V^i][f^i] \quad (2.14)$$

where

$$[v^i] = \begin{bmatrix} v_1^i(x) \\ v_3^i(x) \end{bmatrix}, \quad [V^i] = \begin{bmatrix} v_1^i(x) & 0 \\ 0 & v_3^i(x) \end{bmatrix}, \quad [f^i] = \begin{bmatrix} f_1^i(z) \\ f_3^i(z) \end{bmatrix}, \quad [F^i] = \begin{bmatrix} f_1^i(z) & 0 \\ 0 & f_3^i(z) \end{bmatrix} \quad (2.15)$$

In view of the above equations, an iterative procedure must be introduced. Assuming that the first $(n-1)$ functions have already been computed, the solution for iteration n is

$$[u] = [\bar{u}] + g[V][f] = [\bar{u}] + g[F][v] \quad (2.16)$$

where $[\bar{u}]$ is the displacement solution at iteration $(n-1)$ defined by

$$[\bar{u}] = \sum_{i=1}^{n-1} [u^i] = \sum_{i=1}^{n-1} g^i [F^i][v^i] = \sum_{i=1}^{n-1} g^i [V^i][f^i] \quad (2.17)$$

Note that for sake of clarity the superscript n is ignored for the current unknowns (g,f,v). These functions are computed such that Eq. 2.16 satisfies the weak form in Eq. 2.13. By ordering the terms and taking into account the constitutive law in the mentioned weak form

$$\int_\omega \int_\Omega [\varepsilon(\delta u)]^\top [C][\varepsilon(u)]\,\mathrm{d}V\,\mathrm{d}\omega - \int_\omega \int_\Omega \omega^2 [\delta u]^\top [u]\,\mathrm{d}V\,\mathrm{d}\omega = \int_\omega \int_{\partial_F\Omega} [\delta u]^\top [f_d]\,\mathrm{d}S\,\mathrm{d}\omega \quad (2.18)$$

where $[C]$ represents the plane stress-reduced stiffness tensor of each layer k as in Eq. 2.7 and δu is the virtual displacement

$$[\delta u] = \delta g[F][v] + g[V][\delta f] + g[F][\delta v] = \delta u_\omega + \delta u_f + \delta u_v \quad (2.19)$$

Introducing (2.19) into Eq. 2.18 the problem is decomposed into three equations, which are

$$\int_\omega \int_\Omega \left([\varepsilon(\delta u_\omega)]^\top [C][\varepsilon(\bar{u} + g\,F\,v)] - \omega^2 \rho\,[\delta u_\omega]^\top ([\bar{u}] + g[F][v]) \right) \mathrm{d}V\,\mathrm{d}\omega = \int_\omega \int_{\partial_F\Omega} [\delta u_\omega]^\top [f_d]\,\mathrm{d}S\,\mathrm{d}\omega \quad (2.20)$$

$$\int_\omega \int_\Omega \left([\varepsilon(\delta u_f)]^\top [C][\varepsilon(\bar{u} + g\,V\,f)] - \omega^2 \rho [\delta u_f]^\top ([\bar{u}] + g[V][f]) \right) \mathrm{d}V\,\mathrm{d}\omega = \int_\omega \int_{\partial_F \Omega} [\delta u_f]^\top [f_d]\,\mathrm{d}S\,\mathrm{d}\omega \quad (2.21)$$

$$\int_\omega \int_\Omega \left([\varepsilon(\delta u_v)]^\top [C][\varepsilon(\bar{u} + g\,F\,v)] - \omega^2 \rho [\delta u_v]^\top ([\bar{u}] + g[F][v]) \right) \mathrm{d}V\,\mathrm{d}\omega = \int_\omega \int_{\partial_F \Omega} [\delta u_v]^\top [f_d]\,\mathrm{d}S\,\mathrm{d}\omega \quad (2.22)$$

As these equations define a coupled non-linear problem, a non-linear resolution strategy must be used. The fixed point method is the simplest one. At the first step, initial functions $g^{(0)}$ and $f^{(0)}$ are set, and $v^{(0)}$ is computed from Eq. 2.22 with $g = g^{(0)}$ and $f = f^{(0)}$. Then, at each iteration, the algorithm computes a new solution $g^{(m+1)}$,$f^{(m+1)}$,$v^{(m+1)}$ such that

- Step 1: $g^{(m+1)}$ satisfies Eq. 2.20 for f,v set to $f^{(m)}$,$v^{(m)}$
- Step 2: $f^{(m+1)}$ satisfies Eq. 2.21 for g,v set to $g^{(m+1)}$,$v^{(m)}$
- Step 3: $v^{(m+1)}$ satisfies Eq. 2.22 for g,f set to $g^{(m+1)}$,$f^{(m+1)}$

The algorithm proceeds iteratively until reaching a fixed point.

2.3.2.1 Variational problem defined on load frequency domain ω

In order to simplify the notation, the functions $f^{(m)}$,$v^{(m)}$, which are assumed to be known, will be denoted as $\tilde{f}$,$\tilde{v}$ (and subsequently $\tilde{F}$,$\tilde{V}$ in matrix form) and the function $g^{(m+1)}$ to be computed will be denoted as g. The functions $\bar{g}^i$,$\bar{f}^i$,$\bar{v}^i$ are the solutions at the previous enrichment steps $i = 1,2,...,(n-1)$. The strain in Eq. 2.20 is defined in matrix notation as

$$[\varepsilon(g\tilde{F}\,\tilde{v})] = g\,[\Sigma_z(\tilde{f})]\,[\tilde{\mathscr{E}}_v] \quad (2.23)$$

with

$$[\Sigma_z(\tilde{f})] = \begin{bmatrix} 0 & \tilde{f}_1 & 0 & 0 \\ 0 & 0 & \tilde{f}_3' & 0 \\ \tilde{f}_1' & 0 & 0 & \tilde{f}_3 \end{bmatrix} \quad \text{and} \quad [\tilde{\mathscr{E}}_v]^\top = \begin{bmatrix} \tilde{v}_1 & \tilde{v}_1' & \tilde{v}_3 & \tilde{v}_3' \end{bmatrix} \quad (2.24)$$

where the prime ($'$) stands for the classical derivation. Thus, the variational problem defined on ω from Eq. 2.20 is then

$$g = \frac{f_\omega(\tilde{f},\tilde{v}) + \omega^2 \sum_{i=1}^{n-1} \bar{g}^i \mu^i_\omega(\tilde{f},\tilde{v},\bar{u}) - \sum_{i=1}^{n-1} \bar{g}^i \sigma^i_\omega(\tilde{f},\tilde{v},\bar{u})}{k_\omega(\tilde{f},\tilde{v}) - \omega^2 m_\omega(\tilde{f},\tilde{v})}, \quad \forall \quad \omega \in [\omega_{min},\omega_{max}] \quad (2.25)$$

with

$$\begin{aligned} k_\omega &= \int_\Omega [\tilde{\mathscr{E}}_v]^\top [\Sigma_z(\tilde{f})]^\top [C]\,[\Sigma_z(\tilde{f})]\,[\tilde{\mathscr{E}}_v]\,\mathrm{d}V, & \sigma^i_\omega &= \int_\Omega [\tilde{\mathscr{E}}_v]^\top [\Sigma_z(\tilde{f})]^\top [C]\,[\Sigma_z(\bar{f}^i)][\bar{\mathscr{E}}^i_v]\,\mathrm{d}V \\ m_\omega &= \int_\Omega [\tilde{v}]^\top [\tilde{F}]^\top \rho\,[\tilde{F}]\,[\tilde{v}]\,\mathrm{d}V, & \mu^i_\omega &= \int_\Omega [\tilde{v}]^\top [\tilde{F}]^\top \rho\,[\bar{F}^i]\,[\bar{v}^i]\,\mathrm{d}V \\ f_\omega &= \int_{\partial_F \Omega} [\tilde{v}]^\top [\tilde{F}]^\top [f_d]\,\mathrm{d}S \end{aligned} \quad (2.26)$$

By using the variational problem expression in Eq. 2.20, the value of $g(\omega)$ can be calculated explicitly for any ω considered in the range $[\omega_{min},\omega_{max}]$ through the Eq. 2.25.

Note that, as can be inferred from Eq. 2.25, there are values of ω for which resonance is detected. These values ω_n are calculated at convergence as

$$\omega_n^2 = \frac{k_\omega}{m_\omega} \tag{2.27}$$

This value will be used to estimate the natural frequencies of the beam as it will be shown in section 2.5 involving the numerical test cases.

2.3.2.2 Variational problem defined on Ω_z

The functions $g^{(m+1)}$,$v^{(m)}$, assumed to be known, will be denoted as $\tilde{g}$,$\tilde{v}$ and the function $f^{(m+1)}$ to be computed will be denoted as f. The strain in Eq. 2.21 is defined in matrix notation as

$$[\varepsilon(\tilde{g}\,\tilde{V}\,f)] = \tilde{g}\,[\Sigma_x(\tilde{v})]\,[\mathscr{E}_f] \tag{2.28}$$

with

$$[\Sigma_x(\tilde{v})] = \begin{bmatrix} \tilde{v}_1' & 0 & 0 & 0 \\ 0 & 0 & 0 & \tilde{v}_3' \\ 0 & \tilde{v}_1 & \tilde{v}_3' & 0 \end{bmatrix} \quad \text{and} \quad [\mathscr{E}_f]^\top = \begin{bmatrix} f_1 & f_1' & f_3 & f_3' \end{bmatrix} \tag{2.29}$$

Introducing the above expression into Eq. 2.21, the variational problem defined on Ω_z is

$$\begin{aligned} \gamma_\omega \int_{\Omega_z} [\delta\mathscr{E}_f]^\top [k_x(\tilde{v})]\,[\mathscr{E}_f]\,\mathrm{d}z - \alpha_\omega \int_{\Omega_z} [\delta f]^\top [m_x(\tilde{v})]\,[f]\,\mathrm{d}z = \beta_\omega \int_{\partial_F\Omega_z} [\delta f]^\top [f_x(\tilde{v})]\,\mathrm{d}z \\ + \sum_{i=1}^{n-1} \alpha_\omega^i \int_{\Omega_z} [\delta f]^\top [\mu_x^i(\tilde{v},\bar{u})]\,\mathrm{d}z - \sum_{i=1}^{n-1} \gamma_\omega^i \int_{\Omega_z} [\delta\mathscr{E}_f]^\top [\sigma_x^i(\tilde{v},\bar{u})]\,\mathrm{d}z \end{aligned} \tag{2.30}$$

where the coefficients integrated in the Ω_x domain are

$$\begin{aligned} [k_x] &= \int_{\Omega_x} [\Sigma_x(\tilde{v})]^\top [C]\,[\Sigma_x(\tilde{v})]\,\mathrm{d}x, & [\sigma_x^i] &= \int_{\Omega_x} [\Sigma_x(\tilde{v})]^\top [C]\,[\Sigma_x(\bar{v}^i)][\bar{\mathscr{E}}_f^i]\,\mathrm{d}x \\ [m_x] &= \int_{\Omega_x} [\tilde{V}]^\top \rho\,[\tilde{V}]\,\mathrm{d}x, & [\mu_x^i] &= \int_{\Omega_x} [\tilde{V}]^\top \rho\,[\bar{V}^i][\bar{f}^i]\,\mathrm{d}x \\ [f_x] &= \int_{\partial_F\Omega_x} [\tilde{V}]^\top [f_d]\,\mathrm{d}x \end{aligned} \tag{2.31}$$

and the coefficients that only depend on the load frequency are

$$\begin{aligned} \gamma_\omega &= \int_\omega \tilde{g}^2\,\mathrm{d}\omega, & \gamma_\omega^i &= \int_\omega \tilde{g}\,\bar{g}^i\,\mathrm{d}\omega, & \beta_\omega &= \int_\omega \tilde{g}\,\mathrm{d}\omega \\ \alpha_\omega &= \int_\omega \omega^2\tilde{g}^2\,\mathrm{d}\omega, & \alpha_\omega^i &= \int_\omega \omega^2\tilde{g}\,\bar{g}^i\,\mathrm{d}\omega, \end{aligned} \tag{2.32}$$

In this way, the variational problem defined by Eq. 2.21 is a linear expression that must be solved in the Ω_z domain through Eq. 2.30.

2.3.2.3 Variational problem defined on Ω_x

At this step, the functions $g^{(m+1)}$,$f^{(m+1)}$, which are assumed to be known, will be denoted as $\tilde{g}$,$\tilde{f}$ and the function $v^{(m+1)}$ to be computed will be denoted as v. The expression of the strain being $[\varepsilon(\tilde{g}\,\tilde{F}\,v)] = \tilde{g}\,[\Sigma_z(\tilde{f})]\,[\mathscr{E}_v]$, the variational problem defined on Ω_x becomes

$$\gamma_\omega \int_{\Omega_x} [\delta\mathscr{E}_v]^\top [k_z(\tilde{f})]\,[\mathscr{E}_v]\,\mathrm{d}x - \alpha_\omega \int_{\Omega_x} [\delta v]^\top [m_z(\tilde{f})]\,[v]\,\mathrm{d}x = \beta_\omega \int_{\partial_F\Omega_x} [\delta v]^\top [f_z(\tilde{f})]\,\mathrm{d}x + \sum_{i=1}^{n-1} \alpha_\omega^i \int_{\Omega_x} [\delta v]^\top [\mu_z^i(\tilde{f},\bar{u})]\,\mathrm{d}x - \sum_{i=1}^{n-1} \gamma_\omega^i \int_{\Omega_x} [\delta\mathscr{E}_v]^\top [\sigma_z^i(\tilde{f},\bar{u})]\,\mathrm{d}x \quad (2.33)$$

with

$$[k_z] = \int_{\Omega_z} [\Sigma_z(\tilde{f})]^\top [C]\,[\Sigma_z(\tilde{f})]\,\mathrm{d}z, \qquad [\sigma_z^i] = \int_{\Omega_z} [\Sigma_z(\tilde{f})]^\top [C]\,[\Sigma_z(\bar{f}^i)][\bar{\mathscr{E}}_v^i]\,\mathrm{d}z$$
$$[m_z] = \int_{\Omega_z} [\tilde{F}]^\top \rho\,[\tilde{F}]\,\mathrm{d}z, \qquad [\mu_z^i] = \int_{\Omega_z} [\tilde{F}]^\top \rho\,[\bar{F}^i][\bar{v}^i]\,\mathrm{d}z$$
$$[f_z] = \int_{\partial_F\Omega_z} [\tilde{F}]^\top [f_d]\,\mathrm{d}z \quad (2.34)$$

Analogously, the variational problem defined by Eq. 2.22 is a linear expression that must be solved in the Ω_x domain through Eq. 2.33.

2.4 Galerkin discretization

To build the displacement solution, a discrete representation of the functions g,f,v must be introduced. A classical FE approximation is used in Ω_x and Ω_z. The element vector of DOFs associated with the mesh in Ω_x and Ω_z are denoted as $[q_e^v]$ and $[q_k^f]$, respectively. The part of the displacement and strain fields that only depends on spatial variables are determined from the values of $[q_e^v]$ and $[q_k^f]$ by

$$[v_e] = [N_x][q_e^v], \quad [\mathscr{E}_v^e] = [B_x][q_e^v], \quad [f_k] = [N_z][q_k^f], \quad [\mathscr{E}_f^k] = [B_z][q_k^f] \quad (2.35)$$

where the matrices $[N_x]$, $[B_x]$, $[N_z]$ and $[B_z]$ contain the shape functions, their derivatives and the Jacobian components. The number of DOFs of the problems in Ω_x and Ω_z are

$$Ndof_x = 2\,n_x\,(N_n - 1) + 1 \quad (2.36)$$
$$Ndof_z = 2\,n_z\,(N_n - 1) + 1 \quad (2.37)$$

where n_x and n_z are the total number of elements in $\Omega_x = \bigcup_{e=1}^{n_x} \Omega_x^e$ and $\Omega_z = \bigcup_{k=1}^{n_z} \Omega_z^k$ domain, respectively, and N_n is the number of nodes per element (can be different for each domain). For the load frequency, a uniform discretization of the interval $[\omega_{min},\omega_{max}]$ is considered. The trapezoidal rule is used for the approximation of the integrals in α_ω, γ_ω and β_ω. The size of vector g is denoted as n_ω and it coincides with the DOFs of the problem in the load frequency domain.

2.4.1 Approximation on load frequency domain ω

Taking into account the discretization expressed by Eq. 2.35, for each value of $\omega_j = \omega_{min} + (j-1)\,\dfrac{\omega_{max}-\omega_{min}}{n_\omega - 1}$, $j = 1,\ldots,n_\omega$, the variational Eq. 2.25 can be rewritten as

$$g(\omega_j) = \frac{f_\omega + \omega_j^2 R_{\omega,M} - R_{\omega,K}}{k_\omega - \omega_j^2 m_\omega} \tag{2.38}$$

where

$$k_\omega = \sum_{e=1}^{nx} \int_{\Omega_x^e} [\tilde{\mathscr{E}}_v^e]^\top \left[\sum_{k=1}^{nz} \int_{\Omega_z^k} [\Sigma_z(\tilde{f}_k)]^\top [C_k] [\Sigma_z(\tilde{f}_k)] \,\mathrm{d}z \right] [\tilde{\mathscr{E}}_v^e] \,\mathrm{d}x \tag{2.39}$$

$$m_\omega = \sum_{e=1}^{nx} \int_{\Omega_x^e} [\tilde{v}_e]^\top \left[\sum_{k=1}^{nz} \int_{\Omega_z^k} [\tilde{F}_k]^\top \rho\, [\tilde{F}_k] \,\mathrm{d}z \right] [\tilde{v}_e] \,\mathrm{d}x \tag{2.40}$$

$$f_\omega = [\tilde{v}_{e_p}]^\top [\tilde{F}_{k_p}]^\top [f_d], \quad \text{for } e_p \text{ and } k_p \text{ the elements where the load is applied} \tag{2.41}$$

$$R_{\omega,M} = \sum_{i=1}^{n-1} \bar{g}^i(\omega_j)\, \mu_\omega^i(\tilde{f}_k, \tilde{v}_e, \bar{u}) \tag{2.42}$$

$$R_{\omega,K} = \sum_{i=1}^{n-1} \bar{g}^i(\omega_j)\, \sigma_\omega^i(\tilde{f}_k, \tilde{v}_e, \bar{u}) \tag{2.43}$$

2.4.2 Finite element approximation on Ω_z

The introduction of Eq. 2.35 into the variational Eq. 2.30 leads to the following linear system

$$\Big([K_f] - [M_f] \Big) [q^f] = [F_f] - [R_f] \tag{2.44}$$

where $[q^f]$ is the vector of the nodal displacements associated with the mesh in Ω_z, $[K_f]$ and $[M_f]$ are the stiffness and mass matrices obtained by assembling the element stiffness and mass matrices $[K_f^k]$ and $[M_f^k]$ respectively, $[F_f]$ is the load vector obtained by assembling the element load vectors $[F_f^k]$ and $[R_f]$ is the equilibrium residual obtained by assembling the element residual vectors $[R_f^k]$ whose expressions are

$$[K_f^k] = \gamma_\omega \int_{\Omega_z^k} [B_z]^\top \left[\sum_{e=1}^{n_x} [k_x(\tilde{v}_e)] \right] [B_z] \,\mathrm{d}z \tag{2.45}$$

$$[M_f^k] = \alpha_\omega \int_{\Omega_z^k} [N_z]^\top \left[\sum_{e=1}^{n_x} [m_x(\tilde{v}_e)] \right] [N_z] \,\mathrm{d}z \tag{2.46}$$

$$[F_f^k] = \beta_\omega \int_{\partial_F \Omega_z^k} [N_z]^\top \left[\sum_{e=1}^{n_x} [f_x(\tilde{v}_e)] \right] \mathrm{d}z \tag{2.47}$$

$$[R_f^k] = \sum_{i=1}^{n-1} \gamma_\omega^j \int_{\Omega_z^k} [B_z]^\top \left[\sum_{e=1}^{n_x} [\sigma_x^i(\tilde{v}_e, \bar{u})] \right] \mathrm{d}z - \sum_{i=1}^{n-1} \alpha_\omega^i \int_{\Omega_z^k} [N_z]^\top \left[\sum_{e=1}^{n_x} [\mu_x^i(\tilde{v}_e, \bar{u})] \right] \mathrm{d}z \tag{2.48}$$

2.4.3 Finite element approximation on Ω_x

Likewise, the introduction of Eq. 2.35 into the variational Eq. 2.33 leads to the linear system

$$([K_v] - [M_v])\,[q^v] = [F_v] - [R_v] \tag{2.49}$$

where $[q^v]$ is the vector of the nodal displacements associated with the mesh in Ω_x, $[K_v]$ and $[M_v]$ are the stiffness and mass matrices obtained by assembling the element stiffness and mass matrices $[K_v^e]$ and $[M_v^e]$ respectively, $[F_v]$ is the load vector obtained by assembling the element load vectors $[F_v^e]$ and $[R_v]$ is the equilibrium residual obtained by assembling the element residual vectors $[R_v^e]$ whose expressions are

$$[K_v^e] = \gamma_\omega \int_{\Omega_x^e} [B_x]^\top \left[\sum_{k=1}^{n_z} [k_z(\tilde{f}_k)]\right] [B_x]\,\mathrm{d}x \tag{2.50}$$

$$[M_v^e] = \alpha_\omega \int_{\Omega_x^e} [N_x]^\top \left[\sum_{k=1}^{n_z} [m_z(\tilde{f}_k)]\right] [N_x]\,\mathrm{d}x \tag{2.51}$$

$$[F_v^e] = \beta_\omega \int_{\partial_F \Omega_x^e} [N_x]^\top \left[\sum_{k=1}^{n_z} [f_z(\tilde{f}_k)]\right] \mathrm{d}x \tag{2.52}$$

$$[R_v^e] = \sum_{i=1}^{n-1} \gamma_\omega^i \int_{\Omega_x^e} [B_x]^\top \left[\sum_{k=1}^{n_z} [\sigma_z^i(\tilde{f}_k,\bar{u})]\right] \mathrm{d}x - \sum_{i=1}^{n-1} \alpha_\omega^i \int_{\Omega_x^e} [N_x]^\top \left[\sum_{k=1}^{n_z} [\mu_z^i(\tilde{f}_k,\bar{u})]\right] \mathrm{d}x \tag{2.53}$$

2.4.4 Solution over the number of enrichment steps

Finally, the problem for the whole beam using a discrete PGD framework can be expressed by the three following equations

$$g(\omega_j) = \frac{f_\omega + \omega_j^2 R_{\omega,M} - R_{\omega,K}}{k_\omega - \omega_j^2 m_\omega}, \quad \forall \quad j \in \{1, n_\omega\} \tag{2.54}$$

$$\Big([K_f] - [M_f]\Big)\,[q^f] = [F_f] - [R_f] \tag{2.55}$$

$$([K_v] - [M_v])\,[q^v] = [F_v] - [R_v] \tag{2.56}$$

which are equivalent to Eq. 2.20-2.22. This problem needs to be solved for each enrichment step $i = 1,2,...,n,...,N$ following a fixed point iteration scheme. At the first step of the fixed point method, vectors g and q^f are initialized and q^v is computed using Eq. 2.56. A key issue for the identification of different vibration modes is the initialization of the former vector, g. In this development, a different initialization is considered for each enrichment step n in the following manner

$$g^{(0)}(\omega_j) = \begin{cases} 0 & j \neq i \\ 1 & j = i \end{cases} \quad \text{with } i = \arg\min_j \mid \omega_j - \Psi \mid \tag{2.57}$$

and Ψ is defined as

$$\Psi = \omega_{min} + (n-1)\,\psi \quad \text{with} \quad \psi = \frac{\omega_{max} - \omega_{min}}{N-1}$$

where N is the total number of enrichment steps and $[\omega_{min}, \omega_{max}]$ is the considered load frequency range.

Regarding the initialization of q^f, a unity vector of size n_z is set for each enrichment step. After the computation of the vector q_v, the following steps of the fixed point algorithm are started by solving Eq. 2.54-2.56 successively. The computation is iterated m times until the following convergence criteria are satisfied simultaneously

$$|\omega_n^{(m)} - \omega_n^{(m-1)}| < \varepsilon_\omega \tag{2.58}$$

$$\max\left\{\frac{\|(q^f)^{(m)} - (q^f)^{(m-1)}\|_2}{\|(q^f)^{(m-1)}\|_2}, \frac{\|(q^v)^{(m)} - (q^v)^{(m-1)}\|_2}{\|(q^v)^{(m-1)}\|_2}\right\} < \varepsilon \tag{2.59}$$

being $\|\square\|_2$ the Euclidean norm and ε_ω and ε two different user-specified tolerances set to 10^{-2} and 10^{-6} in the following.

In this study, it has been noticed that the convergence at each enrichment step is not assured. It depends heavily on the number of vibration modes that the beam has in the studied load frequency range. Generally, a number of enrichment steps greater than the vibration modes present in the interval is needed. This means that some of the steps does not converge to a vibration mode. However, the information provided by this non-converging modes is important to reproduce the behaviour of the beam in terms of the anti-resonant peaks. For the converging modes, about 15 iterations of the fixed point method have been required, at worst. For the non-converging modes, the maximum number of iterations is reached, which is set to 25 in this study. At each iteration, one equation with n_ω unknowns and two linear systems of dimension $Ndof_x$ and $Ndof_z$ are solved. In a classical layerwise FE approach, the performance implies n_ω resolutions with $\frac{Ndof_x \times Ndof_z}{2}$ DOFs.

2.5 Numerical results

This section is dedicated to the analysis of some laminated and sandwich beams in order to evaluate the proposed approach in sections above. It should be noticed that the PGD method has been successfully used to solve static problems [62] of composite beams. This paper focuses on the harmonic analysis in the frequency domain, and the FRFs are first obtained by using the PGD method. Moreover, the proposed formulation also allows us to identify the modal parameters, natural frequencies and vibration modes.

Five different numerical test are analysed below. A great variety of boundary conditions is considered with wide range of slenderness ratios for symmetric, anti-symmetric composite beams and different types of sandwich beams. In the following test, as far as the spatial discretization is concerned, a classical quadratic FE approximation is considered for both domains Ω_x and Ω_z. A Gaussian numerical integration with three points is used to evaluate the elementary matrices and also to solve the integrals in load frequency domain. The results are compared with classical FE solutions and exact elastic solutions or theories available in open literature. The commercial FEA software ANSYS is employed in FE simulations to provide reference solutions. A bi-dimensional approach using the PLANE182 element with plane stress conditions is used. This element is defined by four nodes having two DOFs at each node.

2.5.1 Convergence study of the PGD algorithm

A convergence study with respect to the number of total enrichment steps is first carried out. Then, the effect of the mesh size on both spatial coordinates and the load position are analysed. For this purpose, a simple case of an isotropic beam is considered:

- *Geometry*: isotropic beam with $L = 10$ m and $h = 2$ m.
- *Material properties*: $E = 70\,\text{GPa}$, $\nu = 0.3$ and $\rho = 2700\,\text{kg/m}^3$.
- *Boundary conditions*: simply supported beam and harmonic concentrated load.
- *Reference solution*: A modal analysis with a 2D FE model is performed using ANSYS. A refined regular mesh with square elements of side $L/100$ is considered.

2.5.1.1 Number of total enrichment steps

The convergence study with respect to the number of total enrichment steps N is first developed. In Table 2.1, the mode shapes are denoted as *bend*, *sh*, *t/c* and *th* for bending, shear, extensional and thickness modes, respectively. The natural frequencies are presented under a dimensionless value computed as $\overline{\omega} = \omega_n LS\sqrt{\rho/E}$.

Table 2.1 Mode identification for different values of enrichment steps.

Mode	PGD					ANSYS	e_r(%)
	N=5	N=10	N=20	N=30	$\overline{\omega}$	$\overline{\omega}$	
bend	0	0	1	1	2.682	2.684	0.1
bend	0	0	1	1	9.336	9.346	0.1
t/c	1	1	1	1	15.684	15.685	0.0
bend	0	1	1	1	17.902	17.930	0.2
bend	1	0	1	1	27.249	27.307	0.2
th	0	1	1	1	31.198	31.203	0.0
bend	1	1	1	1	36.888	36.990	0.3
th	0	0	0	1	46.189	46.212	0.0
bend	0	0	1	1	46.609	46.771	0.3
sh	0	1	1	1	48.710	48.758	0.1

Note: 1 = identified mode; 0 = non-identified mode.

For PGD computations, a mesh of 50 elements on Ω_x domain and 10 elements on Ω_z is considered. The frequency search range is set to [40-800] Hz and the resolution to 1 Hz. The harmonic point load is applied at the top of the beam at a distance of $L/10$ from the support, and it has vertical and horizontal components with the same amplitude at each direction. The study confirms that when looking for modes within a relatively wide frequency range, it is necessary to consider a number of steps greater than the number of vibration modes within that interval to effectively cover the entire frequency range. In this case, when twenty steps are considered, the algorithm manages to find nine of the ten modes present in that frequency range. When the number of steps is increased to thirty, ten modes are identified. The relative errors (e_r) made in the value of the natural frequency are kept below 0.3% .

2.5.1.2 Spatial domain mesh

The convergence study with regard to the spatial domain mesh is carried out in this section. In the analysis, the frequency search range is reduced to [40-450] Hz because only the results for the first four modes are compared. In this case, it is enough to consider $N = 10$ enrichment steps. The frequency resolution is 1 Hz and a concentrated harmonic load is applied at the top of the beam at a distance of $L/10$ from the support, with vertical and horizontal components, as for the previous section. Table 2.2 shows the relative and cumulative errors of the first four natural frequencies for different meshes. Errors are calculated for the finest mesh considered as reference. Parameters S_x and S_z represent the relative mesh size in beam and thickness axis respectively. It can be inferred from Table 2.2 that the convergence rate is rather high and a mesh with $n_x = 20$ ($S_x = L/20$) and $n_z = 5$ ($S_z = h/5$) elements is sufficient to obtain converged results.

Table 2.2 Relative and cumulative errors (%) for the first four natural frequencies.

S_x \ S_z	h	h/5	h/10	h/20	Mode
	0.586	0.010	0.009	0.010	1
	1.719	0.054	0.051	0.050	2
L/10	0.009	0.001	0.001	0.001	3
	2.805	0.166	0.160	0.160	4
	5.12	**0.23**	**0.22**	**0.22**	cum.
	0.578	0.002	0.001	0.001	1
	1.671	0.006	0.003	0.003	2
L/20	0.002	0.000	0.000	0.000	3
	2.654	0.017	0.011	0.010	4
	4.90	**0.02**	**0.02**	**0.01**	cum.
	0.577	0.001	0.000	0.000	1
	1.668	0.003	0.000	0.000	2
L/50	0.002	0.000	0.000	0.000	3
	2.643	0.007	0.001	0.000	4
	4.89	**0.01**	**0.00**	**0.00**	cum.
	0.577	0.001	0.001	ref.	1
	1.668	0.003	0.000	ref.	2
L/100	0.002	0.000	0.000	ref.	3
	2.643	0.007	0.000	ref.	4
	4.89	**0.01**	**0.00**	-	cum.

2.5.1.3 Load position

The influence of the position and direction of the load applied is evaluated herein. Horizontal and vertical concentrated harmonic loads are considered separately, as well as different load application points. The converged PGD spatial mesh is used following Table

2.2. The frequency range and the number of enrichment steps are the same as in section 2.5.1.2. In Figure 2.2 , a simplified representation of the first five mode shapes of the isotropic beam are plotted with dashed line. Table 2.3 shows which of these five modes are identified when changing the direction and position of the load. The results report that when a vertical load is placed in the centre of the beam ($L/2$) the modes b and e are not excited. This is because for these modes the middle section of the beam, where the load is applied, does not move vertically. Analogously, when a horizontal load is placed in the middle of the beam, mode c cannot be identified because that section does not move horizontally. In view of these results, to ensure the identification of all modes, a load with both vertical and horizontal components should be considered and not located in a node.

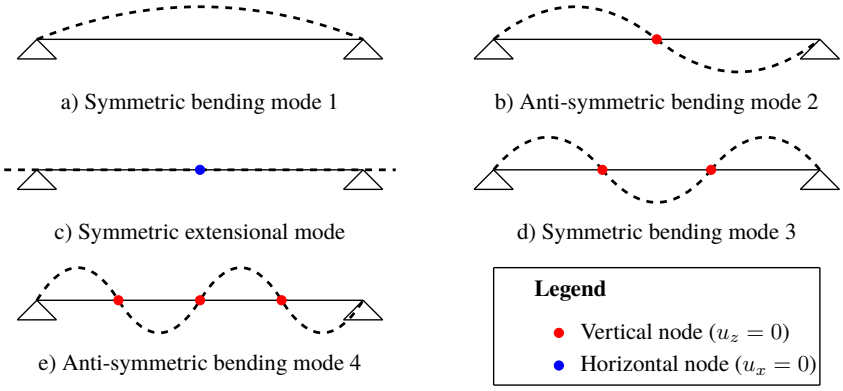

Figure 2.2 First five modal shapes of the isotropic beam with S=5.

Table 2.3 Mode identification for different load positions.

Mode	Vertical load			Horizontal load		
	L/10	L/4	L/2	L/10	L/4	L/2
a	1	1	1	0	0	0
b	1	1	0	0	0	0
c	0	0	1	1	1	0
d	1	1	1	0	0	0
e	1	0	0	0	0	0

Note: 1 = identified mode; 0 = non-identified mode.

2.5.2 Symmetric and anti-symmetric laminated beam

Herein, two symmetric and anti-symmetric composite cross-ply beams [68] are considered:

- *Geometry*: $(0^\circ/90^\circ/0^\circ)$ with thickness $0.25h/0.5h/0.25h$; $(0^\circ/90^\circ)$, being the two layers the same thickness; four length to thickness ratios $S = 2,5,10,20$.
- *Material properties*: $E_L = 181\,\text{GPa}$, $E_T = 10.3\,\text{GPa}$, $\nu_{LT} = 0.25$, $\nu_{TT} = 0.33$ and $\rho = 1578\,\text{kg/m}^3$. Subscripts L and T refer to the fibre and transverse directions.

- *Boundary conditions*: simply supported beam with a harmonic concentrated load placed on the top layer at a distance of $L/10$ from the first support.

The results are presented in a dimensionless form. The dimenssionless natural frequency is computed as $\overline{\omega} = \omega_n LS\sqrt{\rho/E_T}$. The numerical values obtained with the PGD method are compared with exact two-dimensional elasticity solution from [68] and results computed with the commercial FEA software ANSYS using a very refined mesh. For further information about the calculation parameters, please refer to the 2.7 section. Table 2.4 presents the values of the first seven natural frequencies for the thin to very thick of both symmetric and anti-symmetric beams. These results show the excellent agreement with reference values for all types of modes. The maximum relative error is below 0.86%.

Table 2.4 Dimensionless natural frequencies of the laminated beams.

S	Symmetric lay-up					Anti-symmetric lay-up			
	Mode	Exact [68]	ANSYS	PGD	e_r(%)	Mode	ANSYS	PGD	e_r(%)
	bend	-	3.447	3.447	0.0	*bend*	3.206	3.205	0.0
	sh	-	7.007	7.007	0.0	*bend*	7.406	7.404	0.0
	bend	-	7.689	7.686	0.0	*sh*	7.762	7.761	0.0
2	*th*	-	10.788	10.786	0.0	*th*	8.818	8.817	0.0
	bend	-	12.015	12.009	0.1	*bend*	10.987	10.982	0.0
	th	-	12.808	12.803	0.0	*th*	12.835	12.833	0.0
	th	-	14.966	14.963	0.0	*th*	13.465	13.462	0.0
	bend	6.806	6.808	6.806	0.0	*bend*	4.782	4.779	0.0
	bend	16.515	16.524	16.514	0.1	*bend*	14.653	14.638	0.1
	bend	26.688	26.718	26.688	0.1	*bend*	25.496	25.461	0.1
5	*bend*	37.255	37.323	37.256	0.2	*th*	35.396	35.382	0.0
	t/c	-	43.672	43.649	0.1	*bend*	36.181	36.119	0.2
	sh	-	43.807	43.793	0.0	*bend*	46.367	46.273	0.2
	bend	48.035	48.155	48.037	0.2	*sh*	48.536	48.505	0.0
	bend	9.343	9.347	9.343	0.0	*bend*	5.297	5.293	0.1
	bend	27.224	27.249	27.223	0.1	*bend*	19.150	19.117	0.2
	bend	46.416	46.485	46.417	0.1	*bend*	37.855	37.755	0.3
10	*bend*	66.058	66.195	66.056	0.2	*bend*	58.759	58.553	0.4
	bend	86.169	86.420	86.168	0.3	*bend*	80.478	80.134	0.4
	t/c	-	93.776	93.738	0.0	*t/c*	88.435	88.395	0.0
	bend	106.75	107.166	106.750	0.4	*bend*	102.350	101.842	0.5
	bend	10.64	10.649	10.640	0.1	*bend*	5.465	5.453	0.2
	bend	37.374	37.439	37.373	0.2	*bend*	21.234	21.171	0.3
	bend	71.744	71.939	71.743	0.3	*bend*	45.708	45.517	0.4
20	*bend*	108.89	109.293	108.895	0.4	*bend*	76.903	76.473	0.6
	bend	147.04	147.712	147.039	0.5	*bend*	112.951	112.486	0.4
	bend	185.68	186.712	185.681	0.6	*bend*	152.336	151.031	0.9
	t/c	-	190.553	190.491	0.0	*t/c*	187.926	187.863	0.0

Figures 2.4 and 2.3 represent the first six vibration modes for the very thick beams. The PGD algorithm is able to detect not only bending modes, but also shear and thickness modes with complex displacement distribution along either the beam axis or the thickness.

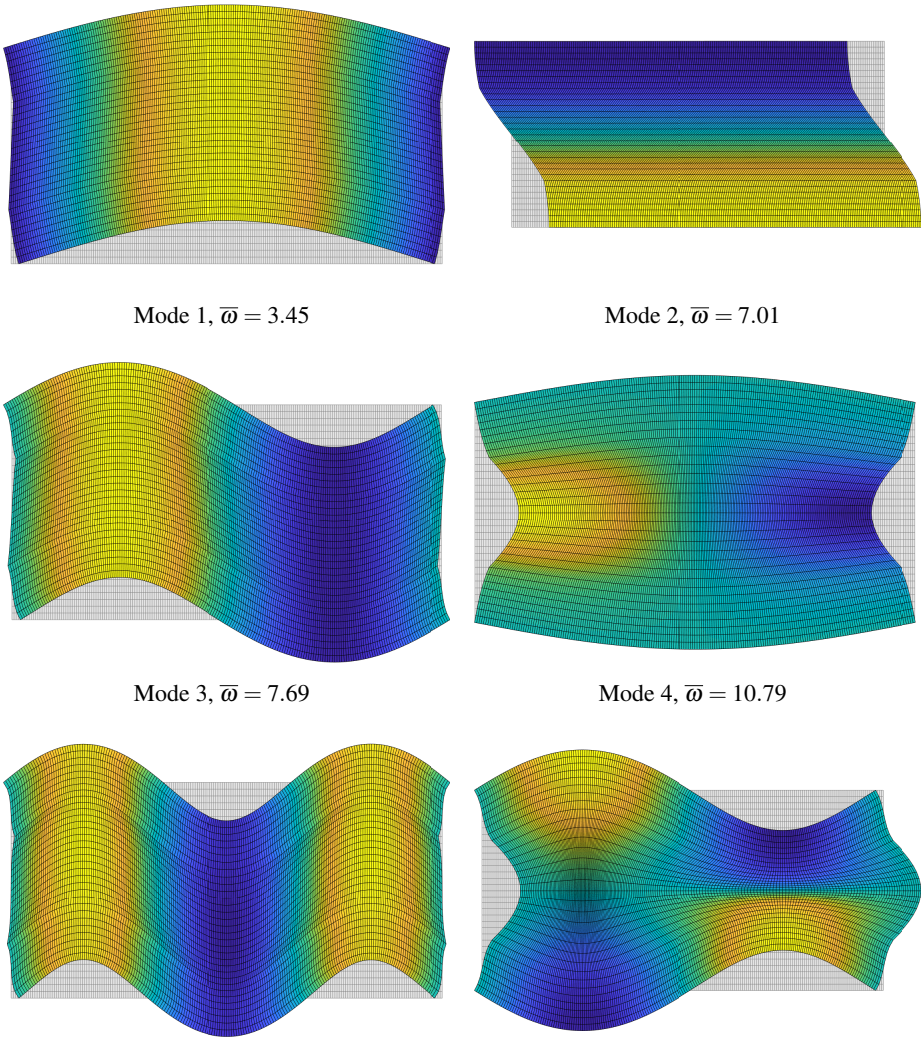

Mode 1, $\overline{\omega} = 3.45$ Mode 2, $\overline{\omega} = 7.01$

Mode 3, $\overline{\omega} = 7.69$ Mode 4, $\overline{\omega} = 10.79$

Mode 5, $\overline{\omega} = 12.01$ Mode 6, $\overline{\omega} = 12.80$

Figure 2.3 PGD solution for the symmetric laminated beam $(0^\circ/90^\circ/0^\circ)$ with $S = 2$.

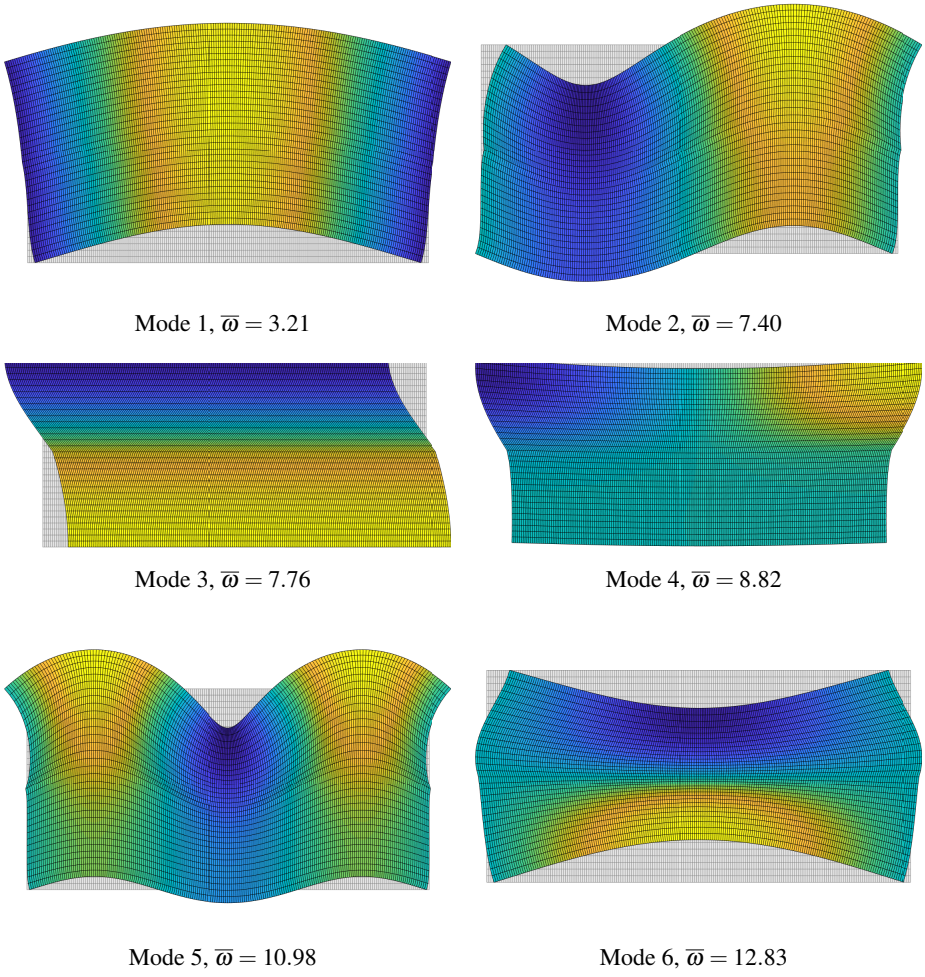

Figure 2.4 PGD solution for the anti-symmetric laminated beam $(0^\circ/90^\circ)$ with $S = 2$.

The main goal of this research is to solve the dynamic problem of a forced vibration beam subjected to a general harmonic excitation of frequency ω (Eq. 2.13). Damping is not considered in the formulation and the displacements are theoretically infinite for loads with a frequency equal to the resonance frequencies of the structure. The frequency response of a system can be represented in terms of displacement, velocity or acceleration considering different graphical representation: real and imaginary parts again frequency, Bode diagrams or Nyquist plot. Herein, the bode representation of displacement-force relationship, so-called receptance, is considered. In Figure 2.5 the FRF of vertical and horizontal displacements at the load application point are plotted for the symmetric laminated beam with $S = 5$. The first seven natural frequencies that appear in Table 2.4 can be

distinguished in this graphical representation.

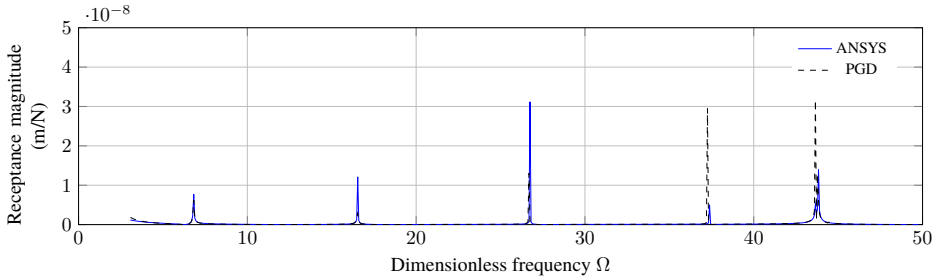

a) horizontal displacement

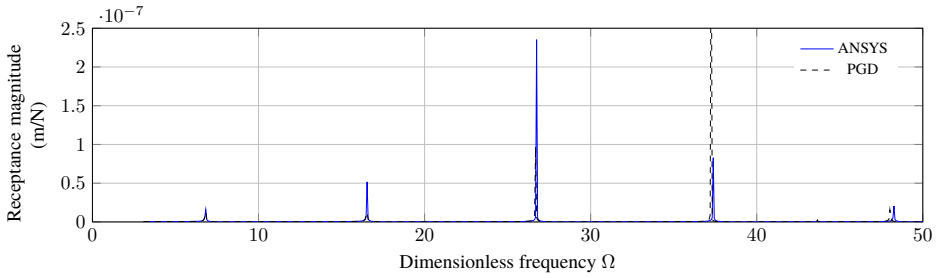

b) vertical displacement

Figure 2.5 FRF at loading point for the symmetric beam $(0^\circ/90^\circ/0^\circ)$ with $S = 5$.

In Figure 2.6, a detail of the horizontal displacement FRF (Figure 2.5a) in the range of $\overline{\omega} = [43-45]$ show that both extensional mode ($\overline{\omega} = 43.649$) and shear mode ($\overline{\omega} = 43.793$) have been identified despite having very similar natural frequency values.

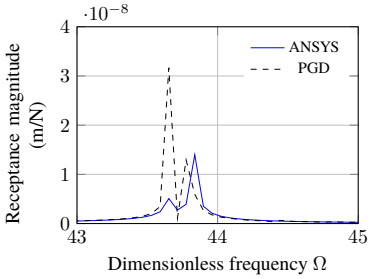

Figure 2.6 Detail of the FRF for the symmetric beam $(0^\circ/90^\circ/0^\circ)$ with $S = 5$.

Using the linear scale in magnitude-frequency graphs lead to lose detail of the response. Bode plots of the receptance amplitude in dB is depicted in the following. The value of the receptance α in dB is defined as $\alpha(\text{dB}) = 20\log_{10}(\alpha/\alpha_{ref})$ where α_{ref} is a reference value, assumed as unity in this study. Figure 2.7 shows the good agreement between the

amplitude of horizontal and vertical displacements at middle point of the beam calculated through a harmonic analysis in ANSYS and using the proposed PGD formulation. The most important difference between this representation and the previous one is that the anti-resonance peaks can be detected. This particular feature can be used to evaluate the validity of the computed FRF using the PGD method.

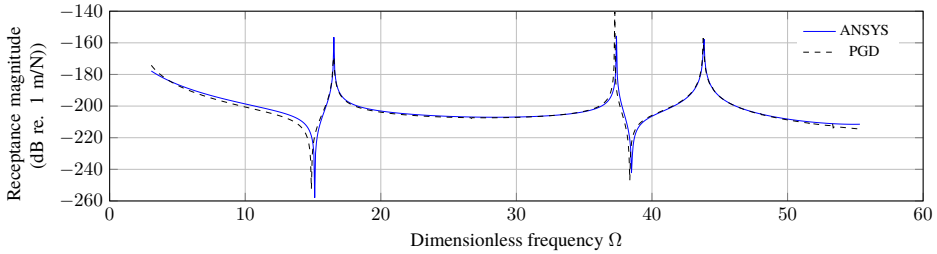

a) horizontal displacement

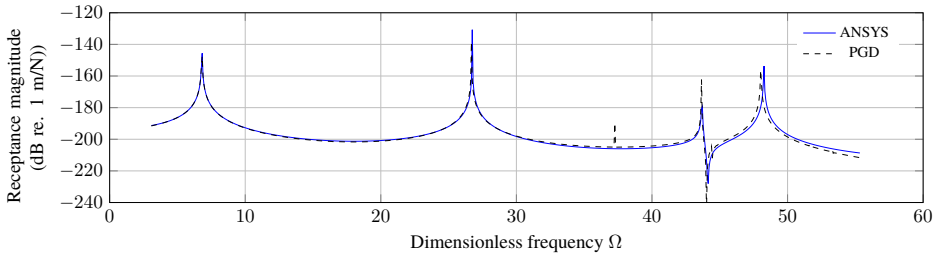

b) vertical displacement

Figure 2.7 FRF at bottom midpoint for the symmetric beam $(0^\circ/90^\circ/0^\circ)$ with $S = 5$.

2.5.3 Three-layer sandwich beam

In order to evaluate the PGD algorithm for solving problems in composite beams with layers of very different characteristics, the present test consists of a three-layer sandwich beam composed of two graphite-epoxy faces and a soft core [68]:

- *Geometry*: $0.1h/0.8h/0.1h$ and four length to thickness ratios $S = 2,5,10,20$.
- *Material properties*:

  Face: $E_{1f} = 131.1\,\text{GPa}$, $E_{2f} = E_{3f} = 6.9\,\text{GPa}$, $G_{12f} = 3.588\,\text{GPa}$,$G_{13f} = 3.088\,\text{GPa}$, $G_{23f} = 2.3322\,\text{GPa}$, $\nu_{12f} = \nu_{13f} = 0.32$, $\nu_{23f} = 0.49$ and $\rho_f = 1000\,\text{kg/m}^3$.

  Core: $E_{1c} = 0.2208\,\text{MPa}$, $E_{2c} = 0.2001\,\text{MPa}$, $E_{3c} = 2760\,\text{MPa}$, $G_{12c} = 16.56\,\text{MPa}$, $G_{13c} = 545.1\,\text{MPa}$, $G_{23c} = 455.4\,\text{MPa}$, $\nu_{12c} = 0.99$, $\nu_{13c} = \nu_{23c} = 0.00003$ and $\rho_c = 70\,\text{kg/m}^3$.
- *Boundary conditions*: simply supported beam with a harmonic concentrated load placed on the top layer at a distance of $L/10$ from the beam start.

The dimensionless natural frequency is computed as $\overline{\omega} = \omega_n LS\sqrt{(\rho_f/E_{2f})}$, where subscript f refers to the face material properties. The results are compared with exact 2D elasticity solution from [68] and results computed with ANSYS. The parameters used for the FE model and for the PGD simulation are provided in the section 2.7. Table 2.5 presents the values of the first seven natural frequencies for the thin to very thick three-layer sandwich beam. It can be noticed that the natural frequencies given by the PGD method are in excellent agreement with the reference elasticity solution in [68] for all types of modes, including thickness modes. Errors with respect to the ANSYS solution remain below 0.5 % for thin to thick beams ($S = 20,10,5$) and only go up to 1% for the very thick case ($S = 2$). Note that the refined sinus model [69], denoted with SinRef-7p, which includes the transverse normal deformation and the zig-zag effect, fails to predict the thickness mode with accuracy. As in the present formulation, the use of LW approach is required. Figure 2.8 represents the first three thickness modes for the very thick beam. As it can be observed, even non-symmetrical modes (cf. mode 4) can be obtained with PGD formulation.

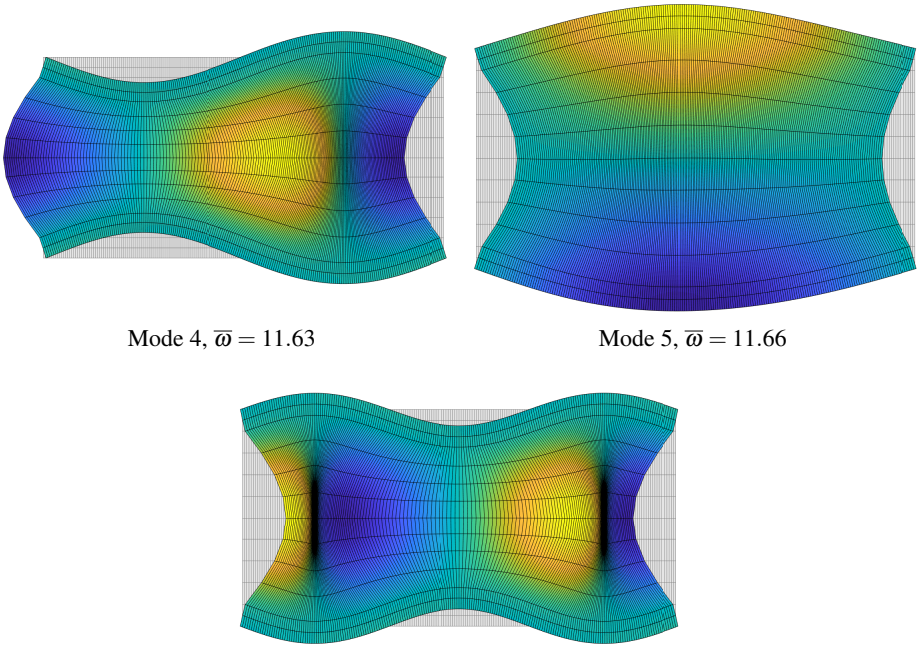

Mode 4, $\overline{\omega} = 11.63$ Mode 5, $\overline{\omega} = 11.66$

Mode 7, $\overline{\omega} = 12.16$

Figure 2.8 PGD solution of thickness modes for the sandwich beam with $S = 2$.

Table 2.5 Dimensionless natural frequencies of the three layer sandwich beam.

S	Mode	Exact 2D [68]	ANSYS	PGD	e_r(%)	SinRef-7p	e_r(%)
	bend	-	3.519	3.521	0.0	3.53	0.2
	sh	-	5.340	5.340	0.0	5.34	0.1
	bend	-	7.531	7.562	0.4	7.60	0.2
2	*th*	-	11.599	11.627	0.2	11.07	4.0
	th	-	11.663	11.664	0.0	9.40	19.0
	bend	-	11.823	11.954	1.1	11.97	0.2
	th	-	12.036	12.161	1.0	15.00	24.0
	bend	7.8227	7.817	7.815	0.0	7.83	0.1
	bend	17.274	17.253	17.247	0.0	17.31	0.1
	bend	26.903	26.854	26.847	0.0	26.97	0.2
5	*sh*	-	33.377	33.372	0.0	33.37	0.1
	bend	36.937	36.838	36.844	0.0	37.06	0.1
	bend	47.397	47.223	47.265	0.1	47.58	0.1
	bend	58.221	57.944	58.052	0.2	-	-
	bend	12.237	12.235	12.230	0.0	12.26	0.1
	bend	31.291	31.281	31.260	0.1	31.33	0.1
	bend	50.218	50.205	50.154	0.1	50.31	0.1
10	*bend*	68.096	69.088	68.990	0.1	69.26	0.1
	bend	88.18	88.190	88.021	0.2	88.51	0.1
	bend	107.61	107.660	107.389	0.3	108.25	0.2
	t/c	-	120.032	120.018	0.0	121.11	0.9
	bend	15.382	15.389	15.379	0.1	15.41	0.2
	bend	48.948	48.989	48.922	0.1	49.04	0.1
	bend	86.902	87.010	86.833	0.2	87.07	0.1
20	*bend*	125.16	125.374	125.042	0.3	-	-
	bend	163.12	163.479	162.941	0.3	163.69	0.1
	bend	200.87	201.423	200.618	0.4	201.94	0.1
	bend	-	239.387	238.243	0.5	-	-

Figures 2.9 and 2.10 represent the FRF of vertical and horizontal displacements separately, at the load application point and at the bottom midpoint of the beam, respectively. In these figures, only the response of the beam with a slenderness ratio of S=10 is represented. In this case, the first six natural frequencies correspond to six bending modes, as it is remarked in Table 2.5. The differences between these two below figures are quite remarkable. In Figure 2.9, almost all natural frequencies can be identified in both vertical and horizontal displacement, but it is not the same in Figure 2.10. This is due to the fact that the vibration nodes of various bending modes are located at the central point of the beam. Regarding symmetrical vibration bending modes (odd modes), they do not have horizontal displacement but vertical displacement at bottom midpoint of the beam as it can be observed in Figure 2.10b. Conversely, for the anti-symmetric bending modes (even modes) the opposite occurs, cf. Figure 2.10a. The PGD results are in good concordance with ANSYS solution.

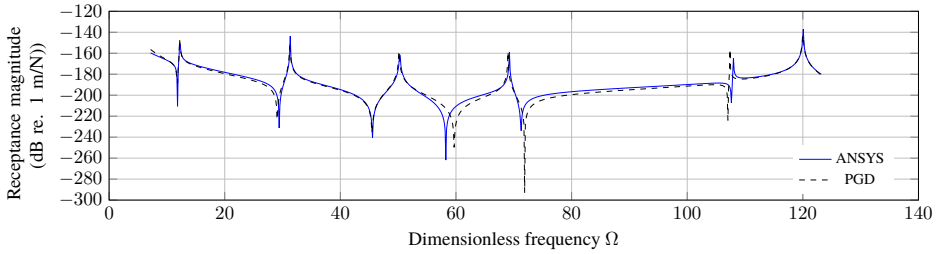

a) horizontal displacement

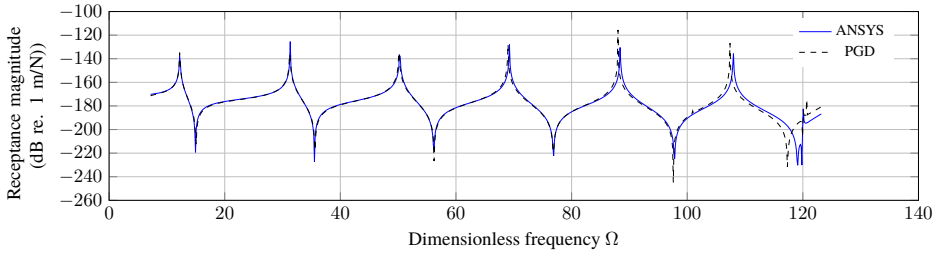

b) vertical displacement

Figure 2.9 FRF at loading point for the three-layer sandwich beam with $S = 10$.

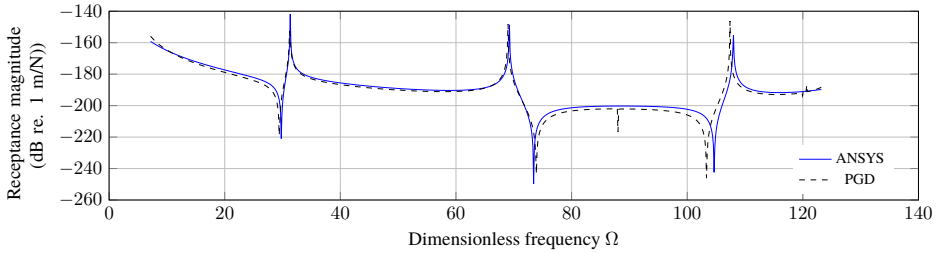

a) horizontal displacement

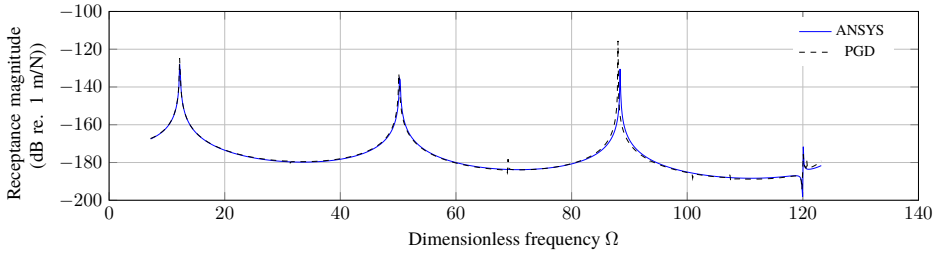

b) vertical displacement

Figure 2.10 FRF at bottom midpoint for the three-layer sandwich beam with $S = 10$.

2.5.4 Unsymmetric sandwich beam

The aim of this section is to compare the results of the PGD method with other theories in the literature. A sandwich beam analysed in the reference [40] is chosen as a test. This is a sandwich beam composed of two laminated faces with a isotropic core between them. Each face is composed of two layers with a stacking sequence of $0^\circ/90^\circ/\text{core}/0^\circ/90^\circ$.

- *Geometry*: Five layers of thickness $0.5h_f/0.5h_f/h_c/0.5h_f/0.5h_f$ with $h_c/h_f = 10$ and two length to thickness ratios $S = 4{,}10$.
- *Material properties*:

  Face laminated: $E_{1f} = 131.1\,\text{GPa}$, $E_{2f} = E_{3f} = 10.34\,\text{GPa}$, $G_{12f} = G_{23f} = 6.895\,\text{GPa}$, $G_{13f} = 6.205\,\text{GPa}$, $\nu_{12f} = \nu_{13f} = 0.22$, $\nu_{23f} = 0.49$ and $\rho_f = 1627\,\text{kg/m}^3$.

  Core: $E_c = 6.89\,\text{MPa}$, $G_c = 3.45\,\text{MPa}$, $\nu_c = 0$ and $\rho_c = 97\,\text{kg/m}^3$.
- *Boundary conditions*: simply supported beam with a vertical harmonic load placed on the top layer at a distance of $L/10$ from the beam start.

Table 2.6 presents the values of the first four bending frequencies for the thick and semi-thick unsymmetric sandwich beam. The frequencies are displayed in dimensionless form as in section 2.5.3. The results obtained with the PGD method are compared with those obtained applying three models reported from [40, 69] denoted as: i) GLHT, global-local-higher order theory [70]; ii) ZZT, zig-zag theory with continuous transverse shear stress at interfaces [41] and iii) SinRef-7p, refined sinus model satisfying the continuity of transverse shear stress at interfaces with seven independent generalized displacements [69]. A 2D FE model of the unsymmetric sandwich beam has also been developed and used as reference for the comparison (see ANSYS and PGD calculation parameters detailed in 2.7). It can be noticed that the natural frequencies obtained with the PGD method are in excellent agreement with the reference solution for both thick and semi-thick beams. The error rate is less than 0.12%. This example highlights the limitations of high-order ESL models for such structures, especially for the thick case. In contrast, the present LW approach based on the variable separation is well-adapted.

Table 2.6 Dimensionless natural frequencies of the unsymmetric sandwich beam.

S	Mode	ANSYS	PGD		SinRef-7p		GLHT		ZZT	
		$\overline{\omega}$	$\overline{\omega}$	$e_r(\%)$	$\overline{\omega}$	$e_r(\%)$	$\overline{\omega}$	$e_r(\%)$	$\overline{\omega}$	$e_r(\%)$
4	*bend 1*	0.614	0.614	0.1	0.645	5.0	0.638	4.0	0.616	0.3
	bend 2	1.762	1.763	0.1	1.819	3.2	1.800	2.2	1.772	0.6
	bend 3	3.569	3.572	0.1	3.674	2.9	3.631	1.7	3.621	1.5
	bend 4	5.795	5.802	0.1	6.223	7.3	6.133	5.8	6.186	6.8
10	*bend 1*	1.282	1.283	0.1	1.361	6.1	1.347	5.0	1.282	0.0
	bend 2	2.868	2.870	0.1	3.026	5.5	2.994	4.4	2.875	0.2
	bend 3	4.951	4.954	0.1	5.183	4.6	5.126	3.5	4.971	0.4
	bend 4	7.649	7.653	0.0	7.961	4.0	7.861	2.7	7.686	0.4

2.5.5 Influence of boundary conditions

Lastly, to validate the PGD algorithm for different boundary conditions, a symmetric laminated composite beam with a stacking sequence $0^\circ/90^\circ/0^\circ$ is analysed:

- *Geometry*: Three layers of equal thickness and a length to thickness ratio $S = 5$.
- *Material properties*: $E_L/E_T = 40$, $G_{LT} = 0.2 \cdot E_T$, $G_{TT} = 0.5 \cdot E_T$, $\nu_{LT} = 0.25$, $\nu_{TT} = 0.33$ and $\rho = 1\,\text{kg/m}^3$.
- *Boundary conditions*: beam with a harmonic concentrated load placed on the top layer at a distance of $L/10$ from the beam start and six different support cases:

  free/free (FF), clamped/clamped (CC), simply support/free (SF), clamped/simply support (CS), simply support/simply support (SS) and clamped/free (CF).

The PGD solution is compared with the results of SinRef-7p model from [69] and with those calculated in [71] using theories named as: i) PSDBT, parabolic shear deformation beam theory and ii) HSDBT, hyperbolic shear deformation beam theory, with continuous/discontinuous inter-laminar stresses (cs/ds). As in the previous section, a FE model of the symmetric laminated beam with the different boundary conditions is analyzed. A unity value of parameter E_T is set for the analysis. The rest of the parameters of the FE model and those referring to the resolution using the PGD method can be found in section 2.7. Table 2.7 shows the fundamental dimensionless natural frequencies.

Table 2.7 Fundamental dimensionless frequencies for different boundary conditions.

		FF	CC	SF	CS	SS	CF
ANSYS	$\overline{\omega}$	19.097	10.757	13.465	9.825	9.200	4.153
PGD	$\overline{\omega}$	19.225	10.816	13.875	10.056	9.199	4.218
	e_r(%)	0.7	0.6	3.0	2.4	0.0	1.6
SinRef-7p	$\overline{\omega}$	19.123	11.100	13.472	10.000	9.201	4.189
	e_r(%)	0.1	3.2	0.1	1.8	0.0	0.9
PSDBT$_{cs}$	$\overline{\omega}$	18.976	11.446	13.206	10.032	8.968	4.158
	e_r(%)	0.6	6.4	1.9	2.1	2.5	0.1
HSDBT$_{cs}$	$\overline{\omega}$	18.955	11.427	13.195	10.021	8.964	4.157
	e_r(%)	0.7	6.2	2.0	2.0	2.6	0.1
PSDBT$_{ds}$	$\overline{\omega}$	19.391	11.637	13.538	10.236	9.207	4.233
	e_r(%)	1.5	8.2	0.5	4.2	0.1	1.9
HSDBT$_{ds}$	$\overline{\omega}$	19.401	11.625	13.538	10.229	9.207	4.232
	e_r(%)	1.6	8.1	0.5	4.1	0.1	1.9
Minimum error		**0.1**	**0.6**	**0.1**	**1.8**	**0.0**	**0.1**
Model		SinRef-7p	PGD	SinRef-7p	SinRef-7p	PGD	HSDBT$_{cs}$

As a general remark, the highest frequencies occur for the free/free boundary condition and the lowest values is obtained for the cantilever beam. For the models with continuous

inter-laminar stresses (SinRef-7p included), the frequencies for the PGD model are always higher than those of the two other models, except for the CC condition. Concerning the models with discontinuous inter-laminar stresses, the PGD results are always lower than the two other discontinuous models, except for the SF condition. The differences between PGD solution and those obtained with the models remain always low. With respect to the ANSYS solution for a very refined mesh of 3375 elements, the PGD method solution is the best fit for SS and CC cases. For the other cases, PGD errors do not exceed 3%.

2.6 Conclusions

This paper investigates a new methodology based on the PGD method to solve the forced vibration problem in bi-dimensional laminated beams. A classical harmonic space-frequency description of the dynamic problem is considered and a variable separation in the spatial domain is introduced. For both spatial coordinates x (beam axis coordinate) and z (thickness coordinate), a classical 3-node FE is used in the discretization while a linear interpolation is introduced for the load frequency ω. The derived iterative algorithm implies the computation of three 1D functions at each iteration where the total cost depends on the number of enrichment steps N used to represent the solution. Specifically the proposed process requires, for each enrichment step, a small number of iterations m of the fixed point method which involves the resolution of one equation with n_ω unknowns and two linear systems of $Ndof_x$ and $Ndof_z$ DOFs respectively. In a classical layerwise FE approach, the calculation implies n_ω resolutions with $\frac{Ndof_x \times Ndof_z}{2}$ DOFs. The advantages of the proposed algorithm become relevant when the number of numerical layers and the number of elements in axis direction increases.

The new approach has been used to solve numerical tests, including composite and sandwich beam configurations with a great variety of slenderness ratios and boundary conditions. Results show a good agreement with exact elasticity solutions, higher-order theories and FE models. This study has showed the capability of the method to build all kinds of mode shapes, including complex thickness modes with non-uniform displacement distribution along x and z axis. This is possible owing to the actual LW approach.

2.7 Notes on chapter: numerical test parameters

Table 2.8 PGD calculation parameters.

Numerical test	L (m)	S	n_x	n_z (per layer)	f_{min} (Hz)	f_{max} (Hz)	Δf (Hz)	N
Isotropic beam								
N analysis	10	5	50	10	40	800	1	-
Spatial mesh analysis	10	5	-	-	40	450	1	10
Load position analysis	10	5	50	10	40	450	1	10
Symmetric laminated composite beam	1	2	100	[4,8,4]	600	4200	1	30
	1	5	100	[4,8,4]	500	5000	1	30
	1	10	100	[4,8,4]	300	4500	1	30
	1	20	100	[2,4,2]	100	4000	1	30
Anti-symmetric laminated composite beam	1	2	100	[8,8]	600	3000	1	50
	1	5	100	[8,8]	300	4000	1	50
	1	10	100	[8,8]	200	4200	1	30
	1	20	100	[4,4]	100	4000	1	30
Three layer sandwich beam	1	2	100	[1,2,1]	500	5000	1	30
	1	5	100	[1,2,1]	500	5000	1	30
	1	10	100	[1,2,1]	450	5500	1	30
	1	20	100	[1,2,1]	250	5500	1	40
Unsymmetric sandwich beam	1	4	100	[1,1,5,1,1]	50	600	1	30
	1	10	100	[1,1,5,1,1]	40	350	1	30
Boundary condition analysis								
FF	1	5	100	[2,2,2]	0.01	1	0.01	10
CC	1	5	100	[2,2,2]	0.01	0.5	0.01	10
SF	1	5	100	[2,2,2]	0.01	0.5	0.01	5
CS	1	5	100	[2,2,2]	0.01	0.5	0.01	5
SS	1	5	100	[2,2,2]	0.01	0.5	0.01	10
CF	1	5	100	[2,2,2]	0.01	0.3	0.01	10

Note: the load frequency range in the PGD performance is $[\omega_{min},\omega_{max}]$, with $\omega_{min} = 2\pi f_{min}$ and $\omega_{max} = 2\pi f_{max}$.

Table 2.9 Parameters of the finite element models using ANSYS.

Numerical test	L (m)	S	Relative element size	Number of elements
Isotropic beam	10	5	L/100	2000
Symmetric laminated composite beam	1	2	L/125	8000
	1	5	L/125	3375
	1	10	L/125	1875
	1	20	L/125	1000
Anti-symmetric laminated composite beam	1	2	L/125	8000
	1	5	L/125	3250
	1	10	L/125	1750
	1	20	L/125	1000
Three layer sandwich beam	1	2	L/125	8000
	1	5	L/125	3250
	1	10	L/125	1750
	1	20	L/125	875
Unsymmetric sandwich beam	1	4	L/384	36864
	1	10	L/720	51840
Boundary condition analysis	1	5	L/125	3375

3 Forced vibration analysis of composite beams with piezoelectric layers based on the variable separation method

Title:	Forced vibration analysis of composite beams with piezoelectric layers based on the variable separation method
Authors:	M Infantes, P Vidal, R Castro-Triguero, L Gallimard, O Polit
Journal:	Composite Structures
ISSN:	0263-8223
JCR:	Impact Factor = 6.603, Q1 (Mechanics 8 / 138)
Details:	Volume: 273, article number 114248. Published online June 11, 2021
DOI:	j.compstruct.2021.114248

3.1 Introduction

Recently, it should be noted an increasing interest towards high-performance structures involving multifunctionality capabilites, as it has been pointed out in [72]. Not only structural but also non-structural functions represent the key issue in the develepment of such smart structural components. Electrical and thermal conductivity, sensing and actuation, energy harvesting and storage, self-healing, electromagnetic interference shielding, recyclability or biodegradability are some of the most promising multifunctionality capabilities [73]. An overview on the topics of smart structures can be found in [74, 75]. As they will be involved in the present work, piezoelectric materials permit to convert mechanical and electrical energy at frequency ranges. Among others, SHM, active vibration damping, rapid shape adaptation or energy harvesting [76] are only some feasible applications of such smart piezoelectric components. Due to the complex manufacturing of such structural devices, a reliable numerical analysis tool is necessary to capture all the relevant phenomena that guide the design process. Some examples of recent numerical studies

regarding the electro-mechanical analysis of piezoelectric energy harvesters are shown in [77–79]. Furthermore, if optimization processes and runtime control algorithms are addressed, the numerical simulation tool should be as robust and efficient as possible.

Various mathematical models developed for structures containing piezoelectric sensors and actuators can be classified into two broad categories including induced strain models and coupled electromechanical models. An overview on the modelling of piezoelectric structures is given in [75, 80–83]. On the one hand, the induced strain models use approximate theories in order to incorporate external forces associated with the piezoelectric actuators. The electric potential is neglected as a state variable in the formulation; therefore these models cannot capture the coupled mechanical and electrical responses and are only limited to predict the actuator behavior of piezoelectric materials ([84–87]). On the other hand, the coupled electromechanical models provide a more consistent representation of both the sensor and actuator responses of piezoelectric materials, incorporating both the displacements and the electric potentials as the state variables in the formulation. Piezoelectric three-dimensional (3D) finite elements have been early proposed in [88–90]. However, the cost of 3D analysis becomes prohibitive when piezoelectric layers are thin compared to the structure size.

In order to overcome these restrictions, several theories for laminated structures including piezoelectric elements have been developed in the literature. A LW description is commonly used for the piezoelectric part (see [91]), therefore, the discussion concerns only the mechanical approach. The following classification is associated with the dependence on the number of mechanical DOFs with respect to the number of layers:

- The ESL approach: the number of unknowns is independent of the number of layers, but continuity of transverse shear and normal stresses is often violated at layer interfaces. This approach is called ”hybrid” or ”mixed” in the literature. We can distinguish CLT, FSDT [92–94] and higher-order theories. In the latter, the third-order shear deformation theory has been carried out in [95–98]. Other types of functions can be also considered as in [99] (exponential function). See also a refined Reissner-Mindlin approach taking into account the stretching effect [83].
- The LW approach: the number of DOFs depends on the number of layers. This theory aims at overcoming the ESL shortcoming of allowing discontinuity of out-of-plane stresses on the interface layers. See for instance [100, 101] for beams, [102–106] for plates, and [107] for shells. Note that an extensive assessment has been provided by Saravanos and Heyligher [81].

In this framework, refined models have been developed in order to improve the accuracy of ESL models while avoiding the computational burden of the LW approach. Starting from a refined layerwise description, some physical considerations can be introduced. Then, after some algebraic transformations, the number of unknowns becomes independent of the number of layers. This type of approach has been carried out in [108]. The resulting model can be classified as a zig-zag one (see the historical review of [47]). In the framework of electromechanical problems, Oh and Cho [109] have extended the third order zig-zag model. Note also the works of Kapuria for beams [110, 111] and plates [112].

Finally, the so-called advanced models based on the Principle of Virtual Displacements (PVD), the Reissner Mixed Variational Theorem (RMVT) and CUF must be referred here.

Different types of interlaminar continuity can be considered: transverse shear/normal stresses and/or transverse electric displacement. For the works related to multilayered piezoelectric structures, readers can refer to [113, 114] for plates and [82] for shells.

A promising alternative approach to reduce the computational cost in the field of the reduced-order modelling is based on the separation of variables [22]. It has been proposed in [115] with a Navier-type solution for the modelling of composite plates with a in-plane/out-of-plane coordinates separation. Such variable separations have been successfully applied to composite structures in static case [60, 63]. The forced vibration problem of composite beams subjected to harmonic excitation has also been considered previously by the authors of this study by using the PGD framework [116]. In the latter reference, the displacements are written under the form of separated variable representation, i.e. a sum of products of unidimensional functions of x and z coordinates. The load frequency ω was introduced into the formulation as another problem variable, in order to achieve a more robust formulation. The aim of the present paper is to extend the previously developed method to laminated and sandwich beams with piezoelectric layers. Therefore, a multi-field analysis of advanced composite structures is addressed, especially dedicated to the consideration of electro-mechanical coupling. Analogously, herein both displacements and electric potential are written under the form of a sum of products of x functions, z functions and load frequency functions. The deduced explicit solution allows us to avoid numerous classical computations for each discretized value of the load frequency in the study domain. To achieve that, the approximation of the 2D beam is based on a quadratic FE approximation for the variation with respect to x and a quadratic layerwise description for the variation with respect to z. The electric unknowns are interpolated with a second-order expansion. Using the PGD, each unknown function of x is classically approximated using one DOF at the node of the mesh while the LW unknown functions of z are global for the whole beam. Finally, the deduced non-linear problem implies the resolution of three 1D linear problems alternatively. This process yields to few unknowns involved in each of these linear problems.

The manuscript is organized as follows. First, the electro-mechanical formulation is recalled. Then, the particular assumption on the displacements and the electric potential is introduced. It leads to a non-linear problem to be solved. An iterative process based on a classical fixed point strategy allows us to obtain the coupling solution. In this process, three 1D linear problems described in the present work, have to be solved. The FE discretization is also given. Numerical evaluations are subsequently presented. A convergence study of the proposed algorithm is first conducted. Several numerical tests with wide range of slenderness ratios under various boundary conditions are considered in order to assess the validity of the method. The results in terms of modal parameters and FRFs are compared with exact elasticity solution and FE simulations from a commercial FEA software.

3.2 Reference problem description

In the present study, a composite beam of length L and thickness h is considered. The beam consists of NC layers assumed to be orthotropic in the beam axes. In addition, some of the layers are assumed to present a piezoelectric behavior. The beam is considered in the

(x,z) plane, i.e., in the domain $\Omega = \Omega_x \times \Omega_z = [0 \leq x \leq L] \times [-h/2 \leq z \leq h/2]$. The x axis is taken along the longitudinal beam axis whereas the z axis is taken along the thickness direction. The reader can refer to Figure 3.1, where the coloured areas represent layers of piezoelectric material. The main notation used throughout the present formulation is also given in the chapter on Notation in the preamble of this document.

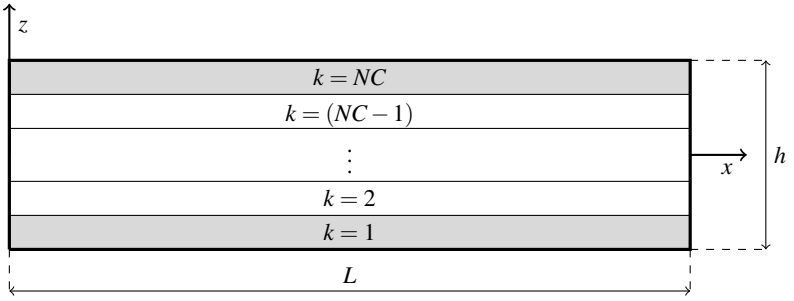

Figure 3.1 The laminated beam with piezoelectric layers and coordinate system.

The governing equations of the piezoelectric problem are given by

$$\nabla \cdot [\sigma] + [b] = \rho \frac{\partial^2 [u]}{\partial t^2} \tag{3.1a}$$

$$\nabla \cdot [D] - q = 0 \tag{3.1b}$$

where $[\sigma]$ is the stress, $[u]$,$[D]$ are the mechanical and electric displacement respectively, $[b]$ is the body load, q is free electric volume charge and ρ refers to the material the density. The two-dimensional formulation of the piezoelectric problem can be reduced to

$$\frac{\partial \sigma_{11}}{\partial x} + \frac{\partial \sigma_{13}}{\partial z} = \rho \frac{\partial^2 u_1}{\partial t^2}, \qquad \frac{\partial \sigma_{13}}{\partial x} + \frac{\partial \sigma_{33}}{\partial z} = \rho \frac{\partial^2 u_3}{\partial t^2}, \qquad \frac{\partial D_1}{\partial x} + \frac{\partial D_3}{\partial z} = 0 \tag{3.2}$$

where body load and free electric volume charge have been neglected for simplification purposes.

3.2.1 Constitutive relation

The constitutive equations with piezoelectric coupling for a layer k read

$$[\sigma] = [\bar{C}_k][\varepsilon] - [\bar{e}_k]^\top [E] \tag{3.3a}$$

$$[D] = [\bar{e}_k][\varepsilon] + [\bar{\varepsilon}_k][E] \tag{3.3b}$$

where $[\varepsilon] = [\varepsilon_{11}\ \varepsilon_{33}\ \gamma_{13}]^\top$ is the strain and $[E] = [E_1\ E_3]^\top$ is the electric field for the 2D formulation. Assuming plane stress in the xy-plane and also vanishing out of plane electric

displacement, the reduced constitutive matrices can be computed for each layer k by

$$[\bar{C}_k] = \begin{bmatrix} C_{11}^{(k)} & C_{13}^{(k)} & 0 \\ C_{13}^{(k)} & C_{33}^{(k)} & 0 \\ 0 & 0 & C_{55}^{(k)} \end{bmatrix} - \begin{bmatrix} C_{12}^{(k)} & 0 & C_{16}^{(k)} \\ C_{23}^{(k)} & 0 & C_{36}^{(k)} \\ 0 & C_{45}^{(k)} & 0 \end{bmatrix} \begin{bmatrix} C_{22}^{(k)} & 0 & C_{26}^{(k)} \\ 0 & C_{44}^{(k)} & 0 \\ C_{26}^{(k)} & 0 & C_{66}^{(k)} \end{bmatrix}^{-1} \begin{bmatrix} C_{12}^{(k)} & C_{23}^{(k)} & 0 \\ 0 & 0 & C_{45}^{(k)} \\ C_{16}^{(k)} & C_{36}^{(k)} & 0 \end{bmatrix} \tag{3.4}$$

$$[\bar{e}_k] = \begin{bmatrix} 0 & 0 & e_{15}^{(k)} \\ e_{31}^{(k)} & e_{33}^{(k)} & 0 \end{bmatrix} - \begin{bmatrix} 0 & 0 & 0 \\ e_{32}^{(k)} & 0 & 0 \end{bmatrix} \begin{bmatrix} C_{22}^{(k)} & 0 & C_{26}^{(k)} \\ 0 & C_{44}^{(k)} & 0 \\ C_{26}^{(k)} & 0 & C_{66}^{(k)} \end{bmatrix}^{-1} \begin{bmatrix} C_{12}^{(k)} & C_{23}^{(k)} & 0 \\ 0 & 0 & C_{45}^{(k)} \\ C_{16}^{(k)} & C_{36}^{(k)} & 0 \end{bmatrix} \tag{3.5}$$

$$[\bar{\varepsilon}_k] = \begin{bmatrix} \varepsilon_{11}^{(k)} & 0 \\ 0 & \varepsilon_{33}^{(k)} \end{bmatrix} + \begin{bmatrix} 0 & 0 & 0 \\ e_{32}^{(k)} & 0 & 0 \end{bmatrix} \begin{bmatrix} C_{22}^{(k)} & 0 & C_{26}^{(k)} \\ 0 & C_{44}^{(k)} & 0 \\ C_{26}^{(k)} & 0 & C_{66}^{(k)} \end{bmatrix}^{-1} \begin{bmatrix} 0 & e_{32}^{(k)} \\ 0 & 0 \\ 0 & 0 \end{bmatrix} \tag{3.6}$$

being $C_{ij}^{(k)}$ the stiffness coefficients, $e_{ij}^{(k)}$ the piezoelectric constants and $\varepsilon_{ij}^{(k)}$ the permittivity coefficients for the 3D problem.

3.2.2 New variational formulation

For a single harmonic mechanical excitation $[F_d] = [f_d] \cdot e^{i\omega t}$ applied in $\partial_F \Omega$, the response of a linear solid in absence of body loads and free electric volume charge is presumed to have the same frequency as the applied load

$$[u(t)] = [u] \cdot e^{i\omega t}, \qquad \phi(t) = \phi \cdot e^{i\omega t} \tag{3.7}$$

with $[u]$ and ϕ containing the displacements and electric potential amplitudes. For a set of the load frequency within an interval $[\omega_{min}, \omega_{max}]$ a new robust variational formulation is proposed herein. The problem is defined as finding $([u(\omega)], \phi(\omega)) \in U \times \Phi$ (space of admissible generalized displacement) such that $\forall\, ([\delta u],\, \delta\phi) \in \delta U \times \delta\Phi$

$$\int_\omega \int_\Omega [\varepsilon(\delta u)]^\top [\sigma] \,\mathrm{d}V \,\mathrm{d}\omega - \int_\omega \int_{\partial_F \Omega} [\delta u]^\top [f_d] \,\mathrm{d}S \,\mathrm{d}\omega = \int_\omega \int_\Omega \omega^2 \rho [\delta u]^\top [u] \,\mathrm{d}V \,\mathrm{d}\omega \tag{3.8a}$$

$$\int_\omega \int_\Omega [E(\delta\phi)]^\top [D] \,\mathrm{d}V \,\mathrm{d}\omega = 0 \tag{3.8b}$$

Using kinematic relations, $[\varepsilon] = 1/2\{\nabla[u] + \nabla[u]^\top\}$, and Maxwell's law to derive the electric field vector from the electric potential,$[E] = -\nabla\phi$, the piezoelectric problem can be reformulated only in terms of the generalized displacements $([u],\, \phi)$. To complete the boundary value problem, a prescribed displacement $[u] = [u_d]$ and electric potential $\phi = \phi_d$ are imposed on $\partial_u \Omega$ and $\partial_\phi \Omega$ respectively.

3.3 Separated representation

In the approach carried out in this study, the unknowns of the problem, i.e., the displacements $[u]$ and the electric potential ϕ are built under the following separated form as

$$[u] = \sum_{i=1}^{N} g^i(\omega)\,[f^i(z)] \circ [v^i(x)]\,, \qquad \phi = \sum_{i=1}^{N} g^i_\phi(\omega)\, f^i_\phi(z)\, v^i_\phi(x) \tag{3.9}$$

where '$\circ$' denotes the Hadamard product. The unknown functions (g^i, g^i_ϕ) are defined in $[\omega_{min}, \omega_{max}]$, $([f^i], f^i_\phi)$ in Ω_z and $([v^i], v^i_\phi)$ in Ω_x. This separated representation is also used to express the virtual displacement δu and the virtual electric potential $\delta\phi$ used as test functions in Eq. 3.8

$$\begin{aligned} &[\delta u] = [\delta u_\omega] + [\delta u_f] + [\delta u_v] = \delta g\,[f] \circ [v] + g \cdot [v] \circ [\delta f] + g \cdot [f] \circ [\delta v], \\ &\delta\phi = \delta\phi_\omega + \delta\phi_f + \delta\phi_v = \delta g_\phi\, f_\phi\, v_\phi + g_\phi\, \delta f_\phi\, v_\phi + g_\phi\, f_\phi\, \delta v_\phi \end{aligned} \tag{3.10}$$

The resolution process is therefore an iterative procedure where the unknown functions must be computed for each enrichment step $i = 1,2,...,n,...,N$. The solution for iteration n can be expressed by

$$[u] = [\bar{u}] + g[V][f] = [\bar{u}] + g[F][v]\,, \qquad \phi = \bar{\phi} + g_\phi f_\phi v_\phi \tag{3.11}$$

where $([\bar{u}], \bar{\phi})$ are the displacement and potential solution obtained at iteration $(n-1)$

$$[\bar{u}] = \sum_{i=1}^{n-1} [u^i] = \sum_{i=1}^{n-1} g^i [F^i][v^i] = \sum_{i=1}^{n-1} g^i [V^i][f^i]\,, \qquad \bar{\phi} = \sum_{i=1}^{n-1} \phi^i = \sum_{i=1}^{n-1} g^i_\phi\, f^i_\phi\, v^i_\phi \tag{3.12}$$

and

$$[v^i] = \begin{bmatrix} v^i_1(x) \\ v^i_3(x) \end{bmatrix}, [V^i] = \begin{bmatrix} v^i_1(x) & 0 \\ 0 & v^i_3(x) \end{bmatrix}, [f^i] = \begin{bmatrix} f^i_1(z) \\ f^i_3(z) \end{bmatrix}, [F^i] = \begin{bmatrix} f^i_1(z) & 0 \\ 0 & f^i_3(z) \end{bmatrix} \tag{3.13}$$

Introducing this separated representation in the piezoelectric formulation expressed by Eq. 3.8, the problem is decomposed into three pair coupled equations given below

$$\begin{aligned} &\int_\omega \int_\Omega \Big([\varepsilon(\delta u_\omega)]^\top [C][\varepsilon(\bar{u} + g\,F\,v)] - [\varepsilon(\delta u_\omega)]^\top [e]^\top [E(\bar{\phi} + g_\phi\, f_\phi\, v_\phi)] \Big)\, \mathrm{d}V\, \mathrm{d}\omega \\ &\qquad - \int_\omega \int_\Omega \omega^2 \rho [\delta u_\omega]^\top [\bar{u} + g\,F\,v]\, \mathrm{d}V\, \mathrm{d}\omega = \int_\omega \int_{\partial_F \Omega} [\delta u_\omega]^\top [f_d]\, \mathrm{d}S\, \mathrm{d}\omega \end{aligned} \tag{3.14a}$$

$$\int_\omega \int_\Omega \Big([E(\delta\phi_\omega)]^\top [e][\varepsilon(\bar{u} + g\,F\,v)] + [E(\delta\phi_\omega)]^\top [\varepsilon][E(\bar{\phi} + g_\phi\, f_\phi\, v_\phi)] \Big)\, \mathrm{d}V\, \mathrm{d}\omega \;=\; 0 \tag{3.14b}$$

$$\begin{aligned} &\int_\omega \int_\Omega \Big([\varepsilon(\delta u_f)]^\top [C][\varepsilon(\bar{u} + g\,V\,f)] - [\varepsilon(\delta u_f)]^\top [e]^\top [E(\bar{\phi} + g_\phi\, f_\phi\, v_\phi)] \Big)\, \mathrm{d}V\, \mathrm{d}\omega \\ &\qquad - \int_\omega \int_\Omega \omega^2 \rho [\delta u_f]^\top [\bar{u} + g\,V\,f]\, \mathrm{d}V\, \mathrm{d}\omega = \int_\omega \int_{\partial_F \Omega} [\delta u_f]^\top [f_d]\, \mathrm{d}S\, \mathrm{d}\omega \end{aligned} \tag{3.15a}$$

$$\int_\omega \int_\Omega \left([E(\delta\phi_f)]^\top [e][\varepsilon(\bar{u}+gVf)] + [E(\delta\phi_f)]^\top [\varepsilon][E(\bar{\phi}+g_\phi f_\phi v_\phi)] \right) \mathrm{d}V\,\mathrm{d}\omega \quad = \quad 0 \tag{3.15b}$$

$$\int_\omega \int_\Omega \left([\varepsilon(\delta u_v)]^\top [C][\varepsilon(\bar{u}+gFv)] - [\varepsilon(\delta u_v)]^\top [e]^\top [E(\bar{\phi}+g_\phi f_\phi v_\phi)] \right) \mathrm{d}V\,\mathrm{d}\omega$$
$$- \int_\omega \int_\Omega \omega^2 \rho [\delta u_v]^\top [\bar{u}+gFv]\,\mathrm{d}V\,\mathrm{d}\omega = \int_\omega \int_{\partial_F\Omega} [\delta u_v]^\top [f_d]\,\mathrm{d}S\,\mathrm{d}\omega \tag{3.16a}$$

$$\int_\omega \int_\Omega \left([E(\delta\phi_v)]^\top [e][\varepsilon(\bar{u}+gFv)] + [E(\delta\phi_v)]^\top [\varepsilon][E(\bar{\phi}+g_\phi f_\phi v_\phi)] \right) \mathrm{d}V\,\mathrm{d}\omega \quad = \quad 0 \tag{3.16b}$$

These three pairs coupled equations define a non-linear problem. To solve it, an iterative procedure is followed. The fixed point loop is iterated m times until reaching a fixed solution for each enrichment step n which composes the final solution. This resolution strategy is explained in Algorithm 1.

Algorithm 1 Fixed point loop applied to the piezoelectric problem.

for $n = 1$ to N **do**
  Initialize $(g,g_\phi)^0$,$([f],f_\phi)^{(0)}$ and compute $([v],v_\phi)^{(0)}$ from Eq. 3.16
  for $m = 1$ to m_{max} **do**
    Step 1: knowing $([v],v_\phi)^{(m-1)}$,$([f],f_\phi)^{(m-1)}$, compute $(g,g_\phi)^{(m)}$ from Eq. 3.14
    Step 2: knowing $([v],v_\phi)^{(m-1)}$,$(g,g_\phi)^{(m)}$, compute $([f],f_\phi)^{(m)}$ from Eq. 3.15
    Step 3: knowing $([f],f_\phi)^{(m)}$,$(g,g_\phi)^{(m)}$, compute $([v],v_\phi)^{(m)}$ from Eq. 3.16
    Check for convergence (break)
  end for
  Set $g^n = g^{(m)}$,$[f^n] = [f]^{(m)}$,$[v^n] = [v]^{(m)}$ and $g^n_\phi = g^{(m)}_\phi$,$f^n_\phi = f^{(m)}_\phi$,$v^n_\phi = v^{(m)}_\phi$

  Set $[u^n] = [u^{n-1}] + g^n\,[V^n]\,[f^n]$ and $\phi^n = \phi^{n-1} + g^n_\phi f^n_\phi v^n_\phi$
end for

3.3.1 Step 1: Problem on load frequency domain

In order to simplify the notation, the functions $([f],f_\phi)^{(m-1)}$,$([v],v_\phi)^{(m-1)}$, which are assumed to be known, will be denoted as $\tilde{f},\tilde{f}_\phi,\tilde{v},\tilde{v}_\phi$ (and subsequently $\tilde{F},\tilde{V}$ in matrix form) and the functions $g^{(m)},g^{(m)}_\phi$ to be computed will be denoted as g,g_ϕ. The strain and electric fields are defined in matrix notation as

$$[\varepsilon(g\tilde{F}\tilde{v})] = g\,[\Sigma_z(\tilde{f})]\,[\tilde{\mathscr{O}}_v], \qquad [E(g_\phi\,\tilde{f}_\phi\,\tilde{v}_\phi)] = g_\phi\,[\Sigma^\phi_z(\tilde{f}_\phi)]\,[\tilde{\mathscr{O}}_{v_\phi}], \tag{3.17}$$

with

$$[\Sigma_z(\tilde{f})] = \begin{bmatrix} 0 & \tilde{f}_1 & 0 & 0 \\ 0 & 0 & \tilde{f}'_3 & 0 \\ \tilde{f}'_1 & 0 & 0 & \tilde{f}_3 \end{bmatrix}, \quad [\tilde{\mathscr{O}}_v] = \begin{bmatrix} \tilde{v}_1 \\ \tilde{v}'_1 \\ \tilde{v}_3 \\ \tilde{v}'_3 \end{bmatrix}, \quad [\Sigma^\phi_z(\tilde{f}_\phi)] = -\begin{bmatrix} 0 & \tilde{f}_\phi \\ \tilde{f}'_\phi & 0 \end{bmatrix}, \quad [\tilde{\mathscr{O}}_{v_\phi}] = \begin{bmatrix} \tilde{v}_\phi \\ \tilde{v}'_\phi \end{bmatrix} \tag{3.18}$$

where the prime ($'$) stands for the classical derivation. Introducing the above expression into Eq. 3.14, the variational problem defined on load frequency domain read

$$\int_\omega \delta g\, k_\omega^{vv}\, g\, \mathrm{d}\omega - \int_\omega \delta g\, k_\omega^{v\phi}\, g_\phi\, \mathrm{d}\omega - \int_\omega \delta g\, \omega^2 m_\omega\, g\, \mathrm{d}\omega = \int_\omega \delta g\, f_\omega\, \mathrm{d}\omega + \sum_{i=1}^{n-1} \left[\int_\omega \delta g\, \omega^2 \mu_\omega^i\, \bar{g}^i\, \mathrm{d}\omega - \int_\omega \delta g\, \sigma_\omega^{vv^i}\, \bar{g}^i\, \mathrm{d}\omega + \int_\omega \delta g\, \sigma_\omega^{v\phi^i}\, \bar{g}_\phi^i\, \mathrm{d}\omega \right] \tag{3.19a}$$

$$-\int_\omega \delta g_\phi\, k_\omega^{\phi v}\, g\, \mathrm{d}\omega - \int_\omega \delta g_\phi\, k_\omega^{\phi\phi}\, g_\phi\, \mathrm{d}\omega = \sum_{i=1}^{n-1} \left[\int_\omega \delta g_\phi\, \sigma_\omega^{\phi v^i}\, \bar{g}^i\, \mathrm{d}\omega + \int_\omega \delta g_\phi\, \sigma_\omega^{\phi\phi^i}\, \bar{g}_\phi^i\, \mathrm{d}\omega \right] \tag{3.19b}$$

where the functions with the superscript "i" are referred to the solution at the previous enrichment steps $i = 1,2,...,(n-1)$. The coefficients integrated in the spatial domain Ω are

$$\begin{aligned}
k_\omega^{vv} &= \int_\Omega [\tilde{\mathscr{E}}_v]^\top [\tilde{\Sigma}_z]^\top [C] [\tilde{\Sigma}_z] [\tilde{\mathscr{E}}_v]\, \mathrm{d}V, & k_\omega^{v\phi} &= \int_\Omega [\tilde{\mathscr{E}}_v]^\top [\tilde{\Sigma}_z]^\top [e]^\top [\tilde{\Sigma}_z^\phi] [\tilde{\mathscr{E}}_{v_\phi}]\, \mathrm{d}V, \\
k_\omega^{\phi v} &= \int_\Omega [\tilde{\mathscr{E}}_{v_\phi}]^\top [\tilde{\Sigma}_z^\phi]^\top [e] [\tilde{\Sigma}_z] [\tilde{\mathscr{E}}_v]\, \mathrm{d}V, & k_\omega^{\phi\phi} &= \int_\Omega [\tilde{\mathscr{E}}_{v_\phi}]^\top [\tilde{\Sigma}_z^\phi]^\top [\varepsilon] [\tilde{\Sigma}_z^\phi] [\tilde{\mathscr{E}}_{v_\phi}]\, \mathrm{d}V, \\
\sigma_\omega^{vv^i} &= \int_\Omega [\tilde{\mathscr{E}}_v]^\top [\tilde{\Sigma}_z]^\top [C] [\bar{\Sigma}_z^i] [\bar{\mathscr{E}}_v^i]\, \mathrm{d}V, & \sigma_\omega^{v\phi^i} &= \int_\Omega [\tilde{\mathscr{E}}_v]^\top [\tilde{\Sigma}_z]^\top [e]^\top [\bar{\Sigma}_z^{\phi^i}] [\bar{\mathscr{E}}_{v_\phi}^i]\, \mathrm{d}V, \\
\sigma_\omega^{\phi v^i} &= \int_\Omega [\tilde{\mathscr{E}}_{v_\phi}]^\top [\tilde{\Sigma}_z^\phi]^\top [e] [\bar{\Sigma}_z^i] [\bar{\mathscr{E}}_v^i]\, \mathrm{d}V, & \sigma_\omega^{\phi\phi^i} &= \int_\Omega [\tilde{\mathscr{E}}_{v_\phi}]^\top [\tilde{\Sigma}_z^\phi]^\top [\varepsilon] [\bar{\Sigma}_z^{\phi^i}] [\bar{\mathscr{E}}_{v_\phi}^i]\, \mathrm{d}V, \\
m_\omega &= \int_\Omega [\tilde{v}]^\top [\tilde{F}]^\top \rho\, [\tilde{F}] [\tilde{v}]\, \mathrm{d}V, & \mu_\omega^i &= \int_\Omega [\tilde{v}]^\top [\tilde{F}]^\top \rho\, [\bar{F}^i] [\bar{v}^i]\, \mathrm{d}V, \\
f_\omega &= \int_{\partial_F \Omega} [\tilde{v}]^\top [\tilde{F}]^\top [f_d]\, \mathrm{d}S
\end{aligned} \tag{3.20}$$

Note that for any particular value of the pulsation ω, it is easy to notice that the Eq. 3.19 results in

$$\left(k_\omega^{vv} - \omega^2 m_\omega\right) g - k_\omega^{v\phi} g_\phi = f_\omega + \sum_{i=1}^{n-1} [...] \tag{3.21a}$$

$$-k_\omega^{\phi v} g - k_\omega^{\phi\phi} g_\phi = \sum_{i=1}^{n-1} [...] \tag{3.21b}$$

These two equations can be combined in order to find an explicit expression for g such that

$$\left[k_\omega^{\phi\phi} \left(k_\omega^{vv} - \omega^2 m_\omega\right) + k_\omega^{\phi v} k_\omega^{v\phi}\right] g = f_\omega + \sum_{i=1}^{n-1} [...] \tag{3.22}$$

from which we can derive the value of the natural frequencies, ω_n, for which the resonance is detected

$$\omega_n^2 = \frac{k_\omega^{vv} + (k_\omega^{v\phi})^2 / k_\omega^{\phi\phi}}{m_\omega} \tag{3.23}$$

3.3.2 Step 2: Problem on Ω_z

At this step, the functions $(g, g_\phi)^{(m)}, ([v], v_\phi)^{(m-1)}$, assumed to be known, will be denoted as $\tilde{g}, \tilde{g}_\phi, \tilde{v}, \tilde{v}_\phi$ and the functions $([f], f_\phi)^{(m)}$ to be computed will be denoted as f, f_ϕ. The strain and electric field are defined in matrix notation as

$$[\varepsilon(\tilde{g}\tilde{V}f)] = \tilde{g}\,[\Sigma_x(\tilde{v})]\,[\mathscr{E}_f], \quad [E(\tilde{g}_\phi\,\tilde{v}_\phi\,f_\phi)] = \tilde{g}_\phi\,[\Sigma_x^\phi(\tilde{v}_\phi)]\,[\mathscr{E}_{f_\phi}] \tag{3.24}$$

with

$$[\Sigma_x(\tilde{v})] = \begin{bmatrix} \tilde{v}_1' & 0 & 0 & 0 \\ 0 & 0 & 0 & \tilde{v}_3 \\ 0 & \tilde{v}_1 & \tilde{v}_3' & 0 \end{bmatrix}, \quad [\mathscr{E}_f] = \begin{bmatrix} f_1 \\ f_1' \\ f_3 \\ f_3' \end{bmatrix}, \quad [\Sigma_x^\phi(\tilde{v}_\phi)] = \begin{bmatrix} -\tilde{v}_\phi' & 0 \\ 0 & -\tilde{v}_\phi \end{bmatrix}, \quad [\mathscr{E}_{f_\phi}] = \begin{bmatrix} f_\phi \\ f_\phi' \end{bmatrix} \tag{3.25}$$

Introducing the above expression into Eq. 3.15, the variational problem defined on Ω_z is

$$\begin{aligned} \gamma_\omega \int_{\Omega_z} [\delta\mathscr{E}_f]^\top [k_x^{ff}][\mathscr{E}_f]\,\mathrm{d}z - \theta_\omega \int_{\Omega_z} [\delta\mathscr{E}_f]^\top [k_x^{f\phi}][\mathscr{E}_{f_\phi}]\,\mathrm{d}z - \alpha_\omega \int_{\Omega_z} [\delta f]^\top [m_x][f]\,\mathrm{d}z = \\ \beta_\omega \int_{\partial_F\Omega_z} [\delta f]^\top [f_x]\,\mathrm{d}z + \sum_{i=1}^{n-1} \Bigg[\alpha_\omega^i \int_{\Omega_z} [\delta f]^\top [\mu_x^i][\bar{f}^i]\,\mathrm{d}z \\ - \gamma_\omega^i \int_{\Omega_z} [\delta\mathscr{E}_f]^\top [\sigma_x^{ff^i}][\bar{\mathscr{E}}_f^i]\,\mathrm{d}z + \theta_\omega^{g\phi^i} \int_{\Omega_z} [\delta\mathscr{E}_f]^\top [\sigma_x^{f\phi^i}][\bar{\mathscr{E}}_{f_\phi}^i]\,\mathrm{d}z \Bigg] \end{aligned} \tag{3.26a}$$

$$\begin{aligned} -\theta_\omega \int_{\Omega_z} [\delta\mathscr{E}_{f_\phi}]^\top [k_x^{\phi f}][\mathscr{E}_f]\,\mathrm{d}z - \eta_\omega \int_{\Omega_z} [\delta\mathscr{E}_{f_\phi}]^\top [k_x^{\phi\phi}][\mathscr{E}_{f_\phi}]\,\mathrm{d}z = \\ \sum_{i=1}^{n-1} \Bigg[\theta_\omega^{\phi g^i} \int_{\Omega_z} [\delta\mathscr{E}_{f_\phi}]^\top [\sigma_x^{\phi f^i}][\bar{\mathscr{E}}_f^i]\,\mathrm{d}z + \eta_\omega^i \int_{\Omega_z} [\delta\mathscr{E}_{f_\phi}]^\top [\sigma_x^{\phi\phi^i}][\bar{\mathscr{E}}_{f_\phi}^i]\,\mathrm{d}z \Bigg] \end{aligned} \tag{3.26b}$$

where the coefficients integrated in the Ω_x domain are

$$\begin{aligned} [k_x^{ff}] &= \int_{\Omega_x} [\tilde{\Sigma}_x]^\top [C][\tilde{\Sigma}_x]\,\mathrm{d}x, & [k_x^{f\phi}] &= \int_{\Omega_x} [\tilde{\Sigma}_x]^\top [e]^\top [\tilde{\Sigma}_x^\phi]\,\mathrm{d}x, \\ [k_x^{\phi f}] &= \int_{\Omega_x} [\tilde{\Sigma}_x^\phi]^\top [e][\tilde{\Sigma}_x]\,\mathrm{d}x, & [k_x^{\phi\phi}] &= \int_{\Omega_x} [\tilde{\Sigma}_x^\phi]^\top [\varepsilon][\tilde{\Sigma}_x^\phi]\,\mathrm{d}x, \\ [\sigma_x^{ff^i}] &= \int_{\Omega_x} [\tilde{\Sigma}_x]^\top [C][\bar{\Sigma}_x^i]\,\mathrm{d}x, & [\sigma_x^{f\phi^i}] &= \int_{\Omega_x} [\tilde{\Sigma}_x]^\top [e]^\top [\bar{\Sigma}_x^{\phi^i}]\,\mathrm{d}x, \\ [\sigma_x^{\phi f^i}] &= \int_{\Omega_x} [\tilde{\Sigma}_x^\phi]^\top [e][\bar{\Sigma}_x^i]\,\mathrm{d}x, & [\sigma_x^{\phi\phi^i}] &= \int_{\Omega_x} [\tilde{\Sigma}_x^\phi]^\top [\varepsilon][\bar{\Sigma}_x^{\phi^i}]\,\mathrm{d}x, \\ [m_x] &= \int_{\Omega_x} [\tilde{V}]^\top \rho\,[\tilde{V}]\,\mathrm{d}x, & [\mu_x^i] &= \int_{\Omega_x} [\tilde{V}]^\top \rho\,[\bar{V}^i]\,\mathrm{d}x, \\ [f_x] &= \int_{\partial_F\Omega_x} [\tilde{V}]^\top [f_d]\,\mathrm{d}x \end{aligned} \tag{3.27}$$

and the coefficients integrated in the load frequency domain are

$$\begin{aligned}
&\gamma_\omega = \int_\omega \tilde{g}^2 \,\mathrm{d}\omega, && \theta_\omega = \int_\omega \tilde{g}\tilde{g}_\phi \,\mathrm{d}\omega, && \eta_\omega = \int_\omega \tilde{g}_\phi^2 \,\mathrm{d}\omega, \\
&\gamma_\omega^i = \int_\omega \tilde{g}\,\bar{g}^i \,\mathrm{d}\omega, && \theta_\omega^{g\phi^i} = \int_\omega \tilde{g}\,\bar{g}_\phi^i \,\mathrm{d}\omega, && \theta_\omega^{\phi g^i} = \int_\omega \tilde{g}_\phi\,\bar{g}^i \,\mathrm{d}\omega, && \eta_\omega^i = \int_\omega \tilde{g}_\phi\,\bar{g}_\phi^i \,\mathrm{d}\omega, \\
&\alpha_\omega = \int_\omega \omega^2 \tilde{g}^2 \,\mathrm{d}\omega, && \alpha_\omega^i = \int_\omega \omega^2 \tilde{g}\,\bar{g}^i \,\mathrm{d}\omega, && \beta_\omega = \int_\omega \tilde{g} \,\mathrm{d}\omega
\end{aligned} \tag{3.28}$$

3.3.3 Step 3: Problem on Ω_x

At this step, the functions $(g, g_\phi)^{(m)}, ([f], f_\phi)^{(m)}$, which are assumed to be known, will be denoted as $\tilde{g}, \tilde{g}_\phi, \tilde{f}, \tilde{f}_\phi$ and the functions $([v], v_\phi)^{(m)}$ to be computed will be denoted as v, v_ϕ. The expression of the strain and electric field are

$$[\varepsilon(\tilde{g}\tilde{F}\,v)] = \tilde{g}\,[\Sigma_z(\tilde{f})]\,[\mathscr{E}_v], \quad [E(\tilde{g}_\phi\,\tilde{f}_\phi\,v_\phi)] = \tilde{g}_\phi\,[\Sigma_z^\phi(\tilde{f}_\phi)]\,[\mathscr{E}_{v_\phi}] \tag{3.29}$$

Introducing the above expression into Eq. 3.16, the variational problem defined on Ω_x read

$$\begin{aligned}
\gamma_\omega \int_{\Omega_x} [\delta\mathscr{E}_v]^\top [k_z^{vv}]\,[\mathscr{E}_v]\,\mathrm{d}x - \theta_\omega \int_{\Omega_x} [\delta\mathscr{E}_v]^\top [k_z^{v\phi}]\,[\mathscr{E}_{v_\phi}]\,\mathrm{d}x - \alpha_\omega \int_{\Omega_x} [\delta v]^\top [m_z]\,[v]\,\mathrm{d}x = \\
\beta_\omega \int_{\partial_F\Omega_x} [\delta v]^\top [f_z]\,\mathrm{d}x + \sum_{i=1}^{n-1} \Bigg[\alpha_\omega^i \int_{\Omega_x} [\delta v]^\top [\mu_z^i][\bar{v}^i]\,\mathrm{d}x \\
-\gamma_\omega^i \int_{\Omega_x} [\delta\mathscr{E}_v]^\top [\sigma_z^{vv^i}][\bar{\mathscr{E}}_v^i]\,\mathrm{d}x + \theta_\omega^{g\phi^i} \int_{\Omega_x} [\delta\mathscr{E}_v]^\top [\sigma_z^{v\phi^i}][\bar{\mathscr{E}}_{v_\phi}^i]\,\mathrm{d}x \Bigg]
\end{aligned} \tag{3.30a}$$

$$\begin{aligned}
-\theta_\omega \int_{\Omega_x} [\delta\mathscr{E}_{v_\phi}]^\top [k_z^{\phi v}]\,[\mathscr{E}_v]\,\mathrm{d}x - \eta_\omega \int_{\Omega_x} [\delta\mathscr{E}_{v_\phi}]^\top [k_z^{\phi\phi}]\,[\mathscr{E}_{v_\phi}]\,\mathrm{d}x = \\
\sum_{i=1}^{n-1} \Bigg[\theta_\omega^{\phi g^i} \int_{\Omega_x} [\delta\mathscr{E}_{v_\phi}]^\top [\sigma_z^{\phi v^i}][\bar{\mathscr{E}}_v^i]\,\mathrm{d}x + \eta_\omega^i \int_{\Omega_x} [\delta\mathscr{E}_{v_\phi}]^\top [\sigma_z^{\phi\phi^i}][\bar{\mathscr{E}}_{v_\phi}^i]\,\mathrm{d}x \Bigg]
\end{aligned} \tag{3.30b}$$

where the coefficients integrated in the Ω_z domain are

$$\begin{aligned}
&[k_z^{vv}] = \int_{\Omega_z} [\tilde{\Sigma}_z]^\top [C] [\tilde{\Sigma}_z]\,\mathrm{d}z, && [k_z^{v\phi}] = \int_{\Omega_z} [\tilde{\Sigma}_z]^\top [e]^\top [\tilde{\Sigma}_z^\phi]\,\mathrm{d}z, \\
&[k_z^{\phi v}] = \int_{\Omega_z} [\tilde{\Sigma}_z^\phi]^\top [e] [\tilde{\Sigma}_z]\,\mathrm{d}z, && [k_z^{\phi\phi}] = \int_{\Omega_z} [\tilde{\Sigma}_z^\phi]^\top [\varepsilon] [\tilde{\Sigma}_z^\phi]\,\mathrm{d}z, \\
&[\sigma_z^{vv^i}] = \int_{\Omega_z} [\tilde{\Sigma}_z]^\top [C] [\bar{\Sigma}_z^i]\,\mathrm{d}z, && [\sigma_z^{v\phi^i}] = \int_{\Omega_z} [\tilde{\Sigma}_z]^\top [e]^\top [\bar{\Sigma}_z^{\phi^i}]\,\mathrm{d}z, \\
&[\sigma_z^{\phi v^i}] = \int_{\Omega_z} [\tilde{\Sigma}_z^\phi]^\top [e] [\bar{\Sigma}_z^i]\,\mathrm{d}z, && [\sigma_z^{\phi\phi^i}] = \int_{\Omega_z} [\tilde{\Sigma}_z^\phi]^\top [\varepsilon] [\bar{\Sigma}_z^{\phi^i}]\,\mathrm{d}z, \\
&[m_z] = \int_{\Omega_z} [\tilde{F}]^\top \rho\,[\tilde{F}]\,\mathrm{d}z, && [\mu_z^i] = \int_{\Omega_z} [\tilde{F}]^\top \rho\,[\bar{F}^i]\,\mathrm{d}z, \\
&[f_z] = \int_{\partial_F\Omega_z} [\tilde{F}]^\top [f_d]\,\mathrm{d}z
\end{aligned} \tag{3.31}$$

and the ones integrated in the load frequency domain are expressed by Eq. 3.28.

3.4 Finite element discretization

To numerically compute the solution, a discrete representation of the unknown functions is addressed. For the load frequency domain, a uniform discretization of the interval $[\omega_{min}, \omega_{max}]$ is set up. The elementary vectors of DOFs associated with the mesh in ω are $[q_h^g]$,$[q_h^{g_\phi}]$. On the other hand, a classical FE approximation is used in domains Ω_x and Ω_z. The elementary vectors of DOFs associated with the mesh in Ω_x and Ω_z are $[q_e^v]$,$[q_e^{v_\phi}]$ and $[q_k^f]$,$[q_k^{f_\phi}]$ respectively. Under these assumptions, unknown functions and derived fields are approximated as follows

$$\begin{aligned}
&[v_e] = [N_x][q_e^v], && [\mathscr{E}_v^e] = [B_x][q_e^v], \quad [v_{\phi_e}] = [N_{\phi x}][q_e^{v_\phi}], && [E_{v_\phi}^e] = [B_{\phi x}][q_e^{v_\phi}] \\
&[f_k] = [N_z][q_k^f], && [\mathscr{E}_f^k] = [B_z][q_k^f], \quad [f_{\phi_k}] = [N_{\phi z}][q_k^{f_\phi}], && [E_{f_\phi}^k] = [B_{\phi z}][q_k^{f_\phi}] \\
&[g_h] = [N_\omega][q_h^g], && [g_{\phi_h}] = [N_{\phi\omega}][q_h^{g_\phi}]
\end{aligned} \tag{3.32}$$

where the matrices $[N_x]$,$[N_{\phi x}]$,$[B_x]$ and $[B_{\phi x}]$ contain the shape functions and their derivatives for the problem on Ω_x and analogously for the other domains. The total number of elements in $[\omega_{min}, \omega_{max}] = \bigcup_{h=1}^{n_\omega} \omega^h$, $\Omega_x = \bigcup_{e=1}^{n_x} \Omega_x^e$ and $\Omega_z = \bigcup_{k=1}^{n_z} \Omega_z^k$ domains are denoted as n_ω, n_x and n_z, respectively. Note that the interpolation can be different for each domain and also for the mechanical and electric unknowns separately. The introduction of the discretization in Eq. 3.30 lead to the electro-mechanical linear system on Ω_x domain

$$\left(\begin{bmatrix} [K_{vv}] & -[K_{vv_\phi}] \\ -[K_{vv_\phi}]^\top & -[K_{v_\phi v_\phi}] \end{bmatrix} - \begin{bmatrix} [M_v] & [\bar{0}] \\ [\bar{0}] & [\bar{0}] \end{bmatrix} \right) \begin{bmatrix} [q^v] \\ [q^{v_\phi}] \end{bmatrix} = \begin{bmatrix} [F_v] + [R_f] \\ [R_{v_\phi}] \end{bmatrix} \tag{3.33}$$

where

- $[q^v]$,$[q^{v_\phi}]$ are the vector of DOFs associated with the mesh in Ω_x for the mechanical and electric unknowns respectively.
- $[K_{vv}]$,$[K_{vv_\phi}]$,$[K_{v_\phi v_\phi}]$ are the stiffness, electro-mechanical and dielectric matrices obtained by assembling the elementary matrices $[K_{vv}^e]$,$[K_{vv_\phi}^e]$,$[K_{v_\phi v_\phi}^e]$, respectively

$$[K_{vv}^e(\tilde{g},\tilde{f})] = \left[\sum_{h=1}^{n_\omega} \gamma_\omega(\tilde{g}_h) \right] \int_{\Omega_x^e} [B_x]^\top \left[\sum_{k=1}^{n_z} [k_z^{vv}(\tilde{f}_k)] \right] [B_x] \, \mathrm{d}x \tag{3.34}$$

$$[K_{vv_\phi}^e(\tilde{g},\tilde{g}_\phi,\tilde{f},\tilde{f}_\phi)] = \left[\sum_{h=1}^{n_\omega} \theta_\omega(\tilde{g}_h,\tilde{g}_{\phi_h}) \right] \int_{\Omega_x^e} [B_x]^\top \left[\sum_{k=1}^{n_z} [k_z^{v\phi}(\tilde{f}_k,\tilde{f}_{\phi_k})] \right] [B_{\phi x}] \, \mathrm{d}x \tag{3.35}$$

$$[K_{v_\phi v_\phi}^e(\tilde{g}_\phi,\tilde{f}_\phi)] = \left[\sum_{h=1}^{n_\omega} \eta_\omega(\tilde{g}_{\phi_h}) \right] \int_{\Omega_x^e} [B_{\phi x}]^\top \left[\sum_{k=1}^{n_z} [k_z^{\phi\phi}(\tilde{f}_{\phi_k})] \right] [B_{\phi x}] \, \mathrm{d}x \tag{3.36}$$

- $[M_v]$ is the mass matrix obtained by assembling the elementary mass matrices $[M_v^e]$

$$[M_v^e(\tilde{g},\tilde{f})] = \left[\sum_{h=1}^{n_\omega} \alpha_\omega(\tilde{g}_h) \right] \int_{\Omega_x^e} [N_x]^\top \left[\sum_{k=1}^{n_z} [m_z(\tilde{f}_k)] \right] [N_x] \, \mathrm{d}x \tag{3.37}$$

- $[F_v]$ is the load vector obtained by assembling the elementary load vectors $[F_v^e]$

$$[F_v^e(\tilde{g},\tilde{f})] = \left[\sum_{h=1}^{n_\omega} \beta_\omega(\tilde{g}_h)\right] \int_{\partial_F \Omega_x^e} [N_x]^\top \left[\sum_{k=1}^{n_z} [f_z(\tilde{f}_k)]\right] \mathrm{d}x \tag{3.38}$$

- $[R_v]$,$[R_{v_\phi}]$ are the equilibrium residuals, obtained by assembling the elementary residual vectors $[R_v^e]$,$[R_{v_\phi}^e]$

$$\begin{aligned}[R_v^e(\tilde{g},\tilde{f},\bar{u},\bar{\phi})] = \sum_{i=1}^{n-1} \Bigg\{ & \left[\sum_{h=1}^{n_\omega} \alpha_\omega^i(\tilde{g}_h,\bar{g}_h^i)\right] \int_{\Omega_x^e} [N_x]^\top \left[\sum_{k=1}^{n_z} [\mu_z^i(\tilde{f}_k,\bar{f}_k^i)]\right] [\bar{v}^i] \,\mathrm{d}x \\ & - \left[\sum_{h=1}^{n_\omega} \gamma_\omega^i(\tilde{g}_h,\bar{g}_h^i)\right] \int_{\Omega_x^e} [B_x]^\top \left[\sum_{k=1}^{n_z} [\sigma_z^{v v^i}(\tilde{f}_k,\bar{f}_k^i)]\right] [\bar{\mathscr{E}}_v^i] \,\mathrm{d}x \\ & + \left[\sum_{h=1}^{n_\omega} \theta_\omega^{g\phi^i}(\tilde{g}_h,\bar{g}_{\phi_h}^i)\right] \int_{\Omega_x^e} [B_x]^\top \left[\sum_{k=1}^{n_z} [\sigma_z^{v\phi^i}(\tilde{f}_k,\bar{f}_{\phi_k}^i)]\right] [\bar{\mathscr{E}}_{v_\phi}^i] \,\mathrm{d}x \Bigg\} \end{aligned} \tag{3.39}$$

$$\begin{aligned}[R_{v_\phi}^e(\tilde{g}_\phi,\tilde{f}_\phi,\bar{u},\bar{\phi})] = \sum_{i=1}^{n-1} \Bigg\{ & \left[\sum_{h=1}^{n_\omega} \theta_\omega^{\phi g^i}(\tilde{g}_{\phi_h},\bar{g}_h^i)\right] \int_{\Omega_x^e} [B_{\phi x}]^\top \left[\sum_{k=1}^{n_z} [\sigma_z^{\phi v^i}(\tilde{f}_{\phi_k},\bar{f}_k^i)]\right] [\bar{\mathscr{E}}_v^i] \,\mathrm{d}x \\ & + \left[\sum_{h=1}^{n_\omega} \eta_\omega^i(\tilde{g}_{\phi_h},\bar{g}_{\phi_h}^i)\right] \int_{\Omega_x^e} [B_{\phi x}]^\top \left[\sum_{k=1}^{n_z} [\sigma_z^{\phi\phi^i}(\tilde{f}_{\phi_k},\bar{f}_{\phi_k}^i)]\right] [\bar{\mathscr{E}}_{v_\phi}^i] \,\mathrm{d}x \Bigg\} \end{aligned} \tag{3.40}$$

Analogously, the introduction of the discretization in the Eq. 3.26 and 3.19 lead to the next electro-mechanical linear systems on Ω_z and ω domains respectively

$$\left(\begin{bmatrix} [K_{ff}] & -[K_{ff_\phi}] \\ -[K_{ff_\phi}]^\top & -[K_{f_\phi f_\phi}] \end{bmatrix} - \begin{bmatrix} [M_f] & [\bar{0}] \\ [\bar{0}] & [\bar{0}] \end{bmatrix} \right) \begin{bmatrix} [q^f] \\ [q^{f_\phi}] \end{bmatrix} = \begin{bmatrix} [F_f]+[R_f] \\ [R_{f_\phi}] \end{bmatrix} \tag{3.41}$$

$$\left(\begin{bmatrix} [K_{gg}] & -[K_{gg_\phi}] \\ -[K_{gg_\phi}]^\top & -[K_{g_\phi g_\phi}] \end{bmatrix} - \begin{bmatrix} [M_g] & [\bar{0}] \\ [\bar{0}] & [\bar{0}] \end{bmatrix} \right) \begin{bmatrix} [q^g] \\ [q^{g_\phi}] \end{bmatrix} = \begin{bmatrix} [F_g]+[R_g] \\ [R_{g_\phi}] \end{bmatrix} \tag{3.42}$$

where the components have a similar formulation and interpretation to that already presented for the problem on Ω_x domain. The separated representation and reduction in the DOFs to which the PGD leads is depicted in the diagram of Figure 3.2. The classical FE approach implies n_ω resolutions of a 2D problem with $n_x \times n_z$ elements, obtaining a problem of $(n_\omega \times n_x \times n_z)$ size. On the contrary, the new strategy considering the PGD methodology involves N iterations of three 1D problems of n_ω, n_x and n_z elements, with a total problem size of $N \times (n_\omega + n_x + n_z)$.

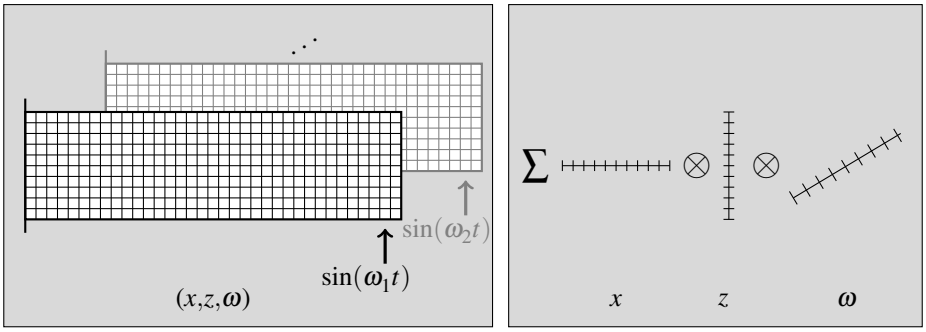

a) FE approach. b) PGD approach.

Figure 3.2 New PGD formulation versus classical 2D layerwise FE approach.

3.5 Numerical tests

This section is dedicated to the dynamic analysis of some piezoelectric composite beams in order to evaluate the proposed methodology. It should be mentioned that the PGD method has been successfully used to the harmonic analysis of composite beams [116] but also to solve static problems of piezoelectric plates [117]. This paper aims to extend the PGD formulation to the harmonic analysis of piezoelectric composite beams in the frequency domain. The FRFs are obtained for the first time by using the PGD method for the piezoelectric problem. In addition, the proposed formulation allows us to identify the modal parameters, natural frequencies and vibration modes, for both short circuit and open circuit conditions. In the following numerical test cases, the proposed approach will be evaluated by first addressing the eigenfrequencies and eigenmodes and subsequently the FRF.

In these tests, as far as the spatial discretization is concerned, a classical quadratic FE approximation is considered for both domains Ω_x and Ω_z. A Gaussian numerical integration with three points is used to evaluate the elementary matrices and also to compute the integrals in the load frequency domain. The results are compared with classical FE solutions and exact elastic solutions or models available in the literature. The FEA software ANSYS is also employed to provide reference solutions, considering a bi-dimensional approach using the PLANE223 element for piezoelectric layers. This element has eight nodes with up to five DOFs per node. For the non-piezoelectric layers, the higher order (quadratic) element PLANE183 is considered.

3.5.1 Convergence study of the proposed algorithm

The aim of the present section is to assess the performance of the proposed method to model coupling piezoelectric problems. In addition, a convergence study to evaluate the effect of the mesh size on spatial coordinates is addressed. For this purpose, a piezoelectric monomorph beam studied by Fernandes [118] is considered (see Figure 3.3a). The

monomorph beam is analysed assuming cylindrical bending (plane strain), for which the strains and the electric displacement in the y direction are considered to be negligible and therefore the columns and vectors in the 3D constitutive matrices associated to the negligible variables can be directly ignore. Different length to thickness ratios are tested for both close and open circuit electrical boundary conditions considering different spatial meshes. The monomorph is made of PZT-4 piezoelectric transversely isotropic ceramic. The characteristics of the test are described as follows:

- *Geometry*: $h = 1\,\text{mm}$ and three length to thickness ratios $S = L/h = 5, 10, 50$.
- *Material properties*:
  $\{C_{11}, C_{33}, C_{44}, C_{12}, C_{13}\} = \{139, 115, 25.6, 77.8, 74.3\}\,\text{GPa}$,
  $\{e_{15}, e_{31}, e_{33}\} = \{12.7, -5.2, 15.1\}\,\text{C/m}^2$,
  $\{\varepsilon_{11}, \varepsilon_{33}\} = \{13.06, 15.51\} \times 10^{-9}\,\text{F/m}$, $\rho = 7550\,\text{kg/m}^3$.
- *Boundary conditions*: the beam is simply supported at its ends: $u_3 = 0\ \forall z$ (through the whole thickness). Two sets of electric boundary conditions are considered:
  - Close circuit or short circuit condition (SC), with the potential forced to remain zero (grounded) at top and bottom surfaces of the monomorph beam.
  - Open circuit condition (OC), where the electric potential remains free everywhere.

In order to evaluate the convergence of the proposed methodology, a study with regard to the mesh size is carried out. The problem is evaluated by considering different meshes, with a number of n_z elements along the thickness. In the longitudinal domain, the size of the elements is the same as in the thickness direction for each analysis. The numerical values of the natural frequencies obtained with the PGD method by means of the Eq. 3.23 are compared with results computed with the commercial FEA software ANSYS using a very refined mesh obtained after a convergence study and the two-dimensional model solutions from [118].

Table 3.1 presents the analysis of the first three bending natural frequencies for the very thick to very thin beams for both open and close circuit conditions. The values of the natural frequencies computed with ANSYS are taken as reference to calculate the relative errors of the solution obtained with the proposed algorithm. It can be inferred that the convergence rate is rather high. In most cases it is only necessary to consider two numerical layers to obtain a value with a relative error below 1%. The PGD results show an excellent agreement with reference values, even closer to those obtained by the Fernandes 2D model which considers a larger mesh with no spatial separation.

Table 3.1 Convergence study for the first natural frequencies of the monomorph beam.

		SC frequency error (%)				OC frequency error (%)			
S	n_z	f_1	f_2	f_3	cum.	f_1	f_2	f_3	cum.
5	2	0.07	0.23	0.48	0.79	1.56	0.08	0.27	1.92
	4	0.03	0.07	0.10	0.20	0.21	0.06	0.03	0.30
	6	0.03	0.06	0.08	0.16	0.01	0.06	0.03	0.11
	8	0.03	0.05	0.07	0.16	0.01	0.06	0.05	0.13
	10	0.03	0.05	0.07	0.15	0.02	0.07	0.03	0.12
2D model [118]		0.48	1.07	1.23	2.77	0.28	0.76	1.10	2.15
ANSYS, Hz		**63910.9**	**219460**	**416755**	-	**64191.7**	**221862**	**422847**	-
10	2	0.02	0.06	0.13	0.21	0.01	0.04	0.10	0.15
	4	0.01	0.02	0.03	0.05	0.00	0.01	0.01	0.01
	6	0.01	0.01	0.03	0.05	0.05	0.01	0.01	0.07
	8	0.00	0.02	0.03	0.05	0.00	0.01	0.01	0.02
2D model [118]		0.12	0.37	0.64	1.13	0.08	0.27	0.51	0.87
ANSYS, Hz		**16797.2**	**63843.1**	**133694**	-	**16823.8**	**64185.4**	**134967**	-
50	1	0.01	0.03	0.07	0.11	0.01	0.03	0.07	0.11
	2	0.00	0.00	0.01	0.01	0.00	0.00	0.00	0.00
2D model [118]		0.01	0.03	0.05	0.09	0.01	0.02	0.04	0.08
ANSYS, Hz		**684.116**	**2730.13**	**6119.17**	-	**684.169**	**2730.95**	**6123.36**	-

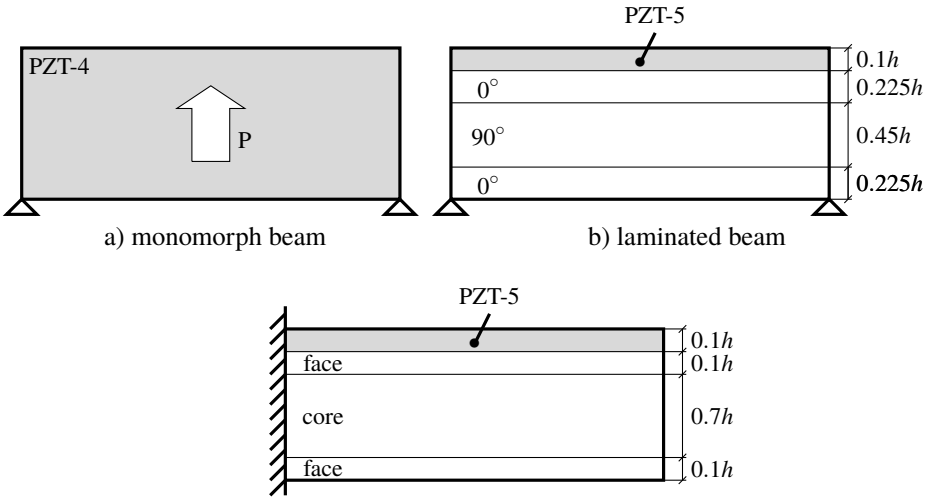

Figure 3.3 Beam tests configuration.

3.5.2 Laminated beam

In this section, a symmetric composite cross-ply beam with a piezoelectric layer bonded to its top analyzed in references [111, 119] is considered. The beam is depicted in Figure 3.3b. The aim of this analysis is to assess the performance of the proposed method to model piezoelectric laminated beams with different length to thickness ratios, for both open and close circuit conditions. The characteristics of the tests are described as follows:

- *Geometry*: lamination scheme $[pz/0°/90°/0°]$ with $0.1h/0.225h/0.45h/0.225h$ of relative thickness, where pz indicates the piezoelectric layer. Four length to thickness ratios from thick to very thin beams with $S = 5,10,20,100$.
- *Material properties*: The substrate of the beam is made of graphite-epoxy with the following properties,where subscripts L and T refer to the fiber and transverse direction respectively:

  $\{E_L, E_T, G_{LT}, G_{TT}\} = \{181, 10.3, 7.17, 2.87\}$ GPa,

  $\{\nu_{LT}, \nu_{TT}\} = \{0.28, 0.33\}, \rho = 1578\,\text{kg/m}^3$.

  The piezoelectric layer is made of PZT-5A transversely isotropic ceramic:

  $\{E_1, E_3, G_{23}\} = \{61.0, 53.2, 21.1\}$ GPa, $\{\nu_{12}, \nu_{13}\} = \{0.35, 0.38\}, \rho = 7600\,\text{kg/m}^3$,

  $\{d_{31}, d_{33}, d_{15}\} = \{-171, 374, 584\} \times 10^{-12}$ m/V,

  $\{\varepsilon_{11}, \varepsilon_{33}\} = \{1.53, 1.50\} \times 10^{-8}$ F/m.
- *Boundary conditions*: the beam is simply supported at its ends. Two sets of electric boundary conditions are considered for the inner surfaces:
  - Open circuit condition (OC), where the electric potential remains free, excepted on the inner surface of the piezoelectric layer where it is forced to be zero.
  - Close circuit or short circuit condition (SC), with the potential forced to remain zero (grounded) at the outer and inner surfaces of the piezoelectric layer.

The results of the natural frequencies are presented under a dimensionless value computed as $\overline{\omega} = \omega_n LS\sqrt{(\rho_0/Y_0)}$, with $\rho_0 = 1578\,\text{kg/m}^3$ and $Y_0 = 10.3\,\text{GPa}$ corresponding to the graphite-epoxy substrate. The vibration mode type is denoted as *bend*, *sh* and *t/c* for bending, shear and extensional modes, respectively. The numerical values obtained with the PGD method are compared with results computed with the Coupled Refined Layerwise Theory (CRLT) presented in [119], consisting of a coupled refined global-local FE model for which all the kinematic and stress continuity conditions are satisfied at the layer interfaces in the presence of non-zero in plane electric field component. Exact three-dimensional elasticity solution shown in [119], which has been derived from the study by Heyliger and Brooks in 1995 [120], is taken as a reference. Table 3.2 presents the values of the dimensionless natural frequencies for the thick to very thin beams, for the open circuit electrical condition. The first six bending frequencies as well as the extensional and shear modes are compared with the exact three-dimensional elasticity solution. These results show the excellent agreement with reference values for all types of modes. The maximum relative error is 0.6 %, although most of them are below 10^{-4} expressed in times one.

Table 3.2 OC dimensionless natural frequencies of laminated beam.

S	Mode type	Exact 3D	Present	Error (%)	CRLT [119]	CRLT error (%)
5	*bend*	5.534	5.535	0.0	5.659	2.3
	bend	13.625	13.609	0.1	13.973	2.6
	bend	22.058	21.929	0.6	22.698	2.9
	bend	30.709	30.712	0.0	32.096	4.5
	bend	39.392	39.311	0.2	42.291	7.4
	bend	47.990	48.122	0.3	53.263	11.0
	t/c	37.203	37.219	0.0	38.091	2.4
	sh	-	37.337	-	37.634	-
	sh	58.447	58.450	0.0	61.708	5.6
10	*bend*	7.443	7.470	0.4	7.525	1.1
	bend	22.137	22.138	0.0	22.637	2.3
	bend	38.128	38.129	0.0	39.108	2.6
	bend	54.502	54.481	0.0	55.896	2.6
	bend	71.214	71.225	0.0	73.072	2.6
	bend	88.232	88.237	0.0	90.807	2.9
	t/c	78.293	78.266	0.0	78.846	0.7
	sh	-	149.389	-	150.533	-
	sh	177.107	176.418	0.4	178.656	0.9
20	*bend*	8.370	8.372	0.0	8.400	0.4
	bend	29.770	29.770	0.0	30.103	1.1
	bend	57.829	57.802	0.0	58.874	1.8
	bend	88.550	88.551	0.0	90.553	2.3
	bend	120.290	120.181	0.1	123.292	2.5
	bend	152.514	152.569	0.0	156.456	2.6
	t/c	159.334	159.341	0.0	159.641	0.2
	sh	-	595.256	-	602.129	-
	sh	627.418	627.449	0.0	631.793	0.7
100	*bend*	8.754	8.755	0.0	8.755	0.0
	bend	34.812	34.802	0.0	34.834	0.1
	bend	77.578	77.579	0.0	77.688	0.1
	bend	136.121	136.094	0.0	136.459	0.2
	bend	209.246	209.247	0.0	210.048	0.4
	bend	295.585	295.693	0.0	297.194	0.5
	t/c	801.586	801.587	0.0	801.651	0.0
	sh	14965.634	15057.896	0.6	15083.435	0.8

The values of the dimensionless natural frequencies for the short circuit condition are shown in Table 3.3. The first six bending frequencies as well as the extensional and shear modes are compared with the exact 3D elasticity solution. The maximum relative error is also 0.6 %, but in general these errors are higher than those obtained for the open circuit condition. In any case, the results show a very good fit with respect to the reference values and mainly improve those obtained with the CRLT, especially for the thick case.

Table 3.3 SC dimensionless natural frequencies of laminated beam.

S	Mode type	Exact 3D	Present	Error (%)	CRLT [119]	CRLT error (%)
5	*bend*	5.517	5.536	0.3	5.643	2.3
	bend	13.589	13.599	0.1	13.943	2.6
	bend	22.002	21.914	0.4	22.645	2.9
	bend	30.635	30.712	0.3	32.010	4.5
	bend	39.307	39.311	0.0	42.164	7.3
	bend	47.901	48.023	0.3	53.095	10.8
	t/c	37.034	37.211	0.5	37.923	2.4
	sh	-	37.338	-	37.633	-
	sh	58.404	58.452	0.1	61.681	5.6
10	*bend*	7.412	7.443	0.4	7.496	1.1
	bend	22.066	22.138	0.3	22.572	2.3
	bend	38.020	38.129	0.3	39.015	2.6
	bend	54.355	54.480	0.2	55.772	2.6
	bend	71.027	71.225	0.3	72.908	2.6
	bend	88.006	87.992	0.0	90.593	2.9
	t/c	78.031	78.183	0.2	78.585	0.7
	sh	-	149.612	-	150.533	-
	sh	177.022	177.617	0.3	178.585	0.9
20	*bend*	8.331	8.372	0.5	8.361	0.4
	bend	29.648	29.771	0.4	29.982	1.1
	bend	57.620	57.802	0.3	58.676	1.8
	bend	88.264	88.551	0.3	90.290	2.3
	bend	119.930	120.181	0.2	122.973	2.5
	bend	152.080	152.778	0.5	156.083	2.6
	t/c	158.870	159.351	0.3	159.178	0.2
	sh	-	595.256	-	602.128	-
	sh	627.313	627.449	0.0	631.696	0.7
100	*bend*	8.711	8.754	0.5	8.712	0.0
	bend	34.640	34.784	0.4	34.664	0.1
	bend	77.202	77.579	0.5	77.313	0.1
	bend	135.474	136.114	0.5	135.813	0.2
	bend	208.269	209.252	0.5	209.074	0.4
	bend	294.235	295.598	0.5	295.849	0.5
	t/c	799.373	801.587	0.3	799.438	0.0
	sh	14965.520	14882.606	0.6	15083.327	0.8

Figure 3.4 represents the first ten vibration modes for the thick beam considering short circuit condition. The PGD algorithm is able to detect not only bending modes, but also extensional, shear and thickness modes with complex displacement distribution along either the beam axis or the thickness.

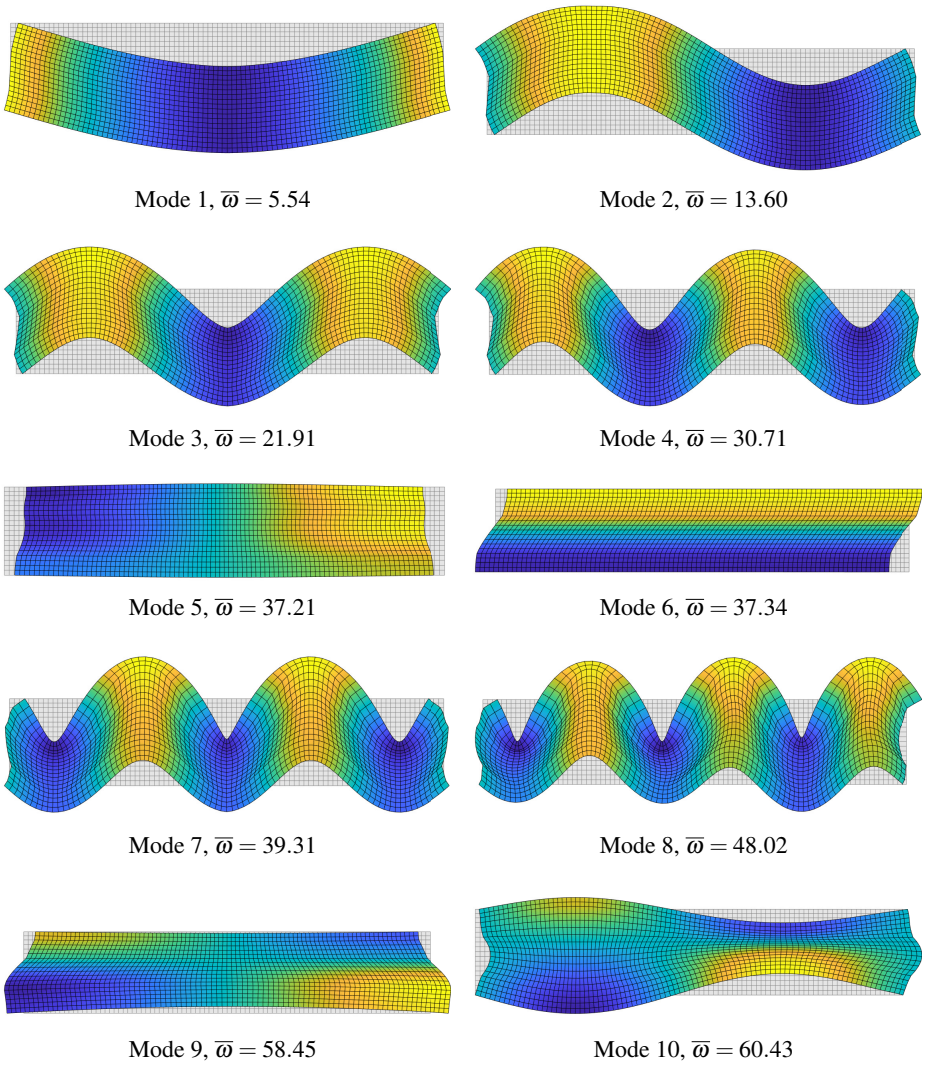

Figure 3.4 SC PGD solution for the laminated beam $(pz/0°/90°/0°)$ with $S = 5$.

3.5.3 Sandwich beam

To evaluate the PGD algorithm for solving coupled piezoelectric problems in beams with layers of very different properties, this test consists of a sandwich beam composed of two graphite-epoxy faces and a soft core with a PZT-5A layer bonded to its top as shown in Figure 3.3c. Additionally, the proposed formulation is validated to solve problems under different boundary conditions. This comprehensive test is also analysed in [111, 119]:

- *Geometry*: Thickness of the piezoelectric layer and face sheets are $0.1h$ while

thickness of the core is assumed to be $0.7h$. Three length to thickness ratios are analysed: $S = 5,10,20$.

- *Material properties*: The face sheets are made of graphite-epoxy with the following properties

  $\{E_L, E_T, G_{LT}, G_{TT}\} = \{131.1, 6.9, 3.588, 2.3322\}$ GPa,

  $\{\nu_{LT}, \nu_{TT}\} = \{0.32, 0.49\}$, $\rho = 1000\,\text{kg/m}^3$.

  The material properties of the soft core are:

  $\{E_1, E_2, E_3, G_{12}, G_{13}, G_{23}\} = \{0.2208, 0.2001, 2760, 16.56, 545.1, 455.4\}$ MPa,

  $\{\nu_{12}, \nu_{13}, \nu_{23}\} = \{0.99, 0.00003, 0.00003\}$, $\rho = 70\,\text{kg/m}^3$.

- *Boundary conditions*: Three different support cases are considered; simply support, cantilever and clamped, under open circuit electrical boundary conditions.

In Tables 3.4, 3.5 and 3.6, the natural frequencies are also presented under a dimensionless value computed as $\overline{\omega} = \omega_n LS\sqrt{(\rho_0/Y_0)}$, with $\rho_0 = 1000\,\text{kg/m}^3$ and $Y_0 = 6.9\,\text{GPa}$. The numerical values obtained with the PGD method are compared with results of the coupled refined theory in [119] and the results computed with the commercial FEA software ANSYS using a very refined mesh, except for the simply support case for which the exact 3D solution is also provided in the previous reference. It should be mentioned here that for the cantilever and the clamped beam tests it is required to build simutaneously 2-tuple in order to achieve accurate results as in [121]. Further information on this technique can be also found in [122, 123].

Table 3.4 OC dimensionless natural frequencies of simply support sandwich beam.

S	Mode type	Exact 3D	Present	Error (%)	CRLT [119]	CRLT error (%)
5	*bend*	3.974	3.974	0.01	4.258	7.1
	bend	8.962	8.963	0.01	9.153	2.1
	bend	14.344	14.353	0.07	13.291	7.3
10	*bend*	6.221	6.221	0.00	6.538	5.1
	bend	15.895	15.892	0.02	17.035	7.2
	bend	25.729	25.728	0.00	27.173	5.6
	bend	35.847	35.853	0.02	36.694	2.4
	bend	46.384	46.407	0.05	45.541	1.8
	bend	57.375	57.409	0.06	53.633	6.5
	sh	62.168	62.167	0.00	62.535	0.6
20	*bend*	7.866	7.877	0.14	8.026	2.0
	bend	24.883	24.880	0.01	26.154	5.1
	bend	44.087	44.084	0.01	47.082	6.8
	bend	63.581	63.574	0.01	68.148	7.2
	bend	83.159	83.155	0.00	88.739	6.7
	bend	102.916	102.918	0.00	108.747	5.7
	sh	131.774	131.776	0.00	132.315	0.4

Table 3.5 OC dimensionless natural frequencies of cantilever sandwich beam.

S	Mode type	ANSYS	Present	Error (%)	CRLT [119]	CRLT error (%)
5	*bend*	1.880	1.885	0.3	1.989	5.8
	bend	6.144	6.181	0.6	6.433	4.7
	bend	11.618	11.732	1.0	11.436	1.6
	t-c	15.400	15.416	0.1	-	-
	bend	17.448	17.666	1.2	14.847	14.9
10	*bend*	2.592	2.595	0.1	2.670	3.0
	bend	9.987	10.019	0.3	10.624	6.4
	bend	20.393	20.467	0.4	21.656	6.2
	bend	30.165	30.524	1.2	31.289	3.7
	t-c	33.327	33.401	0.2	-	-
	bend	41.120	41.665	1.3	41.404	0.7
	bend	51.841	52.277	0.8	50.064	3.4
20	*bend*	2.967	2.968	0.0	2.997	1.0
	bend	14.661	14.678	0.1	15.299	4.3
	bend	32.959	33.018	0.2	34.951	6.0
	bend	52.321	52.450	0.2	55.911	6.9
	t-c	67.506	67.551	0.1	-	-
	bend	72.436	72.354	0.1	77.303	6.7
	bend	92.277	92.315	0.0	98.001	6.2

Table 3.6 OC dimensionless natural frequencies of clamped sandwich beam.

S	Mode type	ANSYS	Present	Error (%)	CRLT [119]	CRLT error (%)
5	*bend*	4.849	4.858	0.2	5.152	6.3
	bend	9.995	10.087	0.9	10.055	0.7
	bend	15.700	15.748	0.3	14.332	8.6
10	*bend*	8.520	8.485	0.4	9.122	7.8
	bend	17.477	17.427	0.3	18.561	7.0
	bend	27.636	27.642	0.0	28.797	5.0
	bend	38.124	38.052	0.2	38.517	1.8
	bend	49.090	48.891	0.4	47.602	2.3
	bend	60.368	60.262	0.2	55.820	6.8
20	*bend*	13.534	13.452	0.6	14.181	5.6
	bend	29.351	29.215	0.5	31.228	7.1
	bend	47.751	47.550	0.4	50.990	7.5
	bend	67.019	66.753	0.4	71.473	7.3
	bend	86.793	86.452	0.4	91.982	6.6
	bend	106.895	106.617	0.3	112.103	5.5

Figure 3.5 is designed to show the potential of the new robust variational formulation to find the solution for a set of the load frequency within an interval $[\omega_{min}, \omega_{max}]$. In the graph, the FRF of the electromechanical problem is plotted. It shows the agreement between the amplitude of the displacements and the voltage response calculated both through a harmonic analysis in ANSYS and using the PGD formulation.

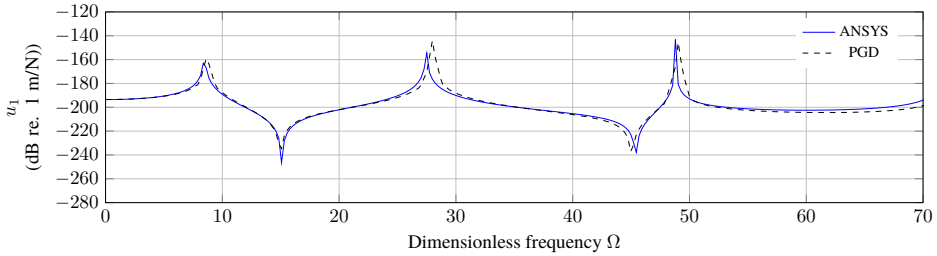

a) horizontal displacement

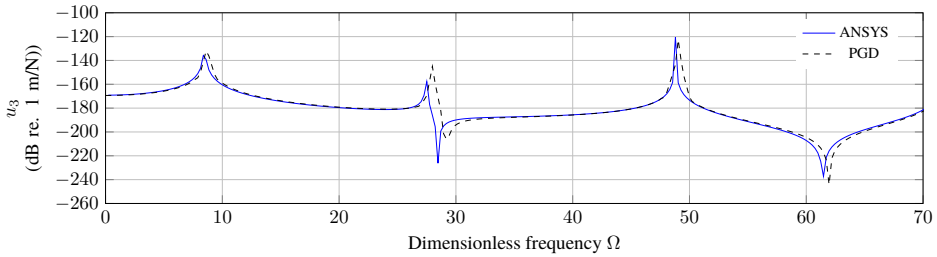

b) vertical displacement

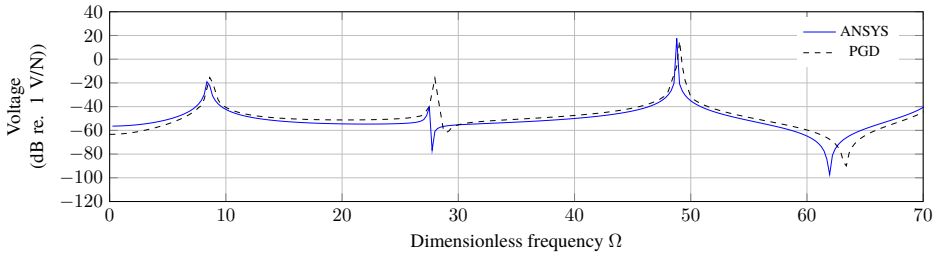

c) voltage

Figure 3.5 FRF at the top at $x = L/3$ for the clamped sandwich beam with $S = 10$.

The former semi-logarithmic representation allow us to detect the anti-resonance peaks. This particular feature can be used to evaluate the validity of the computed FRF using the PGD method. In particular, Figure 3.5 represents the FRF of vertical and horizontal displacements and voltage separately, for the clamped sandwich beam under a vertical harmonic point load placed at $x = L/2$. Only the response at the top at $x = L/3$ of the beam

with a slenderness ratio of $S = 10$ is represented. In this case, there are six bending modes in the frequency range under consideration, as it is remarked in Table 3.6. Nevertheless, only the symmetrical vibration bending modes (odd modes) can be distinguished in this graphical representation. This is due to the fact that the vibration nodes of the anti-symmetric bending modes (even modes) are located at the central line of the beam where the load is applied. As a general remark, the highest frequencies occur for the clamped beam and the lowest values are obtained for the cantilever beam (clamped/free case). The natural frequencies obtained with the PGD method are almost always lower than those of the couple refined layerwise model with continuous inter-laminar stresses (CRLT) and the differences with the reference values remain always low. The maximum relative error is 1.3 % and the average relative error does not exceed 0.3 % for the three cases of boundary conditions considered. This is especially remarkable for the simply supported beam, for which the result of the PGD model achieves a really high accuracy compared to the exact three-dimensional elastic solution. In this case, the average error obtained with the PGD methodology is 0.02% while that achieved by the CRLT model is almost 5%.

3.6 Conclusions

The main goal of this paper is to extend the PGD formulation to multi-field analysis in solid mechanics for the forced vibration problems. A new formulation based on the PGD method applied to bidimensional piezoelectric laminated beams is developed. A harmonic space-frequency description of the dynamic problem is first considered and a variable separation in the spatial domain is introduced. For both spatial coordinates x (beam axis coordinate) and z (thickness coordinate), a classical 3-node FE is used in the discretization. In addition, the load frequency is also introduced as a problem variable. The derived iterative methodology implies the computation of three 1D problems for each enrichment step used to represent the solution. The fixed-point method is employed to obtain the results for each of the N enrichment steps. The advantages of the proposed algorithm become relevant when the number of numerical layers increases and greater precision is required. In these cases the number of DOFs in the classical formulation of the problem grows exponentially and the separation of variables becomes a very useful tool to reduce the order and limit the computational cost. Here, the potential of the PGD formulation has been demonstrated by the accuracy of its results.

The proposed formulation has been validated through several numerical tests, including different composite and sandwich beam configurations with a great variety of slenderness ratios and boundary conditions. The current study show the potential of the approach to evaluate all kinds of mode shapes, including complex thickness modes with non-uniform displacement distribution along x and z axis. This is achieved by the LW approach. In addition, the method has been proved to be successful in detecting even small variations in natural frequencies derived from different electrical boundary conditions, such as short circuit and open circuit conditions. This opens up the possibility of confidently introducing electrical loads into the formulation, by adding an equivalent capacitance matrix to the dielectric matrix as in reference [124]. This would lead to the extension of the PGD approach to the parametric modelling of bimorph PEHDs.

4 A feasibility study on piezoelectric energy harvesting from the operational vibration of a highway bridge

Title:	A feasibility study on piezoelectric energy harvesting from the operational vibration of a highway bridge
Authors:	M Infantes, R Castro-Triguero, R R Sola-Guirado, D Bullejos, M I Friswell
Journal:	Advances in Structural Engineering
ISSN:	1369-4332
JCR:	Impact Factor = 2.438, Q3 (Civil Engineering 81 / 138)
Details:	First published online September 1, 2022
DOI:	10.1080/15376494.2019.1578015

4.1 Introduction

Energy harvesting from ambient vibration sources for use in powering low energy electronic devices has become the focus of numerous scientific studies over recent decades, from the earliest approaches [125] to the latest challenges consideration [126]. The use of energy harvesting devices is increasingly required, especially in targets where the use of batteries is either indispensable or desirable. The limited lifetime, high maintenance costs and the environmentally harmful recycling process of batteries justify this new paradigm. WSNs used in SHM systems represent one of the promising applications [13, 14]. Poulin et al. [127] conducted a comparative study of electromagnetic and piezoelectric energy harvesting mechanisms from low-frequency vibration systems to power portable devices. In this field, energy harvesting from a vibrating piezoelectric device was established as a leading methodology [128, 129]. Almost all of the published results that focus on the piezoelectric effect as the transduction method propose resonance-based devices, mainly cantilever beams. Many of the early references proposed methods to optimise the system

parameters in order to maximise the harvested energy [130–132]. The reader is referred to recent articles for comprehensive details and latest trends [133, 134]. Cai and Zhu [135] presented a review focusing on simultaneous vibration control and energy harvesting, a challenging topic in structural dynamics.

One of the key concerns in the design of a piezoelectric harvester is to ensure that it matches the ambient excitation from which it is intended to harvest energy. Ambient vibration is usually classified into two categories: i) narrow band excitations, ii) broadband excitations. The former are modelled deterministically while the latter are usually analysed as random processes. Vibration-based energy harvesting from deterministic excitations have been the focus of many research works over the last two decades [136]. One of the main references on this subject is the book by Erturk and Inman [19]. Although some reflections on the random nature of ambient excitation had appeared earlier [137], Lefeuvre et al. [138] were probably the first to consider random vibration in the energy harvesting framework. Most of the early studies on energy harvesting from random vibrations considered Gaussian broadband excitation of harvesters [139–141]. However, references dealing with non-stationary vibrations can also be found in the literature [142, 143], as well as proposals on how to analyse the results of the harvested power from random vibrations, usually performed using the mean and standard deviation of the output voltage. Adhikari et al. [144] proposed an alternative approach based on the statistics of the peak voltage to analyse energy harvesters under random excitation. Another particular application involving the energy harvesting from the vibration of suspension bridge cables was considered by Shen et al. [145]. The above authors address the modelling of a device with simultaneous vibration control and energy harvesting functions [146].

A particular case of random excitation for energy harvesting would be the vibration of a host structure. In this context, vibration energy harvesting from bridge vehicle interaction has received considerable attention [147, 148]. Many references consider the harvested energy from vibration in beams generated by single moving loads [76, 149, 150], multi-moving loads [151] or even more complex models for moving vehicles [152, 153]. Among the few experimental studies on energy harvesting from bridge vibration, worth mentioning are the works by Peigney and Siegert [154] and by Kaur et al. [155]. In the latter, the application of direct piezoelectric conversion to harvest energy from both ambient structural vibrations and wind flow are addressed. Cahill et al. [156] experimentally studied energy harvesting from train-induced vibration and its application in SHM. Romero et al. [157] used an approach based on modal decomposition for this problem. Demartino et al. [158] presented a feasibility study of energy harvesting from pedestrian-induced vibrations on footbridges.

The novelty of this work lies in the use of real measured traffic-induced vibration response of structures as excitation in the power generation estimation of a well-established piezoelectric energy harvester model. This is the main breakthrough as the optimal design and analysis of energy harvesters is usually performed considering broadband Gaussian white noise or even ideal harmonic excitations. This paper develops new approaches for the design and feasibility study of piezoelectric vibration energy harvesters based on the experimentally measured spectral density of bridge acceleration. Therefore, the excitation of the system is not assumed to be a broadband Gaussian white noise but a real vibration of a host structure. A new semi-analytic formulation of the expected power is proposed after

introducing the well-known Single Degree Of Freedom (SDOF) electromechanical model of the harvester. After this theoretical background, an experimental study of a bowstring highway bridge located in Córdoba (Spain) is presented. A complete study of the expected power for both operational and ambient vibration cases is addressed. These two situations correspond to the bridge open to regular traffic and the bridge closed to traffic, respectively. Finally, a parametric sensitivity study is carried out in order to optimise the mass of the harvester according to the base excitation due to the bridge acceleration.

4.2 Equivalent electro-mechanical model

A complete general description of the piezoelectric vibration-based energy harvesting system is shown in Figure 4.1. The harvesting from the bridge vibration is performed by the piezoelectric conversion mechanism, mathematically described by the material's constitutive equations. A power-management circuit is used to convert the AC voltage across the piezoelectric device to a usable DC voltage across a storage capacitor (or battery). The sensor node is represented by a DC load, hereafter referred to as R_L.

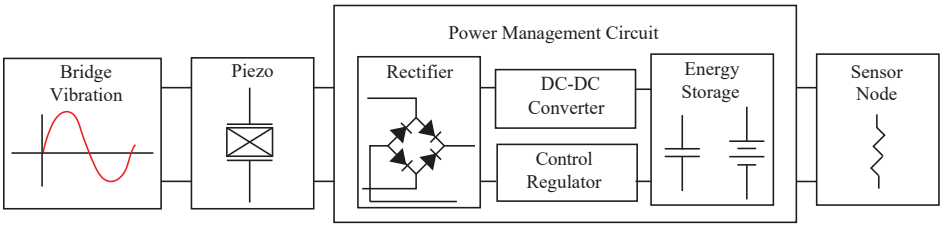

Figure 4.1 General electronic circuit for piezoelectric energy harvesting systems.

For a beam configuration of the PEHD with a proof mass at the tip end, a SDOF model is widely employed in the literature. This model is depicted in Figure 4.2, where x represents the tip displacement and x_b is the random base excitation.

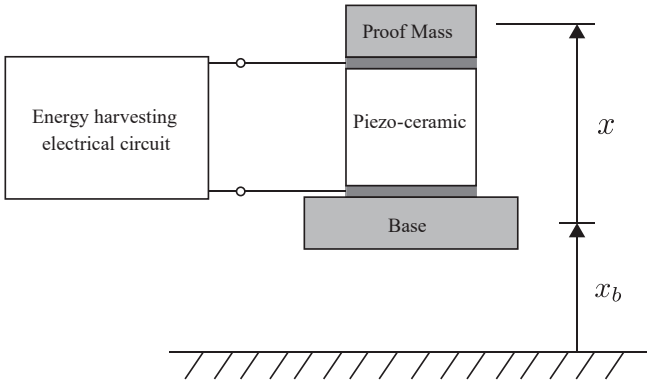

Figure 4.2 Schematic diagram of the piezoelectric energy harvester.

Although the model developed in this paper is for a piezoelectric harvester, Arroyo et al. [159] showed that both piezoelectric and electromagnetic harvesters give equivalent equations for a harvester active in a single mode. The choice of physical mechanism for a given application will depend on many issues, such as the power required, maximum additional mass, size limits, and the frequency spectrum of the excitation. However, the equivalence of the harvester models means that the conclusions reached in this paper for a piezoelectric harvester will also apply to an electromagnetic harvester.

4.2.1 PEHD time domain equations

The coupled electromechanical behaviour of the PEHD may be expressed by the linear ordinary differential equations

$$m\ddot{x}(t) + c\dot{x}(t) + kx(t) - \theta v(t) = f_b(t) \tag{4.1a}$$

$$i(t) = -\theta\dot{x}(t) - C_p\dot{v}(t) \tag{4.1b}$$

Eq. 4.1a is the Newton's equation of motion for a SDOF system, where m, c, k are the equivalent mass, damping and stiffness of the harvester. The mechanical force is modelled as proportional to the voltage across the piezoceramic, $v(t)$. Eq. 4.1b describes the electrical circuit, where the current $i(t)$ arises from the mechanical strain through the electromechanical coupling or force factor, θ, and the blocking capacitance of the piezoelectric insert, C_p. The reader is referred to the book by Erturk and Inman [19] for a comprehensive analysis of this and other equivalent electromechanical harvesters models. In this work the bridge vibration is used as the base excitation, and hence

$$f_b(t) = -m\ddot{x}_b(t) \tag{4.2}$$

According to Kirchhoff's current law for the case of a load resistance (R_L), the voltage is expressed as $v(t) = R_L\, i(t)$ and the electromechanical equations can be rewritten as

$$\ddot{x}(t) + \frac{c}{m}\dot{x}(t) + \frac{k}{m}x(t) - \frac{\theta}{m}v(t) = -\ddot{x}_b(t) \tag{4.3a}$$

$$\frac{\theta}{C_p}\dot{x}(t) + \dot{v}(t) + \frac{1}{C_p R_L}v(t) = 0 \tag{4.3b}$$

Note that, for an external electrical load close to short circuit conditions (very low external load impedance), the problem can be considered as very close to being electromechanically uncoupled (i.e., having negligible force factor θ) and the problem is greatly simplified. Some authors propose to approach the problem using correction factors to improve the predictions of the uncoupled system [150]. These two coupled equations can be expressed in the state-space form as

$$\frac{d\mathbf{z}_1(t)}{dt} = \mathbf{A}_1\,\mathbf{z}_1(t) + \mathbf{B}_1\,\ddot{x}_b(t) \tag{4.4}$$

where the state-vector and the corresponding coefficient matrices are, respectively

$$\mathbf{z}_1(t) = \begin{bmatrix} x(t) \\ \dot{x}(t) \\ v(t) \end{bmatrix} \tag{4.5}$$

$$\mathbf{A}_1 = \begin{bmatrix} 0 & 1 & 0 \\ -\dfrac{k}{m} & -\dfrac{c}{m} & \dfrac{\theta}{m} \\ 0 & -\dfrac{\theta}{C_p} & -\dfrac{1}{C_p R_L} \end{bmatrix}, \mathbf{B}_1 = \begin{bmatrix} 0 \\ -1 \\ 0 \end{bmatrix} \tag{4.6}$$

Eq. 4.4 can be solved with suitable initial conditions and the elements of the state-vector can be obtained. The aim of this paper is to analyse the problem when the forcing function is a random process; particularly the actual vibration of a highway bridge, both under normal operation and environmental excitation.

4.2.2 PEHD frequency domain equations

The response variables of the problem and the base excitation may also be considered in the frequency domain

$$x(t) = X(\omega)e^{i\omega t}, \quad v(t) = V(\omega)e^{i\omega t}, \quad f_b(t) = F_b(\omega)e^{i\omega t} \tag{4.7}$$

where $X(\omega)$, $V(\omega)$ and $F_b(\omega)$ are the Fourier transforms of $x(t)$, $v(t)$ and $f_b(t)$, respectively. Note that the base excitation $f_b(t)$ is usually measured experimentally in terms of acceleration (g units). For this reason, it is convenient to express the equations using time or frequency domain acceleration form

$$F_b(\omega) = -m\ddot{X}_b(\omega) \tag{4.8}$$

Defining the natural frequency of the harvester, $\omega_n = \sqrt{k/m}$, and the damping factor, $\zeta = c/2m\omega_n$, the coupled electromechanical problem defined by Eq. 4.3a and 4.3b can be expressed in the frequency domain as

$$\left(\omega_n^2 + 2i\omega\zeta\omega_n - \omega^2\right)X(\omega) - \frac{\theta}{m}V(\omega) = -\ddot{X}_b \tag{4.9a}$$

$$\frac{i\omega\theta}{C_p}X(\omega) + \left(i\omega + \frac{1}{C_p R_L}\right)V(\omega) = 0 \tag{4.9b}$$

The solution is

$$\begin{bmatrix} X(\omega) \\ V(\omega) \end{bmatrix} = \frac{1}{\Delta_1}\begin{bmatrix} i\omega + \dfrac{1}{C_p R_L} & \dfrac{\theta}{m} \\ \dfrac{-i\omega\theta}{C_p} & \omega_n^2 + 2i\omega\zeta\omega_n - \omega^2 \end{bmatrix}\begin{bmatrix} -\ddot{X}_b \\ 0 \end{bmatrix} \tag{4.10}$$

The determinant Δ_1 is defined as

$$\Delta_1 = -\alpha i\omega^3 - (2\alpha\zeta + 1)\omega_n\omega^2 + (\alpha + \kappa^2\alpha + 2\zeta)\omega_n^2 i\omega + \omega_n^3 \tag{4.11}$$

where the non-dimensional electromechanical coupling coefficient κ, and the time constant of the first-order electrical system are defined as

$$\kappa^2 = \frac{\theta^2}{kC_p} \quad \text{and} \quad \alpha = \omega_n C_p R_L \tag{4.12}$$

Hence, given an acceleration input of the bridge, $\ddot{x}_b(t)$, and transforming to the frequency domain $\ddot{X}_b(\omega)$, the harvester tip displacement, $X(\omega)$, and voltage output, $V(\omega)$, can be straightforwardly obtained in the frequency domain as

$$X(\omega) = -\frac{(i\omega\alpha + \omega_n)}{\Delta_1}\ddot{X}_b(\omega) \tag{4.13}$$

$$V(\omega) = \frac{i\omega\alpha\theta}{C_p\Delta_1}\ddot{X}_b(\omega) \tag{4.14}$$

The frequency response function $H(\omega)$ is defined as the transfer function evaluated along the frequency axis, and represents the relation between the output and input of a linear system. For the problem concerned, $H_{x\ddot{x}_b}(\omega)$ represents the frequency response function between the harvester tip displacement and the base excitation (in terms of acceleration), and, $H_{v\ddot{x}_b}(\omega)$ the frequency response function between the output voltage and the base excitation, which can be expressed as

$$H_{x\ddot{x}_b}(\omega) = \frac{X(\omega)}{\ddot{X}_b(\omega)} = -\frac{i\alpha\omega + \omega_n}{\Delta_1} \tag{4.15}$$

$$H_{v\ddot{x}_b}(\omega) = \frac{V(\omega)}{\ddot{X}_b(\omega)} = \frac{i\omega\alpha\theta}{C_p\Delta_1} \tag{4.16}$$

Hence, the relation between output voltage and harvester tip displacement in the frequency domain is given by the frequency response function $H_{vx}(\omega)$ and defined as

$$H_{vx}(\omega) = \frac{V(\omega)}{X(\omega)} \cdot \frac{\ddot{X}_b(\omega)}{\ddot{X}_b(\omega)} = \frac{H_{v\ddot{x}_b}(\omega)}{H_{x\ddot{x}_b}(\omega)} = \frac{-i\omega\alpha\theta}{C_p(i\alpha\omega + \omega_n)} \tag{4.17}$$

This expression may also be obtained directly from Eq. 4.9b.

4.3 Energy harvesting conversion for traffic-induced excitation

The total energy from the harvester due to base acceleration excitation can be estimated as

$$E = \int_0^\infty \frac{v^2(t)}{R_L}\,dt \tag{4.18}$$

where $v(t)$ is the voltage across the load resistor, R_L. Since the interest lies in the amount of energy consumed per unit time, the harvested power is considered, given by

$$P(t) = \frac{v^2(t)}{R_L} \tag{4.19}$$

Power is in general a non-Gaussian random process. To understand the efficiency and long-term reliability of an energy harvester, it is necessary to quantify statistically the harvester power. In this paper, the focus is particularly on the expected harvested power given by

$$E[P] = E\left[\frac{v^2(t)}{R_L}\right] = \frac{E[v^2(t)]}{R_L} \tag{4.20}$$

As seen in the previous section, for a linear energy harvesting system, the voltage output in the frequency domain can be expressed in the form

$$V(\omega) = H_{v\ddot{x}_b}(\omega)\,\ddot{X}_b(\omega) \tag{4.21}$$

It can be shown that the spectral density of the voltage, $S_V(\omega)$, is related to the spectral density of the base acceleration $S_{\ddot{X}_b}(\omega)$ by

$$S_V(\omega) = H_{v\ddot{x}_b} H^*_{v\ddot{x}_b} S_{\ddot{X}_b}(\omega) = \left|H_{v\ddot{x}_b}(\omega)\right|^2 S_{\ddot{X}_b}(\omega) \tag{4.22}$$

where $(^*)$ denotes the complex conjugate. Thus, in the steady-state (large t), it is obtained

$$\sigma_v^2 = E[v(t)^2] = \int_{-\infty}^{\infty} S_V(\omega)\,d\omega = \int_{-\infty}^{\infty} \left|H_{v\ddot{x}_b}(\omega)\right|^2 S_{\ddot{X}_b}(\omega)\,d\omega \tag{4.23}$$

For a base excitation represented by a Gaussian white noise, the expression for the expected power is [139]

$$E[P] = \frac{\pi\alpha\kappa^2 S_0}{(2\zeta\alpha^2+\alpha)\kappa^2 + 4\zeta^2\alpha + (2\alpha^2+2)\zeta} \tag{4.24}$$

since the forcing function has constant spectral density $S_{f_b}(\omega) = S_0$. The base acceleration, $\ddot{x}_b(t)$, cannot be assumed to be a Gaussian white noise, so that its spectral density $S_{\ddot{X}_b}(\omega)$ is not constant with respect to frequency. However, $\ddot{x}_b(t)$ can be measured from bridge vibrations with experimental tests under operational conditions. In order to have a proper frequency resolution, the experimental tests should be sampled with a high frequency (e.g. $f_s = 2^{11} = 2048\,\text{Hz}$). If Nyquist's theorem is considered, the integral in Eq. 4.23 can be approximated by

$$\sigma_v^2 \approx 2\int_0^{\pi f_s} \left|H_{v\ddot{x}_b}(\omega)\right|^2 S_{\ddot{X}_b}(\omega)\,d\omega = 2I_n \tag{4.25}$$

where $S_{\ddot{X}_b}(\omega)$ is known (i.e. experimentally measured) and is represented by a discrete scalar value for every sampled frequency. Using the expression of the frequency response function indicated by Eq. 4.16, the previous integral is now defined as

$$I_n = \int_0^{\pi f_s} \left|H_{v\ddot{x}_b}(\omega)\right|^2 S_{\ddot{X}_b}(\omega)d\omega = \left(\frac{\alpha\theta}{C_p}\right)^2 \int_0^{\pi f_s} \frac{\omega^2 S_{\ddot{X}_b}(\omega)}{\Delta_1(\omega)\Delta_1^*(\omega)}\,d\omega \tag{4.26}$$

The above integral cannot be solved analytically since $S_{\ddot{X}_b}(\omega)$ is a discrete random function evaluated from experimental tests on the bridge. The harvested power can be evaluated in a discrete form by using numerical integration (e.g. trapezoid rule) as

$$E[P] \approx \frac{2}{R_L}\left(\frac{\alpha\theta}{C_p}\right)^2 \sum_{j=0}^{[\pi f_s]} \frac{\omega_j^2}{\Delta_1(\omega_j)\Delta_1^*(\omega_j)} S_{\ddot{X}_b}(\omega_j)\Delta\omega \tag{4.27}$$

4.4 Experimental study on Palma del Río bridge

A panoramic view of the highway bridge used as the case study is shown in Figure 4.3. It is located in Palma del Río (Córdoba, Spain), over the Guadalquivir river. The bridge was opened to traffic in 2008. It is a bowstring arch, 130 m long simply supported span. It was designed as a steel-composite solution consisting of two inclined steel bowstring arches and a composite deck. The inclination of the arches is 68.8 degrees and it has a parabolic profile with a maximum rise of 25 m. The elements of the steel arches are manufactured with tubular sections 900×50 mm. The arches are tied by a Network pattern of cables of 45 mm of diameter, made of steel Y1860. The concrete slab is 16 m width and 0.25 m thickness, connected to the arches by steel traversal braces. These braces have a variable cross section defined by double T profiles, following a circular curve of 60 m of radius for the lower flanges, and a linear variation in the rest. They have a maximum web of 1.25 m in the center and they are located every 5 m. For further details the reader can consult the reference by García-Macías et al. [160].

4.4.1 Test setup

The bridge consists of two traffic lanes and two pedestrian sidewalks on each side of the deck. These sidewalks were used to place the accelerometers to measure the bridge vibrations without disrupting the traffic flow. Twelve measurements were taken on working days under two different situations: with open traffic (operational vibration) and with closed traffic with vehicles outside the bridge (ambient vibration). Figure 4.4 shows the points where the measurements were taken and some details of these measurements are given in Table 4.1.

Figure 4.3 A panoramic view of the Palma del Río bridge.

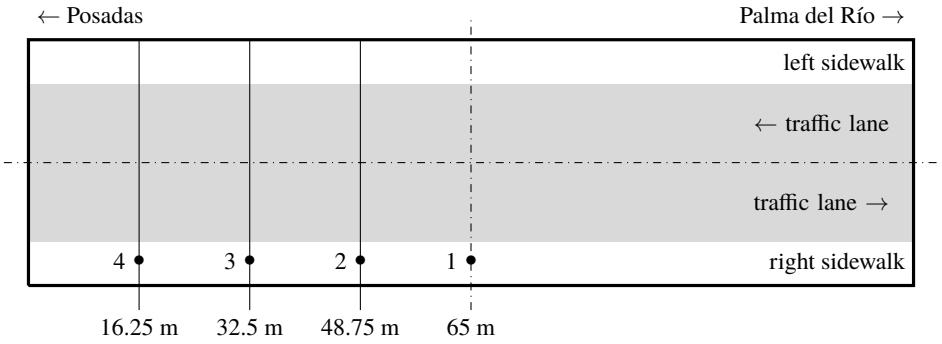

Figure 4.4 Acceleration measurement points on the bridge deck.

Table 4.1 Details of vibration measurements on the Palma del Río bridge.

	Date (2020)	Point	Record (min)	Traffic status	Temp. (°C)
setup 1	17 Jul.	1	5	open	21.5
setup 2	17 Jul.	1	5	close	22.5
setup 3	17 Jul.	1	5	open	23.6
setup 4	17 Jul.	1	5	open	30.2
setup 5	17 Jul.	1	5	open	32.4
setup 6	17 Jul.	2	5	open	33.5
setup 7	17 Jul.	3	5	open	34.2
setup 8	17 Jul.	4	5	open	35
setup 9	17 Jul.	4	5	close	36
setup 10	16 Oct.	1	30	open	11
setup 11	16 Oct.	1	5	close	13
setup 12	16 Oct.	1	30	open	15

A LMS SCADAS Mobile signal recorder was used to acquire the signal. The sensor used was a piezoelectric uniaxial accelerometer with very high sensitivity (10 V/g) from PCB Piezotronics, 393B31 model. The first four minutes of setups 10 and 11 are shown in Figures 4.5a and 4.5b respectively, to illustrate the measured data. In addition, Figure 4.5c shows the acceleration Acceleration Power Spectral Density (ASD) of setups 10 and 11. In setup 10 the traffic flow was continuous with both cars and other large vehicles, and a maximum acceleration of 7.25 m/s^2 was recorded. In contrast, with the bridge closed to traffic the acceleration level was reduced to a maximum of 1.55 m/s^2. Some other statistical data of the measurements are given in Table 4.2. For operational vibration measurements, the average Root Mean Square (RMS) value is around 0.34 m/s^2, with a standard deviation of 0.11 m/s^2, while for ambient vibration measurements the average drops to 0.04 m/s^2, with standard deviation 0.01 m/s^2. For both cases the coefficient of variation (CV) is around 30%.

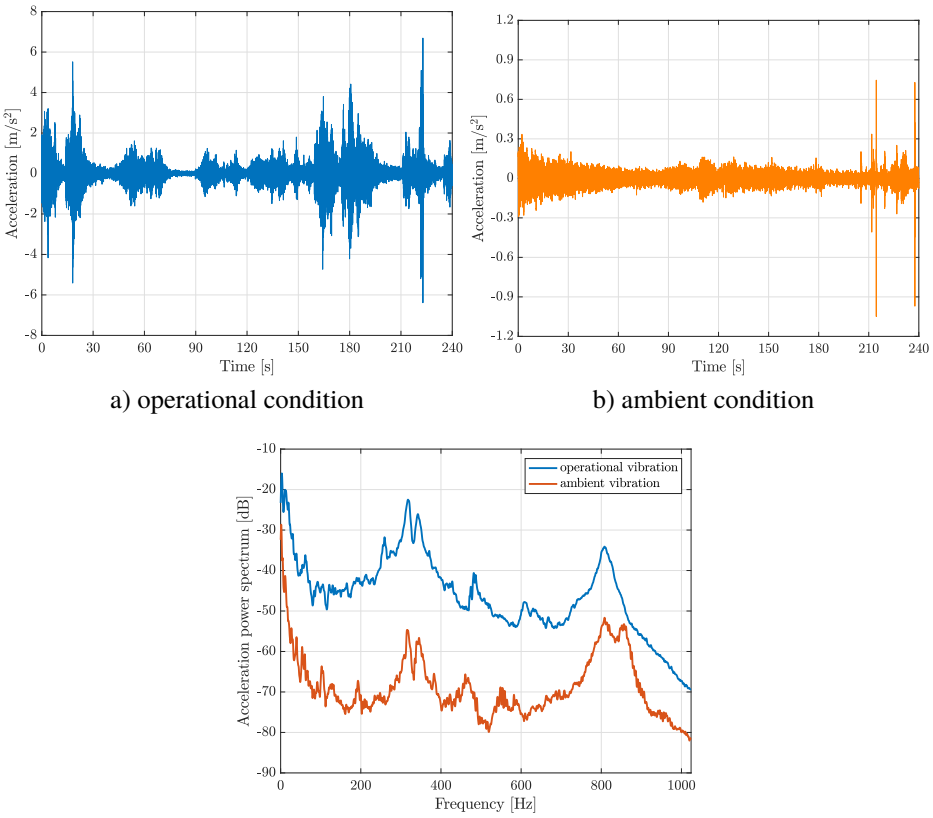

a) operational condition b) ambient condition

c) ASD

Figure 4.5 Vibration records of the Palma del Río bridge (setups 10 and 11).

Table 4.2 General statistics of vibration measurements on the Palma del Río bridge.

	Max.	Min.	Amplitude	RMS value
setup 1	2.4121	-2.4314	4.8435	0.1809
setup 2	0.1981	-0.1984	0.3965	0.0361
setup 3	2.6573	-3.0713	5.7286	0.1933
setup 4	3.1743	-3.1743	6.3487	0.3213
setup 5	3.6959	-3.5234	7.2193	0.3583
setup 6	6.1278	-6.2508	12.3786	0.3865
setup 7	6.9412	-5.7739	12.7151	0.2854
setup 8	8.8632	-8.9458	17.8090	0.5153
setup 9	0.1315	-0.1450	0.2766	0.0264
setup 10	6.9344	-7.2492	14.1836	0.4142
setup 11	1.5501	-1.3878	2.9379	0.0470
setup 12	5.9749	-7.2448	13.2197	0.3958

Note: values are given in m/s^2.

4.4.2 Energy harvesting conversion for traffic-induced excitation

The aim of this paper is to developed a feasibility study on piezoelectric energy harvesting from the operational vibration of real structures. For this purpose, a cantilever piezoelectric harvester subject to a forcing function represented by the real vibration measured at the Palma del Río bridge is evaluated. For this study, a SDOF piezoelectric harvester with the parameters indicated in Table 4.3 is considered. This model has previously been used in other similar studies in the literature [144, 161]. The frequency response function between the base excitation and the output voltage of the device is given in Figure 4.6.

Table 4.3 Parameters of the SDOF piezoelectric harvester for the case study.

Parameter	Value	Unit
m	9.12×10^{-3}	kg
c	0.218	N s/m
k	4.1×10^{3}	N/m
θ	-4.57×10^{-3}	N/V
C_p	43×10^{-9}	F
ω_n	670.49	rad
f_n	106.71	Hz
$R_{opt,th}$	34.685	kΩ
ζ	0.0178	-
κ^2	0.1185	-
α	1.0000	-

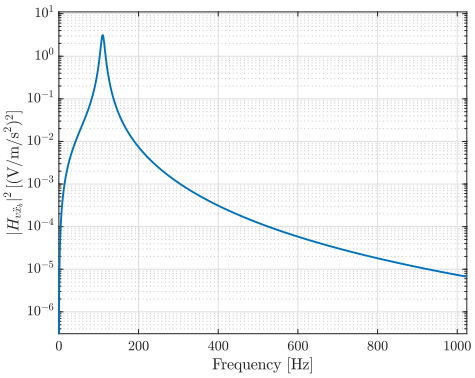

Figure 4.6 FRF between output voltage and base excitation for the SDOF harvester.

First, the coupling effect on energy harvesting is analysed. Figure 4.7 represents a short sample of the voltage signals from operational vibrations, where the differences between the output computed using the coupled and uncoupled system of equations are manifest. For general comparative purposes only, the mean power obtained with both coupled and uncoupled systems is compared below. The expression used to evaluate the mean power is $\bar{P} = (|v(t)|^2/N)/R_{opt,th}$, with N the number of samples of the discrete voltage signal $v(t)$ obtained with both the coupled and uncoupled approaches. Under operational vibrations represented by the 30-minute record of the setup 10, the computed mean power is 23.56 nW considering the coupled electromechanical system and 68.44 nW for the uncoupled equations. This represents an unrealistic increase in the harvested power of more than 290.5%. Under ambient vibrations represented by the 5-minute measurement of the setup 11, the mean power from coupled equations is 0.11 nW while the uncoupled equations give a value of 0.40 nW. This means an overestimation of around 363.6%.

In the light of these results, some conclusions can be drawn about the piezoelectric coupling effect. The coupling causes the voltage from the PZT to generate a force that opposes the harvester motion, which reduces the harvester response and hence the power harvested. It can be stated that although the uncoupled equations are numerically efficient because of their lower computational cost, they do not represent a good approximation of the energy harvesting mechanism. Hence these results confirm that the fully coupled equations should always be used, as highlighted by Erturk and Inman [162].

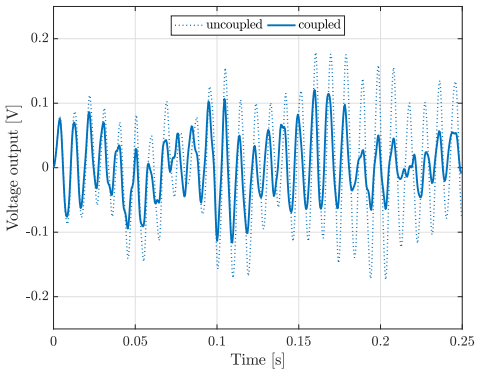

Figure 4.7 Coupled/uncoupled output voltage from the operational record (setup 10).

Figures 4.8a and 4.8b represent the first four minutes of the output voltage of the harvester subjected to operational and ambient real vibration of the Palma del Río bridge. Consistently with the vibration level recorded in each of the two differentiated situations (with the bridge open and closed to traffic) the voltage output from operational vibration is about ten times larger. Figure 4.8c shows the Power Spectral Density (PSD) of the output voltage for measurements 10 and 11. These functions have a similar trend to that of the ASD (Figure 4.5c), but additionally they present a peak around 100 Hz related to the natural frequency of the harvester.

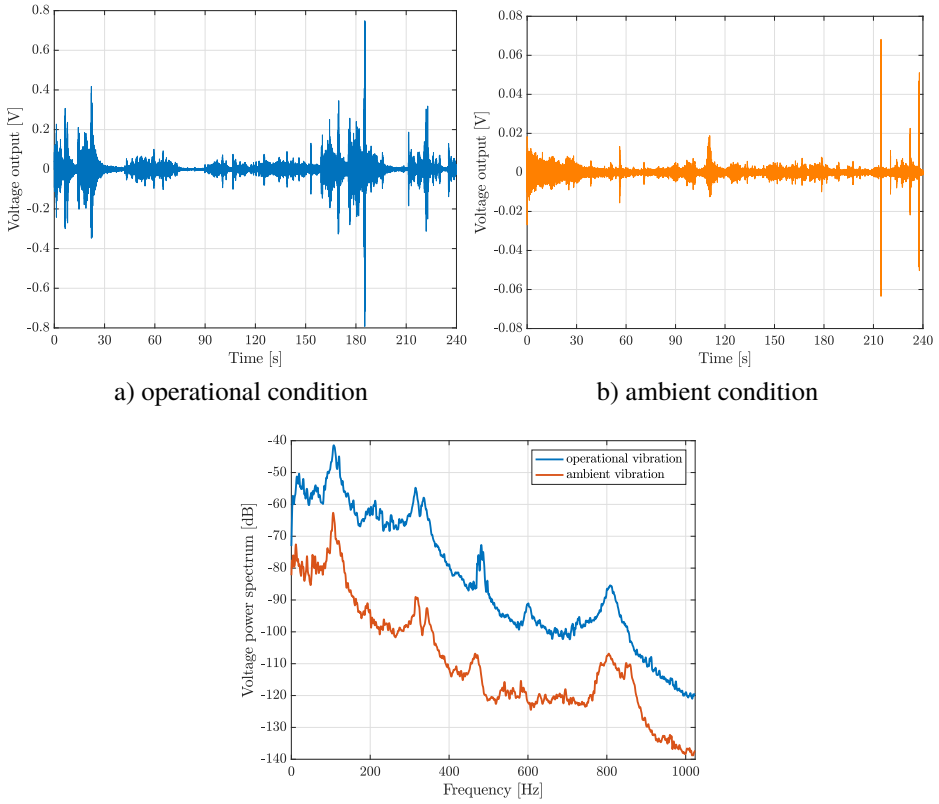

a) operational condition

b) ambient condition

c) output voltage PSD

Figure 4.8 Output voltage from the vibration records (setups 10 and 11).

The new semi-analytic approach of the expected power developed in the previous section is applied to evaluate the the available power from the real vibration measurement of the highway bridge. The maximum expected power has been calculated using Eq. 4.27 for different values of the load resistance R_L. The values obtained for both the operational and ambient vibration situations have been analysed and plotted in Figure 4.9. The expected power computed from the vibration for the bridge open to regular traffic is of the order of tens of nanowatts of magnitude. The maximum expected power obtained is $E[P] = 23.87\,\text{nW}$ for a load resistance of $R_{L,opt} = 28.8\,\text{k}\Omega$. In the case of ambient vibration, the energy harvested is two orders of magnitude smaller ($\times 10^{-1}\,\text{nW}$) and the maximum expected power is $E[P] = 0.116\,\text{nW}$ for a load resistance of $R_{L,opt} = 22.1\,\text{k}\Omega$. It is worth noting that the optimum load resistances obtained from this experimental analysis for the cases of operational and ambient vibrations differ by 20 to 40% respectively from the theoretical value represented by $R_{opt,th} = 1/(C_p \cdot \omega_n) = 34.7\,\text{k}\Omega$. However, it should be noted that this theoretical optimum assumes a purely resistive load and a single frequency resonant harvester response. The reported expected power values are considered

representative because they have been obtained with a semi-analytical approach using the spectral values of real long-term acceleration measurements (up to 30 minutes in the case of operational vibration).

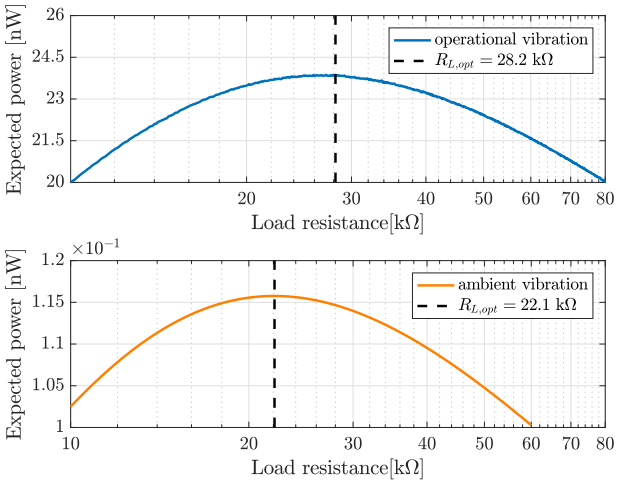

Figure 4.9 Power versus load resistance from the vibration records (setups 10 and 11).

4.5 Sensitivity analysis

Lefeuvre et al. [138] have already pointed out that the effective transmission of surrounding vibrations to the piezoelectric material depends on matching the resonance frequency of the harvester and the environmental frequencies. In this section, a sensitivity study on the effect of the harvester parameters on the expected power is described using the semi-analytic approach developed. This analysis represents an impedance optimisation strategy that has already been addressed by other authors in the literature. For instance, the study presented by Liao and Liang [163] considered different coupling effects or the analysis by Cai and Zhu [164] focussed on electromagnetic energy harvesters. The natural undamped frequency of the harvester is defined by only two parameters: the mass m and the stiffness k. Hence, if the stiffness k is fixed, the proof mass m could be optimized.

Figure 4.10 shows, for a set of reasonable mass values m of the piezo harvester, the values of the maximum expected power for different values of load resistance R_L. In this analysis, k is kept constant (with the value indicated in Table 4.3), m varies between [1-500] g and R_L is considered within a range of [1-100] kΩ for each mass value. The most remarkable consequence of increasing the mass value is that the expected power increases by an order of magnitude. A mass of about 250 g would provide more than a hundred μW of power. For this particular case, the expected power curve shows a maximum at around $m = 300$ g of mass for most values of R_L. A similar value of expected power would not be obtained until the mass is increased by 50%. This behaviour is, as expected, determined by the nature of the excitation.

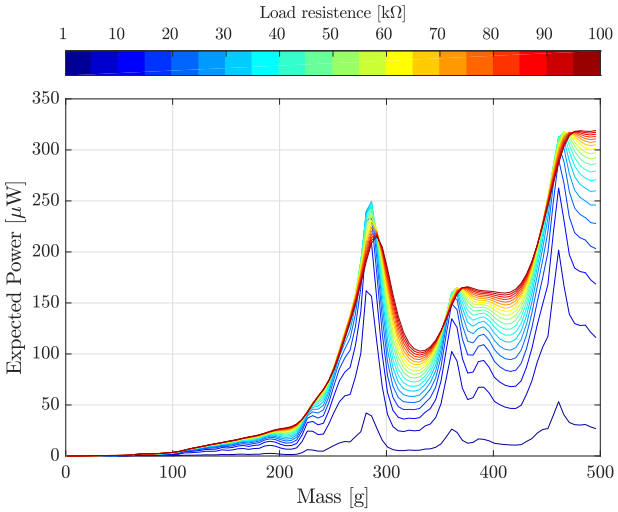

Figure 4.10 Effect of the harvester mass on the expected power (setup 12).

Figure 4.11 shows a clear correlation between the expected power curve and the spectral density of the acceleration recorded on the Palma del Río bridge for regular traffic situation. In particular the optimised mass ensures the harvester resonance occurs at a frequency where the bridge response is high.

4.6 Conclusions

The main goal of this paper is to study the feasibility of deploying a piezoelectric energy harvesting system on a real highway bridge. The novelty lies in the use of real measured traffic-induced vibration response as excitation in the power generation estimation. A new semi-analytic formulation based on real bridge vibration measurements is developed. Therefore, broadband white Gaussian noise excitation is no longer considered. The computation of the expected power is based on the closed-form transfer function between base excitation and harvester output voltage and on the experimentally measured spectral density of the bridge acceleration. The new approach has been used to evaluate the available power from real vibration of a bowstring highway bridge located in Palma del Río, Córdoba (Spain). Two different situations have been considered in the assessment of the harvested power: i) operational vibration records with the bridge open to regular traffic, ii) ambient vibrations with the bridge closed to traffic. The numerical results show that the energy harvested from ambient vibration is two orders of magnitude smaller than that obtained from operational vibration. Consequently, it could be stated that the level of traffic could condition the viability of a piezoelectric energy harvesting system. In addition, a parametric sensitivity study has been used to optimise the harvester mass according to the excitation and considerably increase the expected power (from nW to μW).

This feasibility study is one of the first to present expected power values calculated from the operational vibration of a real structure. This new approach enables a more realistic

study of the application of energy harvesting technique to the power requirements of WSNs and other low-power electronic devices used in SHM. The results show the potential of the semi-analytic approach to evaluate the expected power of piezoelectric energy harvesters subjected to a highway bridge excitation. This also opens up the possibility to confidently extend the approach to different base excitation mechanisms, such as the vibrations of railway bridges or footbridges.

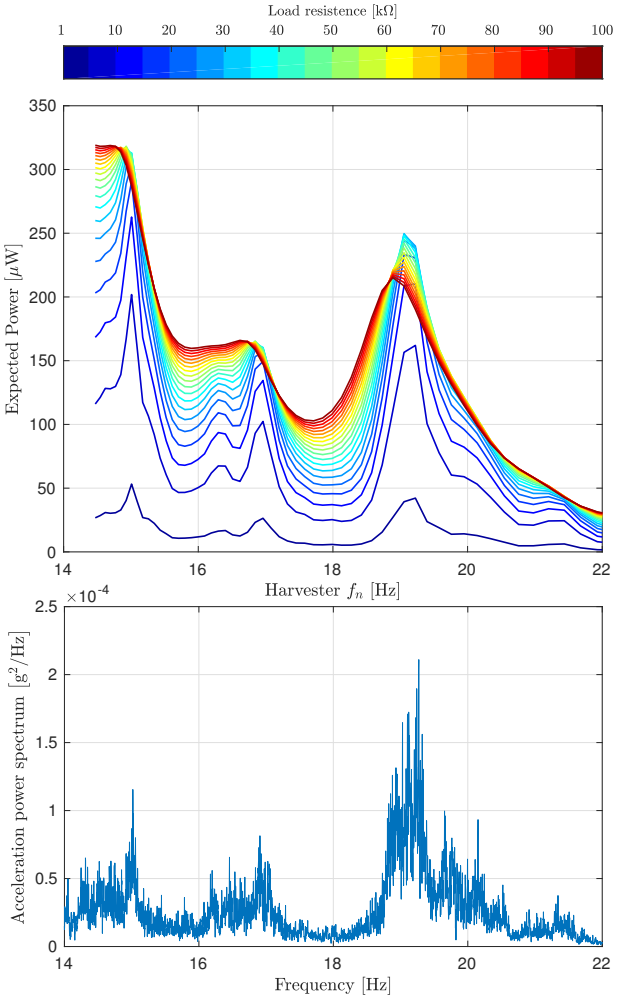

Figure 4.11 Expected power for different harvester natural frequencies versus the acceleration power spectrum (setup 12).

5 General conclusions and future developments

Y ya está todo listo para la siguiente foto:
la familia, los de siempre, mis queridísimos locos,
en resumen todas y todos los que hicisteis que valiera la pena
saltar a esta piscina sin saber si estaba llena.
Mikel Izal, 2021

The core idea of the research plan developed by this thesis work is the long-term SHM through the use of self-supplied sensors. The energy requirement of the monitoring system has typically been solved by the installation of grid-connected sensors, which is a solution with a fixed additional economic and environmental cost that is difficult to maintain in the long term. In addition, the remote location of many of the structures makes mains power supply unfeasible. The novelty of this proposal is the self-supply of the sensors applying a totally clean energy collection system that uses the vibrations of the structures to generate energy. This vibration-based energy harvesting system makes use of devices in which the piezoelectric energy conversion mechanism takes place.

The performance of a PEHD is strongly dependent on the excitation source, represented by the vibration of the host structure. Numerous variants of these devices have been proposed and studied in the literature. Among these proposals, the most widely studied and tested consists of a small cantilever beam. Compared to other designs, it has lower resonance frequency and a relatively larger deformation for a given input excitation. They usually consist of one or two layers of piezoelectric material (unimorph and bimorph configurations) and optionally a mass is attached to the free end to move the resonance frequency towards some desired point (tuning) and/or amplify the conversion effect. These devices would be embedded in the host structure which, when vibrating, would induce a dynamic voltage in the layers of piezoelectric material, resulting in an alternating voltage output through electrodes placed on these layers. To use this energy to charge a battery, it would be necessary to include an electronic circuit for rectification and conversion to direct current. In the analysis of such devices, it is common practice to consider a resistance or impedance to represent the electrical charge.

The study of the vibration-based energy harvesting has been approached in this thesis with a twofold focus. On the one hand, the first two articles that make up this research work focus on the numerical modelling and analysis of composite beams such as those that constitute PEHDs. On the other hand, the third article of the compendium has a more practical focus. It studies the feasibility of a piezoelectric vibration-based energy harvesting system for a real highway bridge. The findings of each of these studies are presented in detail in the chapters of the individual articles. However,the main developments and conclusions are outlined below.

5.1 Conclusions

Overall, the main contributions of this thesis include:

- The development of a new methodology based on the PGD method to solve the forced vibration problem in bi-dimensional laminated beams. A harmonic space-frequency description of the dynamic problem is first considered and a variable separation in the spatial domain is introduced. For both spatial coordinates x (beam axis coordinate) and z (thickness coordinate), a classical 3-node FE is used in the discretization. In addition, the load frequency is also introduced as a problem variable. The derived iterative methodology implies the computation of three 1D problems for each enrichment step used to represent the solution. The fixed-point method is employed to obtain the results for each of the N enrichment steps.
- The extension of the PGD formulation to multi-field analysis in solid mechanics. A new formulation based on the PGD method to solve the forced vibration problem in bi-dimensional laminated beams with piezoelectric layers is developed and validated. This would lead to the extension of the PGD approach to the parametric modelling of bimorph PEHDs.
- The adoption of a new semi-analytic approach based on the use of real measured traffic-induced vibration response as excitation in the power generation estimation. The computation of the expected power is proposed to be based on: i) the closed-form transfer function between base excitation and harvester output voltage, and, ii) the experimentally measured spectral density of the bridge acceleration. Therefore, broadband white Gaussian noise excitation is no longer considered as the base excitation.

On the basis of the research results reached in this thesis, the following conclusions can be remarked. On the new model analysis based on a separated representation:

- The proposed formulation has been validated through several numerical tests, including different composite and sandwich beam configurations with a great variety of slenderness ratios and boundary conditions.
- Results show a good agreement with exact elasticity solutions, higher-order theories and FE models.

- This study has showed the capability of the method to build all kinds of mode shapes, including complex thickness modes with non-uniform displacement distribution along x and z axis.
- The method has been proved to be successful in detecting even small variations in natural frequencies derived from different electrical boundary conditions, such as short circuit and open circuit conditions.
- The advantages of the proposed algorithm become relevant when the number of numerical layers increases and greater precision is required. In these cases the number of DOFs in the classical formulation of the problem grows exponentially and the separation of variables becomes a very useful tool to reduce the order and limit the computational cost. Here, the potential of the PGD formulation has been demonstrated by the accuracy of its results.

The main conclusions on the feasibility study of vibration energy harvesting from a highway bridge:

- The new approach has been used to evaluate the available power from real vibration of a bowstring highway bridge located in Palma del Río, Córdoba (Spain).
- Two different situations have been considered in the assessment of the harvested power: i) operational vibration records with the bridge open to regular traffic, ii) ambient vibrations with the bridge closed to traffic. The numerical results show that the energy harvested from ambient vibration is two orders of magnitude smaller than that obtained from operational vibration. Consequently, it could be stated that the level of traffic could condition the viability of a piezoelectric energy harvesting system.
- A parametric sensitivity study has been used to optimise the harvester mass according to the excitation and considerably increase the expected power (from nW to μW).
- This new approach enables a more realistic study of the application of energy harvesting technique to the power requirements of WSNs and other low-power electronic devices used in SHM. Broadband white Gaussian noise excitation is no longer considered as the base excitation since the computation of the expected power is proposed to be based on the experimentally measured bridge acceleration.
- The results show the potential of the semi-analytic approach to evaluate the expected power of piezoelectric energy harvesters subjected to a highway bridge excitation. This also opens up the possibility to confidently extend the approach to different base excitation mechanisms, such as the vibrations of railway bridges or footbridges.

On the whole, it can be concluded that the proposed objectives at the beginning of this thesis, as previously indicated in Section 1.3, have been successfully accomplished.

5.2 Ongoing and future research areas

In the light of the experience built-up over the development of this thesis, several lines for new and challenging research niches have been identified. Firstly, regarding the PGD-based modelling of the problem:

- The extension of the PGD approach to the parametric modelling of bimorph PEHDs could easily be addressed. The proposed method has been proved to be successful in detecting even small variations in natural frequencies derived from different electrical boundary conditions, such as short circuit and open circuit conditions. This opens up the possibility of confidently introducing electrical loads into the formulation, by adding an equivalent capacitance matrix to the dielectric matrix as in reference [124].
- The consideration of the system response to non-harmonic loads has not been addressed. An initial idea could be combining modal and harmonic analysis for defining a hybrid integration scheme as in [67, 165].

On the other hand, a more experimental approach could certainly extend the cutting edge of energy harvesting from structural vibrations.

- The analysis of the voltage output of PEHDs placed on real bridges would be of considerable value. This would allow a real quantification of the available energy, including possible system losses. This deployment would allow statistical analysis of the particularities associated with different types of structures. Energy collection systems for road bridges, railway bridges or footbridges could be optimised accordingly.
- Tackling the problem in footbridges would additionally entail the need to balance two conflicting strategies: vibration control and vibration energy harvesting. The increasingly slender and daring designs of the footbridges have led to significant episodes of dynamic resonance problems and have extensively developed the field of vibration control devices. Therefore, the dual-function device concept in such civil structures should be faced in order to be successful. When a vibration-based harvester is integrated with a vibration control methodology, a fundamental question arises as to whether or not these two objectives are consistent with each other. According to Cai and Zhu [164], when these objectives are conflicting, a trade-off between the optimizations is required, whereas when these objectives are consistent, the problem may be simplified as a single-objective optimization. In this line, an experimental campaign has been initiated in recent months on an ultra-lightweight footbridge placed in the Department of Continuum Mechanics and Structures of Universidad Politécnica de Madrid, from which we hope to obtain results in the short term.
- One of the key aspects of long-term monitoring is the location of the data acquisition nodes. Since the energy harvesting device will be placed inside the node, it will be necessary to combine the optimal sensor placement technique (OSP) for the correct modal identification of the structure [166] with an optimal location strategy

to maximise the harvested energy. Matching these two objectives can certainly be challenging. In the case of the optimal harvesting placement, the goal would be to ensure that the battery charge level is maintained in order to ensure the power supply of the node. Considering the stochastic nature of the host structure vibration, the probabilistic study of the excitation becomes necessary to this end.

Finally, the actual use of PEHDs for SHM is certainly the most challenging application. There are still many open issues that need to be addressed in line with optimising the resource consumption of the monitoring system's sensors. This is one of the specific objectives that will be pursued in the context of two R&D&I projects launched last years:

- *BRIDGEXT*: Life-extension of Ageing Bridges: Towards a Long-term Sustainable Structural Health Monitoring (PID2020-116644RB-I00, Ministerio de Ciencia e Innovación of Spain)
- *SMART-BRIDGES*: Smart Structural Health Monitoring for High-speed Railway Bridges (PLEC2021-007798, FEDER NextGenerationEU recovery plan)

The objectives of these projects are quite ambitious and multidisciplinary in approach. They involve important advances on: i) the development of advanced SHM methodologies, in the case of SMART-BRIDGES focusing on high-speed railway ageing bridges; ii) the evolution of monitoring technologies to the concept of Smart Sensors for long-term SHM; iii) the energy autonomy of the long-term monitoring system; iv) the prognosis of structural response based on data-driven decision. The application of the life extension via smart self-powered continuous monitoring and data-driven decision methodologies would open up new opportunities for infrastructure management and maintenance, greatly improving their safety and resilience to critical events caused by natural ageing or climate change. Energy autonomy is a key point of the system and is intended to be solved by vibration-based energy harvesting techniques, which would take the research works of this thesis to a higher technology readiness level.

Bibliography

[1] M Grieves and J Vickers. Digital twin: Mitigating unpredictable, undesirable emergent behavior in complex systems. In *Transdisciplinary perspectives on complex systems*, pages 85–113. Springer, 2017. URL *http://doi.org/10.1007/978-3-319-38756-7_4*.

[2] M Chiachío, J Chiachío, D Prescott, and J Andrews. Plausible petri nets as self-adaptive expert systems: A tool for infrastructure asset monitoring. *Computer-Aided Civil and Infrastructure Engineering*, 34(4):281–298, 2019. URL *http://doi.org/10.1111/mice.12427*.

[3] E García-Macías and F Ubertini. MOVA/MOSS: Two integrated software solutions for comprehensive structural health monitoring of structures. *Mechanical Systems and Signal Processing*, 143:106830, 2020. URL *http://doi.org/10.1016/j.ymssp.2020.106830*.

[4] M Azimi, A D Eslamlou, and G Pekcan. Data-driven structural health monitoring and damage detection through deep learning: State-of-the-art review. *Sensors*, 20 (10):2778, 2020. URL *http://doi.org/10.3390/s20102778*.

[5] E García-Macías, L Ierimonti, I Venanzi, and F Ubertini. An innovative methodology for online surrogate-based model updating of historic buildings using monitoring data. *International Journal of Architectural Heritage*, 15(1):92–112, 2021. URL *http://doi.org/10.1080/15583058.2019.1668495*.

[6] R Ibáñez, E Abisset-Chavanne, A Ammar, D González, E Cueto, A Huerta, J L Duval, and F Chinesta. A multidimensional data-driven sparse identification technique: the sparse proper generalized decomposition. *Complexity*, 2018:5608286, 2018. URL *http://doi.org/10.1155/2018/5608286*.

[7] P Seventekidis, D Giagopoulos, A Arailopoulos, and O Markogiannaki. Structural health monitoring using deep learning with optimal finite element model generated data. *Mechanical Systems and Signal Processing*, 145:106972, 2020. URL *http://doi.org/10.1016/j.ymssp.2020.106972*.

[8] P Seventekidis and D Giagopoulos. A combined finite element and hierarchical deep learning approach for structural health monitoring: Test on a pin-joint composite truss structure. *Mechanical Systems and Signal Processing*, 157:107735, 2021. URL *http://doi.org/10.1016/j.ymssp.2021.107735*.

[9] G Tsialiamanis, E Chatzi, N Dervilis, D Wagg, and K Worden. An application of generative adversarial networks in structural health monitoring. In *EURODYN 2020: Proceedings of the XI International Conference on Structural Dynamics*, volume 2, pages 3816–3831, 2020. ISBN 9780854329649.

[10] M H Soleimani-Babakamali, R Sepasdar, K Nasrollahzadeh, and R Sarlo. A system reliability approach to real-time unsupervised structural health monitoring without prior information. *Mechanical Systems and Signal Processing*, 171:108913, 2022. URL *http://doi.org/10.1016/j.ymssp.2022.108913*.

[11] F León-García, J M Palomares, and J Olivares. D2R-TED: Data-domain reduction model for threshold-based event detection in sensor networks. *Sensors*, 18(11): 3806, 2018. URL *http://doi.org/10.3390/s18113806*.

[12] F León-García, F J Rodríguez-Lozano, J Olivares, and J M Palomares. Data communication optimization for the evaluation of multivariate conditions in distributed scenarios. *IEEE Access*, 7:123473–123489, 2019. URL *http://doi.org/10.1109/ACCESS.2019.2936918*.

[13] N G Elvin, N Lajnef, and A A Elvin. Feasibility of structural monitoring with vibration powered sensors. *Smart Materials and Structures*, 15(4):977–986, 2006. URL *http://doi.org/10.1088/0964-1726/15/4/011*.

[14] J C Rodriguez, V Nico, and J Punch. A vibration energy harvester and power management solution for battery-free operation of wireless sensor nodes. *Sensors*, 19(17):3776, 2019. URL *http://doi.org/10.3390/s19173776*.

[15] C Wei and X Jing. A comprehensive review on vibration energy harvesting: Modelling and realization. *Renewable and Sustainable Energy Reviews*, 74:1–18, 2017. ISSN 1364-0321. URL *http://doi.org/10.1016/j.rser.2017.01.073*.

[16] P K Sharma and P V Baredar. Analysis on piezoelectric energy harvesting small scale device – a review. *Journal of King Saud University - Science*, 31(4):869–877, 2019. ISSN 1018-3647. URL *http://doi.org/10.1016/j.jksus.2017.11.002*.

[17] J Siang, M H Lim, and M Salman Leong. Review of vibration-based energy harvesting technology: Mechanism and architectural approach. *International Journal of Energy Research*, 42(5):1866–1893, 2018. URL *http://doi.org/10.1002/er.3986*.

[18] Standards Committee of the IEEE Ultrasonics, Ferroelectrics, and Frequency Control Society. IEEE Standard on Piezoelectricity. *ANSI/IEEE Std 176–1987*, 1988. URL *http://doi.org/10.1109/IEEESTD.1988.79638*.

[19] A Erturk and D J Inman. *Piezoelectric energy harvesting*. John Wiley & Sons, 2011. ISBN 978-0-470-68254-8.

[20] A Erturk and D J Inman. Parameter identification and optimization in piezoelectric energy harvesting: analytical relations, asymptotic analyses, and experimental validations. *Proceedings of the Institution of Mechanical Engineers, Part I: Journal of Systems and Control Engineering*, 225(4):485–496, 2011. URL *http://doi.org/10.1177/0959651810396280*.

[21] L Tang and J Wang. Modeling and analysis of cantilever piezoelectric energy harvester with a new-type dynamic magnifier. *Acta Mechanica*, 229(11):4643–4662, 2018. URL *http://doi.org/10.1007/s00707-018-2250-z*.

[22] A Ammar, B Mokdad, F Chinesta, and R Keunings. A new family of solvers for some classes of multidimensional partial differential equations encountered in kinetic theory modeling of complex fluids. *Journal of Non-Newtonian Fluid Mechanics*, 139(3):153–176, 2006. URL *http://doi.org/10.1016/j.jnnfm.2006.07.007*.

[23] F Chinesta, R Keunings, and A Leygue. *The proper generalized decomposition for advanced numerical simulations: A primer*. Springer Science & Business Media, 2013. ISBN 978-3-319-02864-4.

[24] Y Tanigawa, H Murakami, and Y Ootao. Transient thermal stress analysis of a laminated composite beam. *Journal of Thermal Stresses*, 12(1):25–39, 1989. URL *http://doi.org/10.1080/01495738908961952*.

[25] S M Nabi and N Ganesan. A generalized element for the free vibration analysis of composite beams. *Computers & Structures*, 51(5):607–610, 1994. URL *http://doi.org/10.1016/0045-7949(94)90068-X*.

[26] Y Teboub and P Hajela. Free vibration of generally layered composite beams using symbolic computations. *Composite Structures*, 33(3):123–134, 1995. URL *http://doi.org/10.1016/0263-8223(95)00112-3*.

[27] V Yıldırım. Effect of the longitudinal to transverse moduli ratio on the in-plane natural frequencies of symmetric cross-ply laminated beams by the stiffness method. *Composite Structures*, 50(3):319–326, 2000. URL *http://doi.org/10.1016/S0263-8223(00)00124-0*.

[28] A Chakraborty, D Roy Mahapatra, and S Gopalakrishnan. Finite element analysis of free vibration and wave propagation in asymmetric composite beams with structural discontinuities. *Composite Structures*, 55(1):23–36, 2002. URL *http://doi.org/10.1016/S0263-8223(01)00130-1*.

[29] V K Goyal and R K Kapania. A shear-deformable beam element for the analysis of laminated composites. *Finite Elements in Analysis and Design*, 43(6):463–477, 2007. URL *http://doi.org/10.1016/j.finel.2006.11.011*.

[30] L Jun, H Hongxing, and S Rongying. Dynamic finite element method for generally laminated composite beams. *International Journal of Mechanical Sciences*, 50(3): 466–480, 2008. URL *http://doi.org/10.1016/j.ijmecsci.2007.09.014*.

[31] K Chandrashekhara and K M Bangera. Free vibration of composite beams using a refined shear flexible beam element. *Computers & Structures*, 43(4):719–727, 1992. URL *http://doi.org/10.1016/0045-7949(92)90514-Z*.

[32] G Shi and K Y Lam. Finite element vibration analysis of composite beams based on higher-order beam theory. *Journal of Sound and Vibration*, 219(4):707–721, 1999. URL *http://doi.org/10.1006/jsvi.1998.1903*.

[33] H Matsunaga. Vibration and buckling of multilayered composite beams according to higher order deformation theories. *Journal of Sound and Vibration*, 246(1): 47–62, 2001. URL *http://doi.org/10.1006/jsvi.2000.3627*.

[34] M V V S Murthy, D Roy Mahapatra, K Badarinarayana, and S Gopalakrishnan. A refined higher order finite element for asymmetric composite beams. *Composite Structures*, 67(1):27–35, 2005. URL *http://doi.org/10.1016/j.compstruct.2004.01.005*.

[35] T Kant, S R Marur, and G S Rao. Analytical solution to the dynamic analysis of laminated beams using higher order refined theory. *Composite Structures*, 40(1): 1–9, 1997. URL *http://doi.org/10.1016/S0263-8223(97)00133-5*.

[36] M K Rao, Y M Desai, and M R Chitnis. Free vibrations of laminated beams using mixed theory. *Composite Structures*, 52(2):149–160, 2001. URL *http://doi.org/10.1016/S0263-8223(00)00162-8*.

[37] P Subramanian. Dynamic analysis of laminated composite beams using higher order theories and finite elements. *Composite Structures*, 73(3):342–353, 2006. URL *http://doi.org/10.1016/j.compstruct.2005.02.002*.

[38] R P Shimpi and A V Ainapure. A beam finite element based on layerwise trigonometric shear deformation theory. *Composite Structures*, 53(2):153–162, 2001. URL *http://doi.org/10.1016/S0263-8223(00)00186-0*.

[39] M Tahani. Analysis of laminated composite beams using layerwise displacement theories. *Composite Structures*, 79(4):535–547, 2007. URL *http://doi.org/10.1016/j.compstruct.2006.02.019*.

[40] W Zhen and C Wanji. An assessment of several displacement-based theories for the vibration and stability analysis of laminated composite and sandwich beams. *Composite Structures*, 84(4):337–349, 2008. URL *http://doi.org/10.1016/j.compstruct.2007.10.005*.

[41] M Cho and R R Parmerter. Efficient higher order composite plate theory for general lamination configurations. *AIAA Journal*, 31(7):1299–1306, 1993. URL *http://doi.org/10.2514/3.11767*.

[42] R C Averill and Y C Yip. Thick beam theory and finite element model with zig-zag sublaminate approximations. *AIAA Journal*, 34(8):1627–1632, 1996. URL *http://doi.org/10.2514/3.13281*.

[43] S Kapuria, P C Dumir, and A Ahmed. An efficient higher order zigzag theory for composite and sandwich beams subjected to thermal loading. *International Journal of Solids and Structures*, 40(24):6613–6631, 2003. URL *http://doi.org/10.1016/j.ijsolstr.2003.08.014*.

[44] P Vidal and O Polit. A family of sinus finite elements for the analysis of rectangular laminated beams. *Composite Structures*, 84(1):56–72, 2008. URL *http://doi.org/10.1016/j.compstruct.2007.06.009*.

[45] P Vidal and O Polit. A refined sine-based finite element with transverse normal deformation for the analysis of laminated beams under thermomechanical loads. *Journal of Mechanics of Materials and Structures*, 4(6):1127–1155, 2009. URL *http://doi.org/10.2140/jomms.2009.4.1127*.

[46] P Vidal and O Polit. A sine finite element using a zig-zag function for the analysis of laminated composite beams. *Composites Part B: Engineering*, 42(6):1671–1682, 2011. URL *http://doi.org/10.1016/j.compositesb.2011.03.012*.

[47] E Carrera. Historical review of Zig-Zag theories for multilayered plates and shells. *Applied Mechanics Reviews*, 56(3):287–308, 2003. URL *http://doi.org/10.1115/1.1557614*.

[48] E Carrera. Evaluation of layerwise mixed theories for laminated plates analysis. *AIAA Journal*, 36(5):830–839, 1998. URL *http://doi.org/10.2514/2.444*.

[49] E Carrera and L Demasi. Classical and advanced multilayered plate elements based upon PVD and RMVT. Part 1: Derivation of finite element matrices. *International Journal for Numerical Methods in Engineering*, 55(2):191–231, 2002. URL *http://doi.org/10.1002/nme.492*.

[50] E Carrera and L Demasi. Classical and advanced multilayered plate elements based upon PVD and RMVT. Part 2: Numerical implementations. *International Journal for Numerical Methods in Engineering*, 55(3):253–291, 2002. URL *http://doi.org/10.1002/nme.493*.

[51] A K Noor and W S Burton. Assessment of Computational Models for Multilayered Composite Shells. *Applied Mechanics Reviews*, 43(4):67–97, 1990. URL *http://doi.org/10.1115/1.3119162*.

[52] J N Reddy. *Mechanics of Laminated Composite Plates and Shells: Theory and Analysis*. CRC Press, Boca Raton, FL, 1997. ISBN 978-0-429-21069-3. URL *http://doi.org/10.1201/b12409*.

[53] E Carrera. Theories and finite elements for multilayered, anisotropic, composite plates and shells. *Archives of computational methods in engineering: state of the art reviews*, 9(2):87–140, 2002. URL *http://doi.org/10.1007/BF02736649*.

[54] Y X Zhang and C H Yang. Recent developments in finite element analysis for laminated composite plates. *Composite Structures*, 88(1):147–157, 2009. URL *http://doi.org/10.1016/j.compstruct.2008.02.014*.

[55] T. Kant and K Swaminathan. Estimation of transverse/interlaminar stresses in laminated composites – a selective review and survey of current developments. *Composite Structures*, 49(1):65–75, 2000. URL *http://doi.org/10.1016/S0263-8223(99)00126-9*.

[56] R K Kapania and S Raciti. Recent Advances in Analysis of Laminated Beams and Plates, Part II: Vibrations and Wave Propagation. *AIAA Journal*, 27(7):935–946, 1989. URL *http://doi.org/10.2514/3.59909*.

[57] P Ladevèze. *Nonlinear computational structural mechanics: new approaches and non-incremental methods of calculation*. Springer New York, NY, 1999. ISBN 978-0-387-98594-7.

[58] O Allix and P Vidal. A new multi-solution approach suitable for structural identification problems. *Computer Methods in Applied Mechanics and Engineering*, 191 (25):2727–2758, 2002. URL *http://doi.org/10.1016/S0045-7825(02)00211-6*.

[59] D Néron, P-A Boucard, and N Relun. Time-space PGD for the rapid solution of 3D nonlinear parametrized problems in the many-query context. *International Journal for Numerical Methods in Engineering*, 103(4):275–292, 2015. URL *http://doi.org/10.1002/nme.4893*.

[60] B Bognet, F Bordeu, F Chinesta, A Leygue, and A Poitou. Advanced simulation of models defined in plate geometries: 3D solutions with 2D computational complexity. *Computer Methods in Applied Mechanics and Engineering*, 201-204:1–12, 2012. URL *http://doi.org/10.1016/j.cma.2011.08.025*.

[61] P Vidal, L Gallimard, and O Polit. Assessment of a composite beam finite element based on the proper generalized decomposition. *Composite Structures*, 94(5): 1900–1910, 2012. URL *http://doi.org/10.1016/j.compstruct.2011.12.016*.

[62] P Vidal, L Gallimard, and O Polit. Composite beam finite element based on the Proper Generalized Decomposition. *Computers & Structures*, 102-103:76–86, 2012. URL *http://doi.org/10.1016/j.compstruc.2012.03.008*.

[63] P Vidal, L Gallimard, and O Polit. Proper Generalized Decomposition and layer-wise approach for the modeling of composite plate structures. *International Journal of Solids and Structures*, 50(14):2239–2250, 2013. URL *http://doi.org/10.1016/j.ijsolstr.2013.03.034*.

[64] H Tertrais, R Ibañez, A Barasinski, Ch Ghnatios, and F Chinesta. On the Proper Generalized Decomposition applied to microwave processes involving multilayered components. *Mathematics and Computers in Simulation*, 156:347–363, 2019. URL *http://doi.org/10.1016/j.matcom.2018.09.008*.

[65] A Nouy. A priori model reduction through Proper Generalized Decomposition for solving time-dependent partial differential equations. *Computer Methods in Applied Mechanics and Engineering*, 199(23):1603–1626, 2010. URL *http://doi.org/10.1016/j.cma.2010.01.009*.

[66] F Chinesta, A Ammar, A Leygue, and R Keunings. An overview of the proper generalized decomposition with applications in computational rheology. *Journal of Non-Newtonian Fluid Mechanics*, 166(11):578–592, 2011. URL *http://doi.org/10.1016/j.jnnfm.2010.12.012*.

[67] M H Malik, D Borzacchiello, J V Aguado, and F Chinesta. Advanced parametric space-frequency separated representations in structural dynamics: A harmonic–modal hybrid approach. *Comptes Rendus Mécanique*, 346(7):590–602, 2018. URL *http://doi.org/10.1016/j.crme.2018.04.005*.

[68] S Kapuria, P C Dumir, and N K Jain. Assessment of zigzag theory for static loading, buckling, free and forced response of composite and sandwich beams. *Composite Structures*, 64(3):317–327, 2004. URL *http://doi.org/10.1016/j.compstruct.2003.08.013*.

[69] P Vidal and O Polit. Vibration of multilayered beams using sinus finite elements with transverse normal stress. *Composite Structures*, 92(6):1524–1534, 2010. URL *http://doi.org/10.1016/j.compstruct.2009.10.009*.

[70] X Li and D Liu. Generalized laminate theories based on double superposition hypothesis. *International Journal for Numerical Methods in Engineering*, 40(7):1197–1212, 1997. URL *http://doi.org/10.1002/(SICI)1097-0207(19970415)40:7⟨1197::AID-NME109⟩3.0.CO;2-B*.

[71] M Aydogdu. Vibration analysis of cross-ply laminated beams with general boundary conditions by Ritz method. *International Journal of Mechanical Sciences*, 47(11):1740–1755, 2005. URL *http://doi.org/10.1016/j.ijmecsci.2005.06.010*.

[72] A Duarte B L Ferreira, P R O Nóvoa, and A Torres Marques. Multifunctional Material Systems: A state-of-the-art review. *Composite Structures*, 151:3–35, 2016. URL *http://doi.org/10.1016/j.compstruct.2016.01.028*.

[73] R F Gibson. A review of recent research on mechanics of multifunctional composite materials and structures. *Composite Structures*, 92(12):2793–2810, 2010. URL *http://doi.org/10.1016/j.compstruct.2010.05.003*.

[74] I Chopra. Review of State of Art of Smart Structures and Integrated Systems. *AIAA Journal*, 40(11):2145–2187, 2002. URL *http://doi.org/10.2514/2.1561*.

[75] P Gaudenzi. *Smart Structures: Physical Behaviour, Mathematical Modelling and Applications*. John Wiley & Sons, 2009. ISBN 978-0-470-68243-2.

[76] Zhiwei Zhang, H Xiang, and Z Shi. Mechanism exploration of piezoelectric energy harvesting from vibration in beams subjected to moving harmonic loads. *Composite Structures*, 179:368–376, 2017. URL *http://doi.org/10.1016/j.compstruct.2017.07.013*.

[77] Q Lu, Liwu Liu, F Scarpa, J Leng, and Y Liu. A novel composite multi-layer piezoelectric energy harvester. *Composite Structures*, 201:121–130, 2018. URL *http://doi.org/10.1016/j.compstruct.2018.06.024*.

[78] S Banerjee and S Roy. A Timoshenko like model for piezoelectric energy harvester with shear mode. *Composite Structures*, 204:677–688, 2018. URL *http://doi.org/10.1016/j.compstruct.2018.07.117*.

[79] M Akbar and J L Curiel-Sosa. An iterative finite element method for piezoelectric energy harvesting composite with implementation to lifting structures under Gust Load Conditions. *Composite Structures*, 219:97–110, 2019. URL *http://doi.org/10.1016/j.compstruct.2019.03.070*.

[80] A Benjeddou. Advances in piezoelectric finite element modeling of adaptive structural elements: a survey. *Computers & Structures*, 76(1):347–363, 2000. URL *http://doi.org/10.1016/S0045-7949(99)00151-0*.

[81] D A Saravanos and P R Heyliger. Mechanics and Computational Models for Laminated Piezoelectric Beams, Plates, and Shells. *Applied Mechanics Reviews*, 52(10):305–320, 1999. URL *http://doi.org/10.1115/1.3098918*.

[82] E Carrera, S Brischetto, and P Nali. *Plates and Shells for Smart Structures: Classical and Advanced Theories for Modeling and Analysis*. John Wiley & Sons, 2011. ISBN 978-1-119-95112-4.

[83] P Vidal, M D'Ottavio, M Ben Thaïer, and O Polit. An efficient finite shell element for the static response of piezoelectric laminates. *Journal of Intelligent Material Systems and Structures*, 22(7):671–690, 2011. URL *http://doi.org/10.1177/1045389X11402863*.

[84] E F Crawley and J de Luis. Use of piezoelectric actuators as elements of intelligent structures. *AIAA Journal*, 25(10):1373–1385, 1987. URL *http://doi.org/10.2514/3.9792*.

[85] H S Tzou and M Gadre. Theoretical analysis of a multi-layered thin shell coupled with piezoelectric shell actuators for distributed vibration controls. *Journal of Sound and Vibration*, 132(3):433–450, 1989. URL *http://doi.org/10.1016/0022-460X(89)90637-8*.

[86] B-T Wang and C A Rogers. Laminate Plate Theory for Spatially Distributed Induced Strain Actuators. *Journal of Composite Materials*, 25(4):433–452, 1991. URL *http://doi.org/10.1177/002199839102500405*.

[87] C K Sung, T F Chen, and S G Chen. Piezoelectric Modal Sensor/Actuator Design for Monitoring/Generating Flexural and Torsional Vibrations of Cylindrical Shells. *Journal of Vibration and Acoustics*, 118(1):48–55, 1996. URL *http://doi.org/10.1115/1.2889634*.

[88] H Allik and T J R Hughes. Finite element method for piezoelectric vibration. *International Journal for Numerical Methods in Engineering*, 2(2):151–157, 1970. URL *http://doi.org/10.1002/nme.1620020202*.

[89] H S Tzou and C I Tseng. Distributed piezoelectric sensor/actuator design for dynamic measurement/control of distributed parameter systems: A piezoelectric finite element approach. *Journal of Sound and Vibration*, 138(1):17–34, 1990. URL *http://doi.org/10.1016/0022-460X(90)90701-Z*.

[90] K Xu, A K Noor, and Y Y Tang. Three-dimensional solutions for coupled thermoelectroelastic response of multilayered plates. *Computer Methods in Applied Mechanics and Engineering*, 126(3):355–371, 1995. URL *http://doi.org/10.1016/0045-7825(95)00825-L*.

[91] J N Reddy. An evaluation of equivalent-single-layer and layerwise theories of composite laminates. *Composite Structures*, 25(1):21–35, 1993. URL *http://doi.org/10.1016/0263-8223(93)90147-I*.

[92] A Suleman and V B Venkayya. A Simple Finite Element Formulation for a Laminated Composite Plate with Piezoelectric Layers. *Journal of Intelligent Material Systems and Structures*, 6(6):776–782, 1995. URL *http://doi.org/10.1177/1045389X9500600605*.

[93] A H Sheikh, P Topdar, and S Halder. An appropriate FE model for through-thickness variation of displacement and potential in thin/moderately thick smart laminates. *Composite Structures*, 51(4):401–409, 2001. URL *http://doi.org/10.1016/S0263-8223(00)00156-2*.

[94] S Y Wang. A finite element model for the static and dynamic analysis of a piezoelectric bimorph. *International Journal of Solids and Structures*, 41(15):4075–4096, 2004. URL *http://doi.org/10.1016/j.ijsolstr.2004.02.058*.

[95] C Y K Chee, L Tong, and G P Steven. Mixed model for composite beams with piezoelectric actuators and sensors. *Smart Materials and Structures*, 8(3):417–432, 1999. URL *http://doi.org/10.1088/0964-1726/8/3/313*.

[96] R P Thornburgh and A Chattopadhyay. Simultaneous Modeling of Mechanical and Electrical Response of Smart Composite Structures. *AIAA Journal*, 40(8):1603–1610, 2002. URL *http://doi.org/10.2514/2.1830*.

[97] H Fukunaga, N Hu, and G X Ren. FEM modeling of adaptive composite structures using a reduced higher-order plate theory via penalty functions. *International Journal of Solids and Structures*, 38(48):8735–8752, 2001. URL *http://doi.org/10.1016/S0020-7683(01)00072-5*.

[98] J A Mitchell and J N Reddy. A refined hybrid plate theory for composite laminates with piezoelectric laminae. *International Journal of Solids and Structures*, 32(16): 2345–2367, 1995. URL *http://doi.org/10.1016/0020-7683(94)00229-P*.

[99] X Shu. Free vibration of laminated piezoelectric composite plates based on an accurate theory. *Composite Structures*, 67(4):375–382, 2005. URL *http://doi.org/10.1016/j.compstruct.2004.01.022*.

[100] D A Saravanos and P R Heyliger. Coupled layerwise analysis of composite beams with embedded piezoelectric sensors and actuators. *Journal of Intelligent Material Systems and Structures*, 6(3):350–363, 1995. URL *http://doi.org/10.1177/1045389X9500600306*.

[101] Z K Kusculuoglu, B Fallahi, and T J Royston. Finite element model of a beam with a piezoceramic patch actuator. *Journal of Sound and Vibration*, 276(1):27–44, 2004. URL *http://doi.org/10.1016/j.jsv.2003.07.014*.

[102] J E Semedo Garção, C M Mota Soares, C A Mota Soares, and J N Reddy. Analysis of laminated adaptive plate structures using layerwise finite element models. *Computers & Structures*, 82(23):1939–1959, 2004. URL *http://doi.org/10.1016/j.compstruc.2003.10.024*.

[103] R García Lage, C M Mota Soares, C A Mota Soares, and J N Reddy. Analysis of adaptive plate structures by mixed layerwise finite elements. *Composite Structures*, 66(1):269–276, 2004. URL *http://doi.org/10.1016/j.compstruct.2004.04.048*.

[104] P Heyliger, G Ramirez, and D Saravanos. Coupled discrete-layer finite elements for laminated piezoelectric platess. *Communications in Numerical Methods in Engineering*, 10(12):971–981, 1994. URL *http://doi.org/10.1002/cnm.1640101203*.

[105] D A Saravanos, P R Heyliger, and D A Hopkins. Layerwise mechanics and finite element for the dynamic analysis of piezoelectric composite plates. *International Journal of Solids and Structures*, 34(3):359–378, 1997. URL *http://doi.org/10.1016/S0020-7683(96)00012-1*.

[106] A Robaldo, E Carrera, and A Benjeddou. A unified formulation for finite element analysis of piezoelectric adaptive plates. *Computers & Structures*, 84(22):1494–1505, 2006. URL *http://doi.org/10.1016/j.compstruc.2006.01.029*.

[107] H S Tzou and R Ye. Analysis of piezoelastic structures with laminated piezoelectric triangle shell elements. *AIAA Journal*, 34(1):110–115, 1996. URL *http://doi.org/10.2514/3.12907*.

[108] S Ambartsumyan. *Theory of anisotropic plates: Strength, Stability, Vibration*. Technomic Publishing, Co., 1970. ISBN 9780891166542.

[109] J Oh and M Cho. A finite element based on cubic zig-zag plate theory for the prediction of thermo-electric-mechanical behaviors. *International Journal of Solids and Structures*, 41(5):1357–1375, 2004. URL *http://doi.org/10.1016/j.ijsolstr.2003.10.019*.

[110] S Kapuria. An efficient coupled theory for multilayered beams with embedded piezoelectric sensory and active layers. *International Journal of Solids and Structures*, 38(50):9179–9199, 2001. URL *http://doi.org/10.1016/S0020-7683(01)00112-3*.

[111] S Kapuria and N Alam. Efficient layerwise finite element model for dynamic analysis of laminated piezoelectric beams. *Computer Methods in Applied Mechanics and Engineering*, 195(19):2742–2760, 2006. URL *http://doi.org/10.1016/j.cma.2005.06.008*.

[112] M Cho and J Oh. Higher order zig-zag theory for fully coupled thermoelectric–mechanical smart composite plates. *International Journal of Solids and Structures*, 41(5):1331–1356, 2004. URL *http://doi.org/10.1016/j.ijsolstr.2003.10.020*.

[113] M D'Ottavio and B Kröplin. An Extension of Reissner Mixed Variational Theorem to Piezoelectric Laminates. *Mechanics of Advanced Materials and Structures*, 13 (2):139–150, 2006. URL *http://doi.org/10.1080/15376490500451718*.

[114] E Carrera and P Nali. Mixed piezoelectric plate elements with direct evaluation of transverse electric displacement. *International Journal for Numerical Methods in Engineering*, 80(4):403–424, 2009. URL *http://doi.org/10.1002/nme.2641*.

[115] M Savoia and J N Reddy. A Variational Approach to Three-Dimensional Elasticity Solutions of Laminated Composite Plates. *Journal of Applied Mechanics*, 59(2S): S166–S175, 1992. URL *http://doi.org/10.1115/1.2899483*.

[116] M Infantes, P Vidal, R Castro-Triguero, L Gallimard, E García-Macías, and O Polit. Forced vibration analysis of composite beams based on the variable separation method. *Mechanics of Advanced Materials and Structures*, 28(6):618–634, 2021. URL *http://doi.org/10.1080/15376494.2019.1578015*.

[117] P Vidal, L Gallimard, and O Polit. Modeling of piezoelectric plates with variables separation for static analysis. *Smart Materials and Structures*, 25(5):055043, 2016. URL *http://doi.org/10.1088/0964-1726/25/5/055043*.

[118] A Fernandes. *Modèle et étude de composants piézoélectriques: applications aux structures multifonctionnelles*. PhD thesis, University Paris VI, 2000.

[119] S B Beheshti-Aval and M Lezgy-Nazargah. Coupled refined layerwise theory for dynamic free and forced response of piezoelectric laminated composite and sandwich beams. *Meccanica*, 48(6):1479–1500, 2013. URL *http://doi.org/10.1007/s11012-012-9679-2*.

[120] P Heyliger and S Brooks. Free vibration of piezoelectric laminates in cylindrical bending. *International Journal of Solids and Structures*, 32(20):2945–2960, 1995. URL *http://doi.org/10.1016/0020-7683(94)00270-7*.

[121] P Vidal, L Gallimard, and O Polit. Free vibration analysis of composite plates based on a variable separation method. *Composite Structures*, 230:111493, 2019. URL *http://doi.org/10.1016/j.compstruct.2019.111493*.

[122] A Ammar and F Chinesta. Circumventing curse of dimensionality in the solution of highly multidimensional models encountered in quantum mechanics using meshfree finite sums decomposition. In *Meshfree methods for partial differential equations IV*, pages 1–17. Springer, Berlin, Heidelberg, 2008. URL *http://doi.org/10.1007/978-3-540-79994-8_1*.

[123] E Cancès, V Ehrlacher, and T Lelièvre. Greedy algorithms for high-dimensional eigenvalue problems. *Constructive Approximation*, 40(3):387–423, 2014. URL *http://doi.org/10.1007/s00365-014-9266-y*.

[124] Z Qin, H Talleb, S Yan, X Xu, and Z Ren. Application of PGD on parametric modeling of a piezoelectric energy harvester. *IEEE Transactions on Magnetics*, 52: 1–11, 2016. URL *http://doi.org/10.1109/TMAG.2016.2591001*.

[125] S Roundy, P K Wright, and J Rabaey. A study of low level vibrations as a power source for wireless sensor nodes. *Computer Communications*, 26(11):1131–1144, 2003. URL *http://doi.org/10.1016/S0140-3664(02)00248-7*.

[126] Y Li, K Tao, B George, and Z Tan. Harvesting vibration energy: Technologies and challenges. *IEEE Industrial Electronics Magazine*, 15(1):30–39, 2021. URL *http://doi.org/10.1109/MIE.2020.2978219*.

[127] G Poulin, E Sarraute, and F Costa. Generation of electrical energy for portable devices: Comparative study of an electromagnetic and a piezoelectric system. *Sensors and Actuators A: Physical*, 116(3):461–471, 2004. URL *http://doi.org/10.1016/j.sna.2004.05.013*.

[128] S Roundy and P K Wright. A piezoelectric vibration based generator for wireless electronics. *Smart Materials and Structures*, 13(5):1131–1142, 2004. URL *http://doi.org/10.1088/0964-1726/13/5/018*.

[129] H A Sodano, G Park, and D J Inman. Estimation of electric charge output for piezoelectric energy harvesting. *Strain*, 40(2):49–58, 2004. URL *http://doi.org/10.1111/j.1475-1305.2004.00120.x*.

[130] S Roundy. On the effectiveness of vibration-based energy harvesting. *Journal of Intelligent Material Systems and Structures*, 16(10):809–823, 2005. URL *http://doi.org/10.1177/1045389X05054042*.

[131] E Lefeuvre, A Badel, C Richard, and D Guyomar. Piezoelectric energy harvesting device optimization by synchronous electric charge extraction. *Journal of Intelligent Material Systems and Structures*, 16(10):865–876, 2005. URL *http://doi.org/10.1177/1045389X05056859*.

[132] J M Renno, M F Daqaq, and D J Inman. On the optimal energy harvesting from a vibration source. *Journal of Sound and Vibration*, 320(1):386–405, 2009. URL *http://doi.org/10.1016/j.jsv.2008.07.029*.

[133] Z Yang, S Zhou, J Zu, and D J Inman. High-performance piezoelectric energy harvesters and their applications. *Joule*, 2(4):642–697, 2018. URL *http://doi.org/10.1016/j.joule.2018.03.011*.

[134] C Covaci and A Gontean. Piezoelectric energy harvesting solutions: A review. *Sensors*, 20(12):3512, 2020. URL *http://doi.org/10.3390/s20123512*.

[135] Q Cai and S Zhu. Unified strategy for overall impedance optimization in vibration-based electromagnetic energy harvesters. *International Journal of Mechanical Sciences*, 165:105198, 2020. URL *http://doi.org/10.1016/j.ijmecsci.2019.105198*.

[136] M Safaei, H A Sodano, and S R Anton. A review of energy harvesting using piezoelectric materials: state-of-the-art a decade later (2008–2018). *Smart Materials and Structures*, 28(11):113001, 2019. URL *http://doi.org/10.1088/1361-665x/ab36e4*.

[137] N G Stephen. On energy harvesting from ambient vibration. *Journal of Sound and Vibration*, 293(1-2):409–425, 2006. URL *http://doi.org/10.1016/j.jsv.2005.10.003*.

[138] E Lefeuvre, A Badel, C Richard, and D Guyomar. Energy harvesting using piezoelectric materials: Case of random vibrations. *Journal of Electroceramics*, 19(4): 349–355, 2007. URL *http://doi.org/10.1007/s10832-007-9051-4*.

[139] S Adhikari, M I Friswell, and D J Inman. Piezoelectric energy harvesting from broadband random vibrations. *Smart Materials and Structures*, 18(11):115005, 2009. URL *http://doi.org/10.1088/0964-1726/18/11/115005*.

[140] S Zhao and A Erturk. Electroelastic modeling and experimental validations of piezoelectric energy harvesting from broadband random vibrations of cantilevered bimorphs. *Smart Materials and Structures*, 22(1):015002, 2013. URL *http://doi.org/10.1088/0964-1726/22/1/015002*.

[141] Y Amini, P Fatehi, M Heshmati, and H Parandvar. Time domain and frequency domain analysis of functionally graded piezoelectric harvesters subjected to random vibration: Finite element modeling. *Composite Structures*, 136:384–393, 2016. URL *http://doi.org/10.1016/j.compstruct.2015.10.029*.

[142] H Yoon and B D Youn. Stochastic quantification of the electric power generated by a piezoelectric energy harvester using a time-frequency analysis under non-stationary random vibrations. *Smart Materials and Structures*, 23(4):045035, 2014. URL *http://doi.org/10.1088/0964-1726/23/4/045035*.

[143] H Yoon, M Kim, C S Park, and B D Youn. Time-varying output performances of piezoelectric vibration energy harvesting under nonstationary random vibrations. *Smart Materials and Structures*, 27(1):015004, 2018. URL *http://doi.org/10.1088/1361-665X/aa95ed*.

[144] S Adhikari, M I Friswell, G Litak, and H H Khodaparast. Design and analysis of vibration energy harvesters based on peak response statistics. *Smart Materials and Structures*, 25(6):065009, 2016. URL *http://doi.org/10.1088/0964-1726/25/6/065009*.

[145] W Shen, S Zhu, and H Zhu. Experimental study on using electromagnetic devices on bridge stay cables for simultaneous energy harvesting and vibration damping. *Smart Materials and Structures*, 25(6):065011, 2016. URL *http://doi.org/10.1088/0964-1726/25/6/065011*.

[146] W Shen, S Zhu, and H Zhu. Unify energy harvesting and vibration control functions in randomly excited structures with electromagnetic devices. *Journal of Engineering Mechanics*, 145(1):04018115, 2019. URL *http://doi.org/10.1061/(ASCE)EM.1943-7889.0001548*.

[147] T V Galchev, J McCullagh, R L Peterson, and K Najafi. Harvesting traffic-induced vibrations for structural health monitoring of bridges. *Journal of Micromechanics and Microengineering*, 21(10):104005, 2011. URL *http://doi.org/10.1088/0960-1317/21/10/104005*.

[148] F U Khan and I Ahmad. Review of energy harvesters utilizing bridge vibrations. *Shock and Vibration*, 2016:1340402, 2016. URL *http://doi.org/10.1155/2016/1340402*.

[149] S F Ali, M I Friswell, and S Adhikari. Analysis of energy harvesters for highway bridges. *Journal of Intelligent Material Systems and Structures*, 22(16):1929–1938, 2011. URL *http://doi.org/10.1016/S2095-4956(13)60085-6*.

[150] A Erturk. Piezoelectric energy harvesting for civil infrastructure system applications: Moving loads and surface strain fluctuations. *Journal of Intelligent Material Systems and Structures*, 22(17):1959–1973, 2011. URL *http://doi.org/10.1177/1045389x11420593*.

[151] Y Amini, M Heshmati, P Fatehi, and S E Habibi. Piezoelectric energy harvesting from vibrations of a beam subjected to multi-moving loads. *Applied Mathematical Modelling*, 49:1–16, 2017. URL *http://doi.org/10.1016/j.apm.2017.04.043*.

[152] K Bendine, M Hamdaoui, and B F Boukhoulda. Piezoelectric energy harvesting from a bridge subjected to time-dependent moving loads using finite elements. *Arabian Journal for Science and Engineering*, 44(6):5743–5763, 2019. URL *http://doi.org/10.1007/s13369-019-03721-0*.

[153] Z Zhang, L Tang, and H Xiang. Piezoelectric energy harvesting from bridge vibrations using different models for moving vehicles. *Journal of Aerospace Engineering*, 32(2):04018141, 2019. URL *http://doi.org/10.1061/(ASCE)AS.1943-5525.0000968*.

[154] M Peigney and D Siegert. Piezoelectric energy harvesting from traffic-induced bridge vibrations. *Smart Materials and Structures*, 22(9):095019, 2013. URL *http://doi.org/10.1088/0964-1726/22/9/095019*.

[155] N Kaur, D Mahesh, and S Singamsetty. An experimental study on piezoelectric energy harvesting from wind and ambient structural vibrations for wireless structural health monitoring. *Advances in Structural Engineering*, 23(5):1010–1023, 2020. URL *http://doi.org/10.1177/1369433219886956*.

[156] P Cahill, B Hazra, R Karoumi, A Mathewson, and V Pakrashi. Vibration energy harvesting based monitoring of an operational bridge undergoing forced vibration and train passage. *Mechanical Systems and Signal Processing*, 106:265–283, 2018. URL *http://doi.org/10.1016/j.ymssp.2018.01.007*.

[157] A Romero, J C Cámara-Molina, E Moliner, P Galvín, and M D Martínez-Rodrigo. Energy harvesting analysis in railway bridges: An approach based on modal decomposition. *Mechanical Systems and Signal Processing*, 160:107848, 2021. URL *http://doi.org/10.1016/j.ymssp.2021.107848*.

[158] C Demartino, G Quaranta, C Maruccio, and V Pakrashi. Feasibility of energy harvesting from vertical pedestrian-induced vibrations of footbridges for smart monitoring applications. *Computer-Aided Civil and Infrastructure Engineering*, 37 (8):1044–1065. URL *http://doi.org/10.1111/mice.12777*.

[159] E Arroyo, A Badel, F Formosa, Y Wu, and J Qiu. Comparison of electromagnetic and piezoelectric vibration energy harvesters: Model and experiments. *Sensors and Actuators A: Physical*, 183:148–156, 2012. URL *http://doi.org/10.1016/j.sna.2012.04.033*.

[160] E García-Macías, R Castro-Triguero, R Gallego, J Carretero, and M Gómez-Casero. Operational modal analysis and detection of non-linear structural behavior of bowstring arch bridge. In *Proceedings of the 6th International Operational Modal Analysis Conference*, Gijón, Spain, 2015.

[161] N E du Toit and B L Wardle. Experimental verification of models for microfabricated piezoelectric vibration energy harvesters. *AIAA Journal*, 45(5):1126–1137, 2007. URL *http://doi.org/10.2514/1.25047*.

[162] A Erturk and D J Inman. Issues in mathematical modeling of piezoelectric energy harvesters. *Smart Materials and Structures*, 17(6):065016, 2008. URL *http://doi.org/10.1088/0964-1726/17/6/065016*.

[163] Y Liao and J Liang. Maximum power, optimal load, and impedance analysis of piezoelectric vibration energy harvesters. *Smart Materials and Structures*, 27(7): 075053, 2018. URL *http://doi.org/10.1088/1361-665x/aaca56*.

[164] Q Cai and S Zhu. The nexus between vibration-based energy harvesting and structural vibration control: A comprehensive review. *Renewable and Sustainable Energy Reviews*, 155:111920, 2022. URL *http://doi.org/10.1016/j.rser.2021.111920*.

[165] G Quaranta, C Argerich Martin, R Ibáñez, J L Duval, E Cueto, and F Chinesta. From linear to nonlinear PGD-based parametric structural dynamics. *Comptes Rendus Mécanique*, 347(5):445–454, 2019. URL *http://doi.org/10.1016/j.crme.2019.01.005*.

[166] R Castro-Triguero, S Murugan, R Gallego, and M I Friswell. Robustness of optimal sensor placement under parametric uncertainty. *Mechanical Systems and Signal Processing*, 41(1):268–287, 2013. URL *http://doi.org/10.1016/j.ymssp.2013.06.022*.